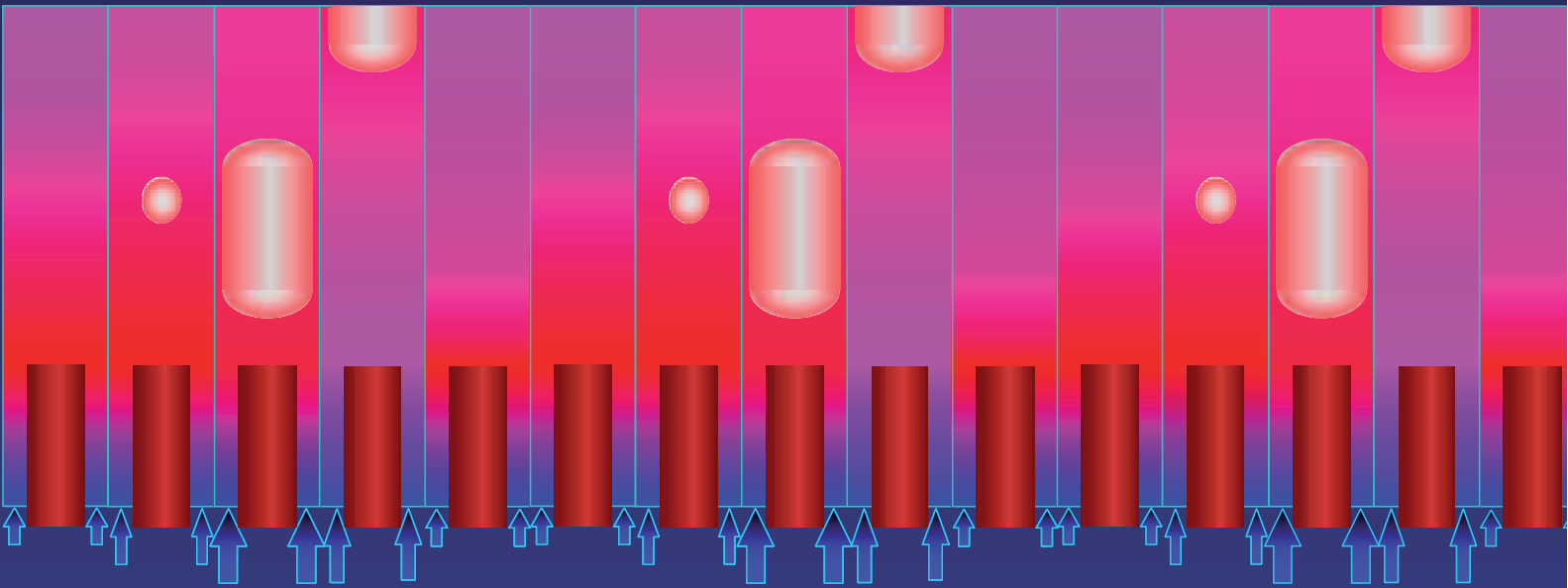


Experimental and Analytical Modeling of Natural Circulation and Forced Circulation BWRs

Thermal-Hydraulic, Core-Wide, and Regional Stability Phenomena



Masahiro Furuya

Experimental and Analytical Modeling of
Natural Circulation and Forced Circulation BWRs
– Thermal-Hydraulic, Core-Wide, and Regional Stability Phenomena

The research described in this thesis was performed at Nuclear Technology Research Laboratory, Central Research Institute of Electric Power Industry (CRIEPI), 2-11-1 Iwado-Kita, Komae, Tokyo 201-8511, Japan and the Department of Radiation, Radionuclides and Reactors (R³), Faculty of Applied Sciences, Delft University of Technology, Mekelweg 15, 2629 JB Delft, The Netherlands.

Experimental and Analytical Modeling of Natural Circulation and Forced Circulation BWRs

– Thermal-Hydraulic, Core-Wide, and Regional Stability Phenomena

PROEFSCHRIFT

ter verkrijging van de graad van doctor
aan de Technische Universiteit Delft,
op gezag van de Rector Magnificus prof.dr.ir. J. T. Fokkema,
voorzitter van het College voor Promoties,
in het openbaar te verdedigen

op maandag 24 april 2006 om 13:00 uur

door

Masahiro FURUYA

Master in Nuclear Engineering,
Tokyo Institute of Technology, Tokyo, Japan
geboren te Yamaguchi, Japan

Dit proefschrift is goedgekeurd door de promotor:
Prof. dr. ir. T. H. J. J. van der Hagen

Samenstelling promotiecommissie:

Rector Magnificus, voorzitter	
Prof. dr. ir. T. H. J. J. van der Hagen,	Technische Universiteit Delft, promotor
Prof. dr. ir. A. H. M. Verkooijen,	Technische Universiteit Delft
Prof. dr. ir. H. van Dam,	Technische Universiteit Delft
Prof. dr. R. F. Mudde,	Technische Universiteit Delft
Prof. dr. T. Takamasa,	Tokyo University of Marine Science and Technology
Prof. dr. K. Okamoto,	The University of Tokyo

Copyright © 2006 by Masahiro FURUYA and IOS Press

All rights reserved. No part of this book may be reproduced, stored in a retrieval system, or transmitted, in any form of by any means, without prior permission from the publisher.

ISBN

Keywords: boiling water reactor, natural circulation, regional stability, dynamics

Published and distributed by IOS Press under the imprint Delft University Press

Publisher & Distributor

IOS Press
Nieuwe Hemweg 6b
1013 BG Amsterdam
Netherlands
fax: +31-20-687 0019
email: info@iospress.nl

Distributor in the USA and Canada

IOS Press, Inc.
4502 Rachael Manor Drive
Fairfax, VA 22032
USA
fax: +1-703-323 3668
e-mail: sales@iospress.com

LEGAL NOTICE

The publisher is not responsible for the use which might be made of the following information.

PRINTED IN THE NETHERLANDS

To Tomoyo

Contents

1	Introduction	1
1.1	Historical Perspective of Nuclear Reactors	2
1.2	Description of BWRs	3
1.3	Classification of Stability Types	4
1.4	Review of Channel Stability Research	6
1.4.1	Type-I and Type-II Instabilities	6
1.4.2	Flashing-Induced Instability	8
1.5	Review of Core-Wide and Regional Stability Research	8
1.6	Motivation behind Present Work	9
1.7	Thesis Outline	10
2	Low-Pressure Thermal-Hydraulic Stability	11
	Abstract	11
2.1	Introduction	11
2.2	SIRIUS-N Experimental Facility	13
2.2.1	Thermal-hydraulic Loop	13
2.2.2	Experimental Procedure	13
2.2.3	Void Fraction Estimation	14
2.3	Experimental Results	16
2.3.1	Signal Time Traces	16
2.3.2	Stability Maps for Different Pressures	18
2.4	Instability Mechanism	20
2.5	Comparison with Other Kinds of Instabilities	21
2.5.1	Geysering	21
2.5.2	Flow Pattern Transition Instability	22
2.5.3	Natural Circulation Oscillation	23
2.6	Stability Boundary and Stability Estimation for the ESBWR	25
2.7	Conclusions	26
3	High-Pressure Thermal-Hydraulic Stability	27
	Abstract	27
3.1	Introduction	27
3.2	Instability Characteristics	28
3.2.1	Representative Signals and Instability Phenomenology	28
3.2.2	Effect of System Pressure, Heat Flux, and Inlet Subcooling	30
3.3	Comparison with Other Kinds of Instabilities	33
3.3.1	Flashing-induced Density Wave Oscillations	33
3.3.2	Geysering	34
3.3.3	Flow Pattern Transition Instability	35

3.3.4	Natural Circulation Oscillation	36
3.4	Modeling of Boiling Two-Phase Flow Dynamics for Stability Estimation	36
3.4.1	Historical Perspective of Analytical Modeling	37
3.4.2	Reduced-Order Model	37
3.4.3	Verification of Static Characteristics with Experimental Data	40
3.4.4	Analytical Prediction of the Lower Subcooling Stability Boundary	42
3.4.5	Instability Characterization by Linear Stability Analysis	42
3.4.6	Effect of Single-Phase Liquid Natural-Circulation	43
3.5	Effect of Inlet Throttling	47
3.5.1	Experimental Investigation	48
3.5.2	Numerical Investigation	49
3.6	Conclusions	50
4	Implementation Method for Neutronic-Thermalhydraulic Coupling	53
	Abstract	53
4.1	Introduction	53
4.2	Methodology to Implement Artificial Void Reactivity Feedback	54
4.3	Measurement and Control System	55
4.4	Formulations of Real-Time Analysis	58
4.4.1	Thermal-hydraulics	58
4.4.2	Neutronics	58
4.4.3	Thermal Conduction in the Fuel Rod	59
4.5	Identification of Transfer Functions	60
4.5.1	Power Supply	60
4.5.2	Heater Rod	61
4.5.3	Differential Pressure Measurement System	62
4.6	Conclusions	62
5	Natural Circulation BWR Core-Wide and Regional Stabilities	65
	Abstract	65
5.1	Introduction	65
5.2	Stability Estimation Based on Noise Analysis	66
5.2.1	Method Description	66
5.2.2	Optimization of Model Parameter	67
5.3	Regional Stability Estimation with SIRIUS-N Facility	69
5.3.1	Implemented Power Profile and λ -mode Eigenvalue Separation	69
5.3.2	Investigation of Rated Operating Conditions	70
5.3.3	Stability Effect of Design Parameters	71
5.3.4	Stability Identification by Limit Cycle Oscillations	73
5.4	Conclusions	75
6	Forced Circulation BWR Core-Wide and Regional Stabilities	77
	Abstract	77
6.1	Introduction	77
6.2	SIRIUS-F Experimental Facility	78
6.2.1	Design Concept	78
6.2.2	Boiling Two-Phase Flow Loop	81
6.2.3	Experimental Procedure	82
6.3	Description of Design Analysis Code	82

6.4	Experimental and Analytical Parameters	84
6.5	Results on Channel Stability	86
6.5.1	Minimum Pump Speed Line	86
6.5.2	Natural Circulation Line	87
6.6	Results on Core-Wide and Regional Stability	87
6.6.1	Minimum Pump Speed Line	87
6.6.2	Natural Circulation Line	89
6.7	Conclusions	89
6.8	Recommendation	90
7	Conclusions	91
7.1	Concluding Remarks in the Thesis	91
7.2	Future Work	94
A	Reduced-order Model	97
A.1	Neutron Kinetics	97
A.2	Fuel Dynamics	97
A.3	Boiling Boundary Dynamics	97
A.4	Core Void Dynamics	97
A.5	Chimney Void Dynamics	98
A.6	Mass-flux Density Dynamics	98
B	Transfer Functions Used in the Frequency-Domain Analysis	101
	Nomenclature	103
	List of Publications	107
	Bibliography	109
	Summary	115
	Samenvatting (Summary in Dutch)	119
	内容梗概 (Summary in Japanese)	123
	Dankwoord (Acknowledgments)	127
	Curriculum Vitae	129

List of Tables

2.1	Comparison of SIRIUS-N Facility with Prototypical Natural Circulation BWR .	14
3.1	Dynamic Pressure Drops in the Natural Circulation Loop	44
3.2	Dimension of DESIRE Facility	46
3.3	Rated DESIRE Conditions for Stability Analysis	46
4.1	Heater Rod Parameters in Thermal Conductivity Experiment	61
5.1	Parameters in Parametric Study on Noise Analysis at Rated Operating Conditions	67
5.2	Parameters in Stability Experiment Near Rated Operating Conditions	70
6.1	Specifications of Design Analysis Code	84
6.2	Input Parameters of Design Analysis Code and Experiments	85
A.1	Pressure Drops in Reduced-Order Model	99

List of Figures

1.1	Generation IV Concept	2
1.2	Schematic of Boiling Water Reactors.	4
1.3	Typical Stability Map	7
2.1	Schematic of Natural Circulation BWR	12
2.2	Schematic of SIRIUS-N Facility	12
2.3	Time Traces of Signals Measured When $P_s = 0.2$ MPa and $q'' = 53$ kW/m ²	16
2.3	Time Traces of Signals Measured When $P_s = 0.2$ MPa and $q'' = 53$ kW/m ² (Cont'd)	17
2.4	Stability Maps for a Range of Heat Fluxes and Inlet Subcooling	18
2.5	Stability Maps for $P_s = 0.1, 0.2, 0.35,$ and 0.5 MPa	19
2.6	Relationship of Enthalpy Wave Propagation Time to Oscillation Period	19
2.7	Proposed Process for Flashing-induced Density-Wave Oscillations	22
2.8	Relationship between Boiling Delay Time and Oscillation Period	23
2.9	Transient Flow Patterns at $P_s = 0.2$ MPa and $q'' = 53$ kW/m ²	23
2.10	Momentum Response to a Natural Circulation Driving Force	24
2.11	Stability Boundary for Higher Subcooling	25
3.1	Effect of Flashing in Terms of Pressure	28
3.2	Representative Time Traces of the Signals Measured when $P_s = 2$ MPa and $q'' = 228$ kW/m ² , $N_{sub} = 5.46$	29
3.3	Stability Maps in Reference to Heat Flux and Inlet Subcooling	30
3.4	Stability Maps at $P_s = 1, 2, 4,$ and 7.2 MPa	32
3.5	Relationship of Bubble Passing Time to Flow Oscillation Period for Different Pressures	33
3.6	Relationship of Single Phase Liquid Passing Time to Flow Oscillation Period for Different Pressures	33
3.7	Relationship of Boiling Delay Time to Oscillation Period for Different Pressures	34
3.8	Trajectory of Transient Flow Patterns at $P_s = 2$ MPa and $q'' = 228$ kW/m ² , $N_{sub} = 5.46$	34
3.9	Momentum Response of Natural Circulation Driving Force at $P_s = 2$ MPa and $q'' = 228$ kW/m ² , $N_{sub} = 5.46$	35
3.10	Reduced-Order Model Diagram	38
3.11	A Cut-Away Scheme of Dodewaard Natural-Circulation BWR	38
3.12	Block Diagram of Reduced-Order Model	39
3.13	Validation of Analytical Static Characteristics	41
3.14	Analytical Prediction of Stability Boundary	41
3.15	Stability Map in Subcooling - Phase Change Number Plane	42
3.16	Relationship of Bubble Passing Time to Flow Oscillation Period for Different Pressures.	42
3.17	Typical Stability Map for Type-I and Type-II Density Wave Oscillations	45

3.18	Schematic of DESIRE Facility	45
3.19	Stability Effect of Liquid Density Derivative with Respect to Temperature	46
3.20	Relationship between Shift of Operating Condition and Stability Boundary in terms of Liquid Density Derivative	46
3.21	Effect of Inlet Restriction on Inlet Velocity and Void Fraction	47
3.22	Stability Map in Reference to Inlet Subcooling and Inlet Restriction	48
3.23	Relationship of Driving Force of Natural Circulation to Momentum Energy in Reference to Inlet Restrictions	48
3.24	Decrease in Inlet Velocity with Increasing Inlet Restriction	49
3.25	Analytical Stability Boundaries for Various Inlet Restrictions	49
4.1	Block Diagram of Closed Transfer Functions for Artificial Void-Reactivity Feedback	54
4.2	Block Diagram of Closed Transfer Functions in terms of Core-Wide and Regional Stability	55
4.3	Overview of the Digital Controller of the SIRIUS-N Facility	56
4.4	User Interfaces of SIRIUS-N Control and Monitoring System	57
4.5	Indicial Response of Developed Power Supply	61
4.6	Noise Response of Developed Power Supply	61
4.7	Thermal Conductivity Time Constant of Heater Rod	62
4.8	Time Constant of DPMS	62
5.1	Effect of Auto Regressive Model Order	67
5.2	Effect of Data Size for Noise Analysis	67
5.3	Verification of AR Method with PSD	68
5.4	Power Distributions and Their Subcriticalities	69
5.5	Stability Effect of Void Reactivity	71
5.6	Interaction Mode between Half-Cores	72
5.7	Stability Effect of Power Profile	72
5.8	Stability Effect of Fuel Rod Time Constant	73
5.9	Stability Effect of Core Inlet Subcooling	73
5.10	Effect of Power Distribution on Stability	74
5.11	Time Traces of Signals under Stable Conditions and Regional Instability	75
6.1	Thermal Conductivity Time Constant of Heater Rod in SIRIUS-F Facility	79
6.2	Time Constant of DPMS in SIRIUS-F Facility	79
6.3	Schematic of Thermal-Hydraulic Loop of SIRIUS-F Facility	80
6.4	Axial Pressure Profile Measured at SIRIUS-F Facility	81
6.5	Relationships among Models in Analysis	83
6.6	ABWR Power-Flow Operating Map and SIRIUS-F Experimental Range	84
6.7	Channel Stability on Minimum Pump Speed Line	86
6.8	Channel Stability on Natural Circulation Line	86
6.9	Core-Wide and Regional Stability on Minimum Pump Speed Line	88
6.10	Core-Wide and Regional Stability on Natural Circulation Line	88
6.11	Interaction Mode between Half-Cores	88

Chapter 1

Introduction

The world's population is expected to increase from about 6 billion people in year 2004 to 10 billion in year 2050. As the Earth's population grows, so will the demand for energy, improved standards of living, better health, and longer life expectancy. For the Earth to support its growing population, human beings will have to increasingly take advantage of energy sources that do not have adverse environmental effects and which contribute as little as possible to global warming. One of the cleanest, safest and most cost-effective sources is nuclear energy, even though a major public concern about the disposal of radioactive waste is present. Currently, approximately 440 nuclear power reactors are in operation in 31 countries. Together, they generate electricity for 1 billion people in a reliable manner without emitting noxious gases into the atmosphere.

Among these 440 nuclear power reactors, the majority consists of so-called Pressurized Water Reactors (PWRs) and Boiling Water Reactors (BWRs). In both types of reactors, light water (H_2O) is heated by the nuclear fuel. In a PWR, water is heated at high pressure. Due to the high pressure, boiling of the water is suppressed. The hot water is used to produce steam in a secondary loop, which is led into the steam turbines to produce electricity. In a BWR, however, steam is produced in the core of the reactor itself.

Due to the presence of steam in BWRs, this type of reactor shows a range of complex physical processes that influences the stability and safety of the reactor. These physical processes refer to e.g. the coupling of thermal-hydraulics and neutronics, the adiabatic boiling due to the reduction of the hydrostatic head at low pressure (flashing) and dry-out (the absence of a liquid water film on the fuel rod).

In this thesis, the stability of two types of BWRs, being the so-called *natural circulation* BWR and *forced circulation* BWR, has been studied. In the latter type of reactor, the water is pumped through the core. In the natural circulation BWR, the flow is driven by the difference between the density of the water-steam mixture in the core and the liquid water in the down-comer. In both types of BWRs, the boiling two-phase flow in the core may become less stable because of the time lag between the steam generation and the change of the pressure drop over the core. Furthermore, the neutronic coupling may make the system less stable. These two issues are of practical importance and should be studied thoroughly before such BWRs can be taken into operation.

This thesis, covering more than ten years of work, focuses on the thermal-hydraulics, core-wide and regional stability phenomena. Before clarifying the specific stability properties of the BWR in more detail, however, a description of the developments considering nuclear reactors is given in the following section.

is not simply a larger version of a natural circulation BWR. It is equipped with passive safety features such as isolation condensers and a gravity driven emergency core cooling system (McCandless and Redding, 1989). GE hoped to obtain a design certification for the SBWR from the United States Nuclear Regulatory Commission (USNRC). GE terminated the project in 1998, because the design was considered to be too expensive. In order to achieve a less expensive model, the SBWR concept was used as the basis of the following two reactor concepts as illustrated in Figure 1.2: the Japanese Simplified BWR (JSBWR, 1200MWe) designed jointly by GE, Hitachi, and Toshiba in 1995 (Tabata *et al.*, 1997) and the European Simplified BWR (ESBWR, 1190MWe) designed by GE in 1996 (Challberg *et al.*, 1998; Cheung *et al.*, 1998). The significant increase in overall output power from the SBWR design to the JSBWR and the ESBWR designs required certain changes to assure a sufficient coolant flow rate. The concept of the ESBWR is proposed in the Generation III period. The refinements in designing of the ESBWR are in progress. The ESBWR is expected to go into commercial operation soon in the Generation III+ period.

Generation III+ The Generation III+ consists of reactor designs that offer improved economics for near-term deployment. Two of those reactor designs, being the High Temperature Reactor (HTR) and the Reduced Moderation Light Water Reactor (RMLWR), will be briefly described here. The HTR is a promising nuclear reactor in Generation III+. The core of the HTR is cooled by a gas (helium, etc.) Due to the high temperature of the coolant gas, the HTR can also be used for the production of heat. This process-heat could be used in chemical industry, paper-mills, city heating and desalination plants.

The RMLWR is a water-cooled reactor with a hard neutron spectrum (high energy). In the RMLWR design, natural circulation is feasible, since the vapor volume fraction (hereafter called void fraction) in the core is larger than in conventional BWRs. Since the elimination of recirculation pumps makes pump power supply and control systems unnecessary, the reactor core cooling system is strongly simplified.

Generation IV The Generation IV International Forum (GIF) selected six reactor concepts, which offer advantages in the areas of economics, safety and reliability, and sustainability, and could be deployed commercially by 2030 (USDOE Nuclear Energy Research Advisory Committee and the Generation IV International Forum, 2002). Those are: (1) Very-High-Temperature Reactor (VHTR), (2) Supercritical-Water-Cooled Reactor (SCWR), (3) Gas-Cooled Fast Reactor (GFR), (4) Lead-Cooled Fast Reactor (LFR), (5) Sodium-Cooled Fast Reactor (SFR), and (6) Molten Salt Reactor (MSR). Although different fluids are used to cool the reactor core, a large natural circulation force can be obtained for all types of the reactors, because of the great density difference of the coolant between the core (and the chimney) and the downcomer (or primary loop). Natural circulation driven cooling could therefore be employed in the SCWR, the GFR and the LFR. It is to be expected that the natural circulation will have influence on the stability, similar to that of a BWR such as the ESBWR.

1.2 Description of BWRs

In historical perspective, stability has been the main concern in the development stage of BWRs. The boiling two-phase flow in the core may become less stable because of the time lag between vapor generation and pressure loss perturbation (the void sweep phenomenon). Furthermore, void-reactivity feedback may make the system less stable. These two issues are of practical

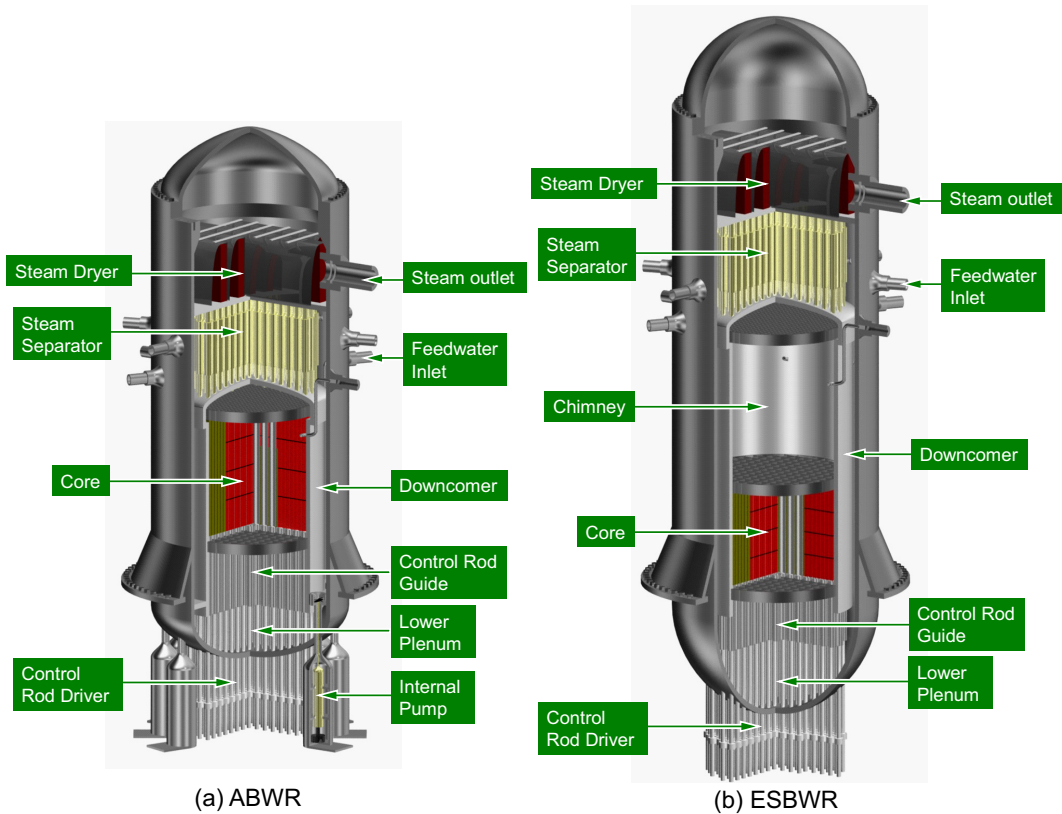


Figure 1.2: A cut-away of (a) ABWR and (b) ESBWR vessels. No recirculation pumps are used in the ESBWR design. Instead of pumps, a relatively long chimney is placed on top of the core in order to increase the natural-circulation flow rate.

importance for designing and operating BWRs. We, therefore, focus on the stability of BWRs in this thesis.

Figure 1.2 (a) shows an Advanced Boiling Water Reactor (ABWR, Generation III) as an example of a modern forced circulation BWR. The internal diameter and height of the reactor vessel are approximately 7 m and 22 m, respectively. Heat is produced by nuclear fission in the core, which consists of 872 fuel assemblies. A fuel bundle is formed through a lattice of 8×8 fuel rods. The ceramic fuel pellets are cylindrical in shape, approximately 10 mm in diameter and 10 mm long. Approximately 370 fuel pellets are piled up and encased in a Zircaloy cladding. Heat produced in the core is removed by the coolant (ordinary water, H_2O). The coolant enters at the bottom of the core, approximately 10 K below the saturation condition. As the coolant flows upwards along the fuel cladding and the temperature rises to its saturation point, the coolant starts boiling. At the core exit, approximately 15 % of the coolant mass is converted into steam. This steam-water mixture flows through the steam separators and dryers exiting the core. The steam exits the vessel and drives the turbines. The turbine axis is coupled with an electric generator which produces electricity. The water, which is separated from the steam in a condenser, flows downwards in the downcomer (the periphery of the core) and mixes with the recirculated condensate from the turbines.

1.3 Classification of Stability Types

Natural circulation reactors and related concepts can be found in each Generation as indicated in Figure 1.1. In all the above natural circulation reactor designs, the magnitude of the natural-circulation flow rate depends on the driving head and on the pressure losses along the circulation

path. In order to determine the desired dimensions of these reactors, one can apply design principles on the basis of static characteristics by assuming steady-state behavior of the natural circulation loop. For instance, one can increase the chimney height to enhance the core flow rate. As can be easily understood from reactor startup and shut down processes, reactors cannot be operated without a transient condition: i.e. the dynamic behavior of the system is an essential factor in the reactor design. It has been proven and experienced that both forced circulation and natural circulation BWRs can be unstable at times during unanticipated large-scale fluctuations in pressure, flow rate, and heat generation rate (D'Auria *et al.*, 1997). These instabilities can make a reactor deviate from steady-state conditions and must be thoroughly evaluated with respect to reactor safety. The stability feature discussed in this thesis can be described as a macroscopic phenomenon in principle (rather than a microscopic phenomenon characterized by the dynamics of individual bubble). In the following section, the instabilities relevant to BWRs are described in detail.

In BWR design the stability of all operating conditions in the reactor power/flow map as well as quasi-static transients during operation must be evaluated. Typically, a stability evaluation addresses four primary aspects, viz.:

Channel Stability Channel stability is defined as the thermal-hydraulic stability of an individual channel in parallel with other channels. Each channel is assumed not to be neutronically coupled with the rest of the core. Channel stability is analyzed, thereby assuming that the channel pressure drop, imposed on an individual channel by the rest of the core, is constant. Channel stability can be enhanced by designing the fuel to have a high ratio of single phase pressure drop to two-phase pressure drop. Instability cannot occur in a single channel in a BWR, because it is neutronically coupled with neighboring channels (except in extremely degraded conditions). Therefore, the channel stability must be considered together with core-wide and regional stabilities (see the following paragraphs), which account for the neutronic coupling.

Core-Wide Stability Core-Wide stability is defined as reactivity feedback stability and depends on the neutron flux response to a perturbation. This is also termed overall loop stability, because it involves the loop outside the core through the downcomer, as well as the core. In the fuel and core design process, core-wide stability is enhanced by controlling the single-phase to two-phase pressure drop ratio, void reactivity coefficient, fuel time constant, and radial peaking factor. For a new reactor design or changes to the operating domain, average power-to-flow ratio, and inlet orificing are also key factors in determining core stability.

Regional Stability Regional oscillations are the result of exciting a subcritical harmonic spatial mode of the reactor neutronics (in other words, a higher than fundamental mode, which is not self-sustaining). In the past, the onset of regional oscillations has been correlated empirically as a function of the channel and core-wide stability characteristics (often referred to as 1-1 map). Regional oscillations can be excited by a group of channels that are also unstable. In addition, the void reactivity coefficient, the power-to-flow ratio, and the fuel rod time constant are also important. The size of the core (number of bundles) is a key factor in determining the susceptibility of a core to regional oscillations. For a core of a given size, the radial power distribution also plays a role in determining whether regional oscillations may take place.

Overall Plant Stability The response of the plant to external perturbations must also be stable. Once core-wide and regional stabilities are enhanced, it becomes a matter of tuning the control systems to damp the response to perturbations.

In the following section, short reviews of channel, core-wide, and regional stabilities are presented. The overall plant stability is not presented, since it is not dominated by the reactor core behavior and it is typically evaluated during the design of plant control systems.

1.4 Review of Channel (Boiling Two-Phase Flow) Stability Research

In general, several types of thermal-hydraulic instabilities may occur in a boiling two-phase system (Bouré *et al.*, 1973; Ishii, 1976; Yadigaroglu, 1981a; Nakanishi, 1979; Kakac and Liu, 1991). Some of these instabilities arise from the steady state characteristics of the system such as flow excursion (or Ledinegg instability) and relaxation instability (flow pattern transition, bumping, geysering, and chugging, etc.). The remaining types of instabilities are due to the dynamic nature of the system such as density wave oscillations, pressure drop oscillations, acoustic oscillations and thermal oscillations.

In forced circulation BWRs, the most commonly encountered instabilities are so-called density wave oscillations, which may occur in the operation range from start-up to rated conditions. Density wave oscillations may induce power oscillations through void reactivity coupling (feedback from void to power).

In contrast to forced circulation BWR stability, the number of references dealing with the natural circulation BWR is limited. Aritomi *et al.* (1992) and Chiang *et al.* (1993a) pointed out three types of instabilities that might occur in natural circulation BWRs: *viz.* geysering, natural circulation oscillations, and density wave oscillations. They also found that such instabilities could be suppressed above 0.5 MPa. At earlier stages, however, Mathisen (1967) reported large amplitude oscillations even at high pressures ($1 \text{ MPa} \leq P_s \leq 7 \text{ MPa}$). These instabilities were found to be induced by the natural circulation flow dynamics. Therefore, the mechanism that causes instabilities in natural circulation BWRs at both low and high pressures still deserves attention.

1.4.1 Type-I and Type-II Instabilities

Within the class of density wave oscillations, two distinct types of instabilities can be found. Fukuda and Kobori (1979) proposed the Type-I instability (only occurring with a chimney installed) and the Type-II instability. The Type-I instability is dominant when the flow quality is low, while the Type-II instability is dominant when the flow quality is high. The Type-II instability is the most commonly observed form of density wave oscillation.

Numerous numerical simulations were performed on the sensitivities of Type-I and Type-II instabilities to system parameters such as heat flux, subcooling and pressure. Lin *et al.* (1993) and Yokobori *et al.* (1992) estimated the stability of natural circulation BWRs numerically by using the TRAC code. This code is based on the time domain two-fluid model. A similar study was also performed by Masuhara *et al.* (1993), who used a frequency domain linear stability code. In these studies, however, the mechanism behind the instability was not investigated.

Such a study was also performed experimentally at the Dodewaard natural circulation BWR. Van der Hagen *et al.* (2000) showed evidence of Type-I instability under low power and reduced pressure conditions, and Type-II instability at high power and low pressure conditions.

In general, it can be concluded that further detailed investigation is required to examine the mechanism behind the instabilities found at both low and high pressures (in terms of the classification proposed by Fukuda and Kobori (1979)).

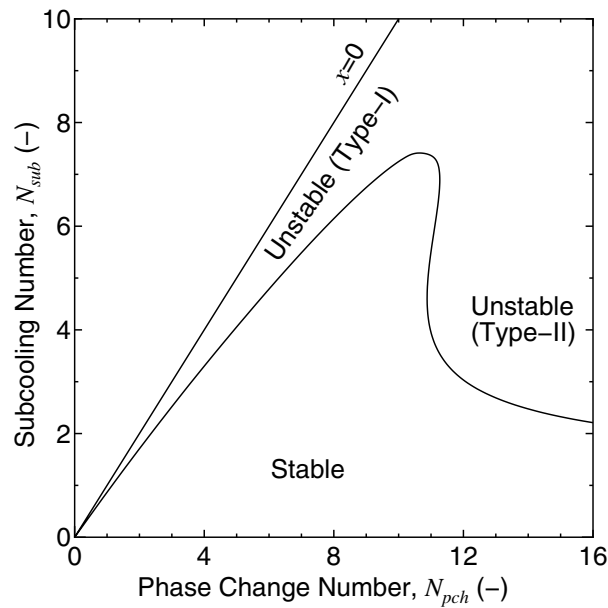


Figure 1.3: Stability boundaries are shown for Type-I and Type-II instabilities in the phase change number and the subcooling number. The Type-I instability region becomes smaller as the chimney length is decreased.

Ishii and Zuber (1970), Nayak *et al.* (1998), Van Bragt and Van der Hagen (1998a) and Van Bragt and Van der Hagen (1998b) have conducted a linear stability analysis by creating a set of linear equations to describe the natural-circulation boiling two-phase flow. They determined the stability boundaries of Type-I and Type-II instabilities, which can be represented as a function of the dimensionless phase change number (also known as the Zuber number) and the subcooling number. The phase change number, N_{pch} , is proportional to the heating power and inversely proportional to the coolant flow rate, while the subcooling number, N_{sub} , is proportional to the channel inlet subcooling. Figure 1.3 shows a typical stability map in the dimensionless plane of the phase change number and the subcooling number for a natural circulation system consisting of a heated core, adiabatic chimney and a downcomer. The liquid density differences have been neglected. The straight line in the figure indicates the operational points where the flow quality at the core exit is zero. Therefore, this line divides the stability map into two regions: a single phase flow region ($N_{sub} \geq N_{pch}$) and a boiling two-phase flow region ($N_{sub} < N_{pch}$).

The stability boundary is drawn in the two-phase flow region as a curve in the figure. The flow is stable below the curve. Type-I instability is dominant when the flow quality is small (in between the zero quality line and the stability boundary curve), while Type-II instability is dominant at the large flow quality. The stability boundary is independent of the pressure, if one applies the homogeneous equilibrium mixture (HEM) model and neglects changes in thermodynamic properties such as densities and liquid saturation enthalpy. The HEM model assumes a perfect mixture of liquid and vapor.

The thermo-dynamic properties are, in reality, dependent on temperature: i.e. a liquid density difference induces single phase natural circulation. In Section 3.4.6, the linearized model is, therefore, extended to take into account the dependence of the liquid density on fluid temperature. Based on that model the effect of single phase natural circulation on Type-I and Type-II instabilities were studied.

1.4.2 Flashing-Induced Instability

Thermo-dynamic properties are also dependent on pressure: i.e. saturation enthalpy changes with pressure, which in turn induces the flashing phenomenon (the sudden increase of vapor generation due to the reduction in hydrostatic head). Wissler *et al.* (1956) were the first to report that flashing causes instability at low pressure. We investigated the occurrence conditions and the mechanism of flashing-induced instability experimentally in a relatively low system pressure at the SIRIUS-N facility, which simulates a prototypical natural circulation BWR (Furuya *et al.*, 1995, 2004). Later on, Manera (2003) investigated the dynamics of a flashing bubble with wire mesh sensors (Prasser *et al.*, 1998) in a natural circulation loop (the CIRCUS facility).

1.5 Review of Core-Wide and Regional (Neutronic-Thermal-hydraulic Coupling) Stability Research

As discussed in Section 1.3, instability cannot occur in a single channel in a BWR, because it is neutronicly coupled with neighboring channels. Therefore, in stead of channel stability tests, stability tests have been performed at operating BWRs for many years. Results show that BWRs are only susceptible to instabilities at the lower corner of the power/flow map (at a relatively high power to flow ratio). Early test programs at the Peach Bottom reactor (Larsen, 1978; Carmichael and Niemi, 1978) and Vermont Yankee (Sandoz and Chen, 1983) reactor provided a large quantity of data on core-wide stability and the onset of limit cycle oscillations in the natural circulation region of the power/flow map. Regional oscillations in the out-of-phase mode were first seen at the Caorso plant in 1982. Subsequently, another test program was set up in October 1983 (Gialdi *et al.*, 1984) to study out-of-phase mode oscillations. The stability test performed during the startup of the Leibstadt plant in 1984 also resulted in regional oscillations at minimum pump speed conditions. A few occurrences of regional oscillations have been observed in other plants as well.

Regional oscillations are induced by out-of-phase oscillations in neutron flux and channel inlet flows between regions of the core that are symmetric around the diagonal of the core. Early analyses of these oscillations relied entirely on time domain transient analysis codes (Takigawa *et al.*, 1987), which were useful for calculating the oscillations, but did not yield much insight into the underlying physical phenomena. Later, March-Leuba and Blakeman (1991) pointed out that these oscillations excite higher neutronic harmonics modes. These modes are subcritical under steady-state conditions, though it would be possible to overcome the damping in the neutronics due to the subcriticality. The regional mode is the dominant oscillation mode from the thermal-hydraulics point of view, particularly when axial peaking leads to a thermal-hydraulically least stable condition in the highest power channels. This is because the loop outside the core is not involved in the oscillation; the oscillation occurs primarily between groups of channels with a minimal variation in the total core flow. The regional mode is not the dominating mode of oscillation from the perspective of the neutronics, because it is normally subcritical. Therefore, the balance between thermal-hydraulic gain and neutronic damping determines the dominating mode of oscillation: core-wide or regional.

Due to symmetry of regional oscillations, significant cancellation of power variations can occur. Specifically, the oscillation in total power indicated by the Average Power Range Monitor (APRM) is much smaller than those in local regions, as indicated by the Local Power Range Monitors (LPRMs). More research must, therefore, be undertaken to determine whether they can be detected and mitigated during reactor operation.

It is a well established fact that as the core size increases the nuclear coupling between

different parts of the core becomes weaker. Therefore, the core becomes more susceptible to regional oscillations. Therefore, regional stability considerations can limit the maximum core size and feasible power ratings. With the current trend towards increasing power ratings, it is important to evaluate the implication of core size and power on regional stability.

The mechanism of regional oscillations is based on exciting the subcritical higher harmonic modes (in particular, the first azimuthal harmonic) of the neutronics. Therefore the key neutronic parameters for predicting regional oscillations are the subcritical reactivity associated with these harmonic modes, and the corresponding void reactivity.

In addition to stability experiments conducted in nuclear power plants, out-of-pile facilities have been built to study thermal-hydraulic stability. Since void-reactivity feedback does not exist in out-of-pile facilities, most of the facilities could only be used to estimate so-called channel stability, which is defined as a thermal-hydraulic stability at a fixed power condition. Uehiro (1997) was the first to introduce artificial void-reactivity feedback into the facility located at Kyushu University, Japan. Later, Kok and Van der Hagen (1999a) designed a scaled loop (DE-SIRE), with Freon as the working fluid, at the Delft University of Technology, the Netherlands, and investigated instability characteristics in detail. Recently, Iguchi *et al.* (2000) and Iguchi *et al.* (2003) also constructed a core-wide stability facility (THYNC) at the JAERI research institute, Japan. However, the THYNC facility was not designed with the same friction factors as those in a BWR core, which are important in the simulation of BWR stabilities. All these facilities were used for fundamental research on core-wide stability. At present, there is no facility suitable for investigating *regional stability*. Regional stability is, however, the dominant mode in most of the transient scenarios in modern BWRs.

1.6 Motivation behind Present Work

In the early 1990s, it became very important to assess the feasibility of large-scale natural circulation BWRs such as the SBWR and the JSBWR. Special attention was paid to the flashing phenomenon. At that time, the mechanism of flashing-induced instability in natural circulation BWRs with a chimney was not yet clear. Hence, the stability database of natural circulation BWRs was limited. To cope with the lack of experiments and analytical models for natural circulation BWRs, the SIRIUS-N project was started in 1993 at the Central Research Institute of the Electric Power Institute (CRIEPI) in Japan.

The SIRIUS-N project focused on the investigation of flashing-induced instability and Type-I instability. The project has been partly conducted in cooperation with GE and the Interfaculty Reactor Institute, Delft University of Technology. The work also resulted in a research project on the same subject at the Delft University of Technology (Zboray, 2002; Manera, 2003).

Analytical models were developed to evaluate core-wide and regional stabilities of forced circulation and natural circulation BWRs (Ishii and Zuber, 1970; Nayak *et al.*, 1998; Van Bragt and Van der Hagen, 1998a). Out-of-pile facilities, however, were not available. Therefore, in order to gain confidence in the design of a prototypical natural circulation BWR, a method to implement void-reactivity feedback was developed and used to investigate core-wide and regional stabilities in order to validate a model for core-wide and regional stabilities.

The developed method has also been useful to study forced circulation BWRs in order to gain confidence in the area of reactor core management. Consequently, the SIRIUS-F project was initiated in 2002 at CRIEPI. The SIRIUS-F project is focused on the evaluation of channel, core-wide, and regional stabilities in a forced circulation BWR and especially in an Advanced BWR (ABWR). Experiments were conducted at the SIRIUS-F facility to gain insight into the relevant physics and to validate the licensing analysis codes for BWR stability over a wide range

of the reactor operating conditions.

It took a decade to determine an entire picture of the instability mechanisms and evaluate core-wide and regional stabilities. This thesis addresses the results of the SIRIUS-N and SIRIUS-F projects.

1.7 Thesis Outline

This thesis contains seven chapters: an introduction, conclusion and five technical chapters. Each chapter has its own abstract, introduction, and conclusions, and can more or less be read independent from the other chapters.

In Chapter 2, experimental studies related to the low-pressure instability in a natural circulation loop with a chimney are presented. The facility used for these studies was designed and constructed to simulate the thermal-hydraulics of a prototypical natural circulation BWR. The investigation emphasis is on the flashing phenomenon and its role in low pressure instability. Stability characteristics are discussed and the process of the flashing-induced instability is explained.

In Chapter 3, high-pressure instability in a natural circulation loop with a chimney is investigated. Stability maps were obtained under different experimental conditions (inlet restriction, heat flux, inlet subcooling, and system pressure). The characteristics of the instability were studied, to gain greater insight into the dynamics, by comparing characteristic times to phenomenological time constants. In addition, a linear stability analysis of a natural circulation BWR is performed by examining single-phase natural circulation. The analytical stability boundary is compared with an experimental database to validate the analysis. A parametric study is also conducted to increase the size and range of the experimental database.

In Chapter 4, a methodology to implement artificial neutronic feedback is developed and then implemented in a simulated thermal-hydraulic loop in order to study BWR coupled neutronic-thermalhydraulic stability. The equations and correlations used to estimate the core-wide and regional stabilities of BWRs are also described and validated in this chapter.

In Chapter 5, core-wide and regional stabilities were estimated for a natural circulation BWR, using the SIRIUS-N facility, by taking into account neutronic-thermalhydraulic coupling. As indicators of the stability, decay ratios and resonance frequencies were obtained with auto regressive methods. Limit cycles were measured to examine nonlinear phenomena.

In Chapter 6, core-wide and regional stabilities were estimated for a forced circulation BWR, at the SIRIUS-F facility, by taking into account neutronic-thermalhydraulic coupling. The resultant decay ratios and resonance frequencies were compared with the ODYSY linear stability analysis code to validate the code that is generally used in BWR design.

Finally, conclusions and recommendations are given in Chapter 7.

Chapter 2

Low-Pressure Thermal-Hydraulic Stability

Abstract

Experiments were conducted to investigate two-phase flow instabilities caused by flashing in a boiling natural circulation loop with a chimney at relatively low pressure (0.1-0.5 MPa). The SIRIUS-N facility used in the experiment was designed and constructed to simulate the boiling two-phase flow of a prototypical natural circulation BWR.

The observed instability is caused by flashing-induced density-wave oscillations. This occurs because the oscillation period roughly matches the passing time of single-phase liquid in the chimney section regardless of the system pressure, heat flux, and inlet subcooling. In order to distinguish the flashing-induced instabilities from other kinds of instabilities, such as flow pattern transient oscillations, geysering, and natural circulation instability, the transient flow pattern, the relationship between oscillation period and boiling delay time, and the natural circulation driving force response are investigated in detail.

Stability maps were obtained for a range of inlet subcooling and heat fluxes at system pressures of 0.1, 0.2, 0.35, and 0.5 MPa. Instability was observed to occur within a certain range of inlet subcooling. The stability boundary at higher inlet subcooling reached when the chimney exit quality was approximately 1.1%. Flashing causes instabilities above this level only, although flashing also takes place at qualities lower than 1.1%. The flow was found to be stable below a certain heat flux regardless of the channel inlet subcooling. Moreover, the size of the region of instability in the N_{sub} - N_{pch} plane was reduced with increasing system pressure. These observations indicated that stability in the cold startup process of a reactor can be improved by pressurizing the reactor sufficiently before withdrawing the control rods (heating the reactor core).

2.1 Introduction

Design of the natural circulation cooling is a key issue in the design of simplified Boiling Water Reactors (BWRs). Cooling by natural circulation is simple, inherently safe, and results in reduced overall maintenance costs. In natural circulation BWRs, a chimney is installed on top of the core to increase the natural circulation flow rate, (see Figure 2.1). To achieve reliable cooling performance, natural circulation BWRs have to be designed such that the two-phase flow instability caused by adiabatic flashing is avoided.

Several studies have addressed two-phase flow instability during the low pressure startup

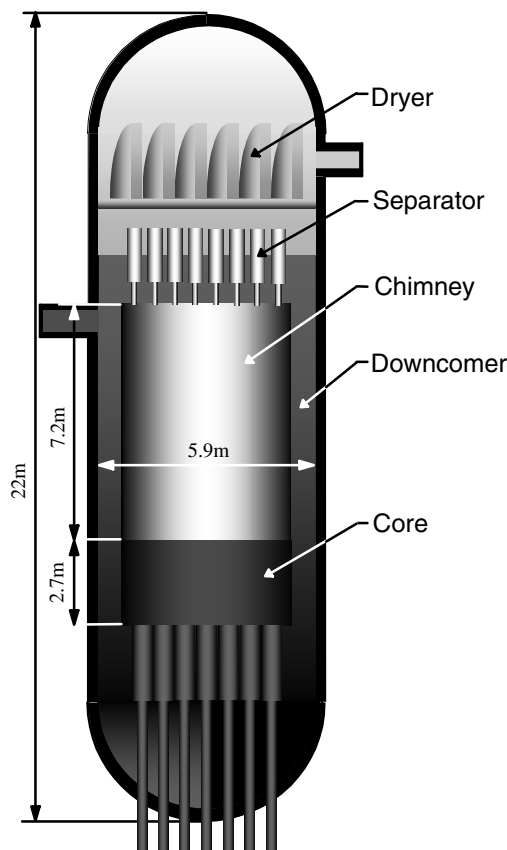


Figure 2.1: Schematic of a natural circulation BWR

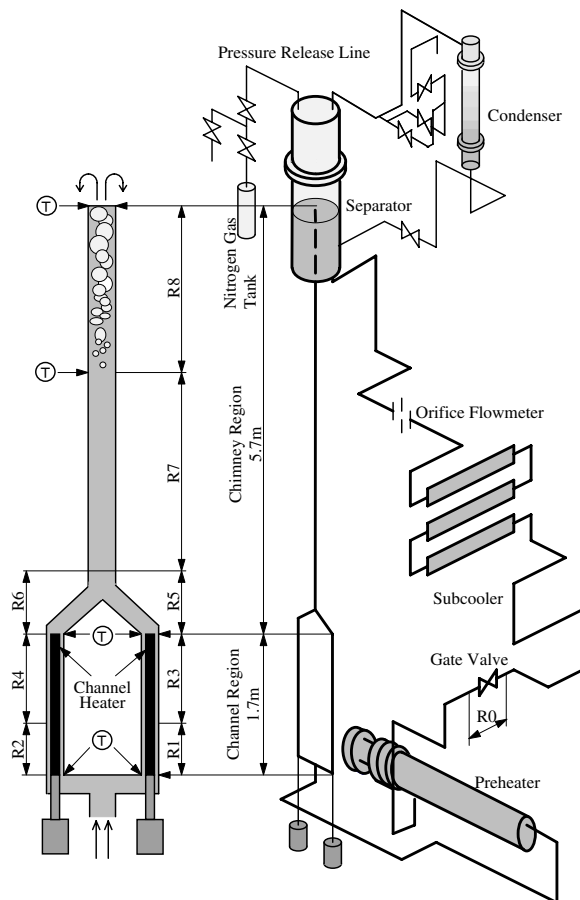


Figure 2.2: Schematic of the SIRIUS-N Facility

of natural circulation BWRs. Aritomi *et al.* (1992) and Chiang *et al.* (1993b) pointed out three types of instabilities that may occur in a boiling natural circulation loop: geysering, natural circulation oscillations, and density-wave oscillations. Although the stability of natural circulation BWRs during startup can already be estimated numerically (Lin *et al.*, 1993; Yokobori *et al.*, 1992), (Masuhara *et al.*, 1993), the mechanism that determines such instabilities has never been investigated. Van der Hagen and Stekelenburg (1995) reported that small perturbations were observed during the startup process of the Dodewaard BWR in the Netherlands.

Further detailed investigation is required to clarify such instability characteristics in relation to well-known instability classifications and the roles of the flashing in the mechanism of the instability. In order to resolve these issues, the SIRIUS-N^{*1} test facility was designed and constructed. This facility is a scaled copy of a prototypical natural circulation BWR.

This chapter addresses the characteristics and mechanism of flashing-induced instability by using the experimental results obtained from the SIRIUS-N facility at low pressures ranging from 0.1 to 0.5 MPa. The flashing-induced instability process is described by using the observed signal time traces. Furthermore, a method is proposed for a stable startup of the reactor, based on experimentally obtained stability maps.

¹SIRIUS-N is an acronym of Simulated Reactivity feedback Implemented into thermal-hydraUlic Stability loop for Natural circulation BWR

2.2 SIRIUS-N Experimental Facility

2.2.1 Thermal-hydraulic Loop

Figure 2.2 shows a schematic of the test facility. The thermal-hydraulic loop consists of two channels, a chimney, an upper-plenum (separator), a downcomer, a subcooler, and a preheater. The channel length, l_c , is 1.7 m and the chimney length, l_r , is 5.7 m, being around 70% of the actual values used in a prototypical natural circulation BWR. A heater pin is installed concentrically in each channel. The test fluid is water that has passed through an ion exchange resin.

Measurement regions of the differential pressure sensors (R1-R8) and locations for temperature measurements (T) are shown in Figure 2.2. In addition to these temperature measurements, type-K thermocouples were embedded in the surface of the sheath heater. The recirculation flow rate was measured by an orifice flowmeter attached to the downcomer. The system pressure refers to the pressure in the separator dome.

The nondimensional inlet subcooling, N_{sub} , is based on the saturation temperature related to the system pressure by the following equation:

$$N_{sub} \equiv \frac{Cp_l \Delta T_{sub}}{h_{gl}} \left(\frac{\rho_l}{\rho_g} - 1 \right). \quad (2.1)$$

Cp_l denotes the specific heat capacity at constant liquid phase pressure; ΔT_{sub} , the degree of subcooling; ρ_l and ρ_g , the liquid density and gas phase density, respectively and h_{gl} , the latent heat. N_{sub} yields a negative value when the channel inlet temperature is higher than the saturation temperature at the system pressure.

The nondimensional parameters used for scaling of the SIRIUS-N facility are listed in Table 2.1. Definitions of the nondimensional parameters are described in the nomenclature section on page 105. Detailed descriptions of the nondimensional parameters are summarized in Inada *et al.* (1995). The Froude number and flashing parameter are key values that determine the magnitude of flashing. These two values in the SIRIUS-N facility are approximately 70% of the values found in a prototypical natural circulation BWR. The facility height is limited within the availability of vertical space of the existing facility building. As a result, the height of the facility had to be less than 13 m. The value of the nondimensional drift velocity is also approximately 70% of the value common to prototypical natural circulation BWRs. However, the difference in the drift velocity may not affect the stability behavior, since the drift velocity is sufficiently smaller than the single-phase natural circulation flow rate in the range of experiments. The other parameter values agree well with the actual reactor specifications.

2.2.2 Experimental Procedure

The experimental parameters are the system pressure, heat flux and channel inlet temperature. The natural circulation flow rate is dependent on these experimental parameters. The experimental system pressures were 0.1, 0.2, 0.35, and 0.5 MPa. For 0.1 MPa, the experiments were carried out with an open valve, attached at the upper separator, because condenser performance was insufficient to maintain the system pressure at 0.1 MPa. For other system pressures, the system pressure was maintained at a specific level by controlling the performance of the condenser.

Subsequently, the channel inlet temperature was maintained at the desired value by controlling the performance of the subcooler. The system allows to perform measurements for a range

Table 2.1: Comparison of the SIRIUS-N facility with a prototypical natural circulation BWR

System Pressure, P_s	0.1 MPa		7.2 MPa	
	Reactor	SIRIUS	Reactor	SIRIUS
Target				
Flashing Parameter, N_f	67	46	0.057	0.036
Froude Number, N_{Fr}	$10.5 \cdot 10^{-4}$	$7.6 \cdot 10^{-4}$	0.058	0.053
Phase Change Number, N_{pch}	11.6	13.1	3.7	3.7
Subcooling Number, N_{sub}	9.0	9.0	0.58	0.58
Nondimensional Drift Velocity, \widehat{v}_{gj}	1.32	1.97	0.138	0.183
Ratio of Vapor to Liquid Densities, R_{gl}	$6.2 \cdot 10^{-4}$	$6.2 \cdot 10^{-4}$	0.052	0.052
Ratio of Channel Inlet to Chimney Exit Vapor Densities, $\rho_{g,ch,in} / \rho_{g,r,ex}$	2.01	1.63	1.01	1.01
Friction Coefficient in the Channel, f_{ch}	6.9	5.7	3.4	2.7
Orifice Coefficient at the Channel Inlet, κ_i	10-50	30	10 - 50	30
Orifice Coefficient at the Chimney Exit, $\kappa_{r,ex}$	20-40	21	20 - 40	21
Nondimensional Downcomer Cross-Sectional Area, \widehat{A}_d	1.05	1.11	1.05	1.11
Nondimensional Chimney Cross-Sectional Area, \widehat{A}_r	2.59	2.47	2.59	2.47
Non dimensional Chimney Length, \widehat{L}_r	3.34	3.38	3.34	3.38

of the channel inlet temperature at one- or two-degree Kelvin intervals. Experiments were repeated to verify reproducibility. The time-average and standard deviation of the acquired data were correlated over four oscillation periods.

2.2.3 Void Fraction Estimation

In order to investigate the thermal-hydraulic stability of a boiling two-phase flow driven by natural circulation, the void fraction must be estimated accurately, since that determines the flow rate. In this study, the void fraction was calculated in each measured section using the measured differential pressure, inlet velocity, and inlet temperature. The analysis in estimating the void fraction is based on :

1. The flow is in a one-dimensional steady-state condition. This assumption is valid only if the integration time in the acquisition system (10 ms) is sufficiently shorter than the flow oscillation period ($\tau_{fo} > 10$ s).
2. The following pressure losses are taken into account: acceleration, gravitation, wall friction, and local pressure losses.
3. Each measurement region (denoted as R1 through R8 in Figure 2.2) was divided into a liquid single-phase flow part and a boiling two-phase flow part, separated by a boiling boundary. The effect of subcooled boiling is neglected, since flashing mainly takes place in the adiabatic chimney.
4. Thermo-physical properties refer to those under saturated conditions for the system pressure, except that the liquid density in the connecting pipes of the differential pressure measurement system (DPMS) is determined by an experimentally obtained correlation.

The momentum equation, thereby using the above assumptions, yields:

$$\frac{d}{dz} \left[\frac{1}{2} \alpha \rho_g u_g^2 + \frac{1}{2} (1 - \alpha) \rho_l u_l^2 \right] + \frac{d}{dz} P + M_{wall} + M_{local} + [\alpha \rho_g + (1 - \alpha) \rho_l] g = 0. \quad (2.2)$$

In this equation, α is the void fraction, ρ the density, P the pressure and g the gravitational acceleration. The subscripts g and l denote vapor and liquid phases respectively. The terms on the left-hand side of the equation correspond to acceleration, total pressure, wall friction, local (concentrated) friction, and gravitational losses, respectively. The wall friction loss, M_{wall} , is given by:

$$M_{wall} = \begin{cases} \frac{f_{1\phi}}{2d} \rho_l u_{in}^2 & \text{(single-phase flow)} \\ \frac{f_{2\phi,g}}{2d} \alpha \rho_g u_g^2 + \frac{f_{2\phi,l}}{2d} (1 - \alpha) \rho_l u_l^2 & \text{(two-phase flow)} \end{cases} \quad (2.3)$$

The loss coefficient was estimated on the basis of Blasius's correlation for liquid single-phase flow ($f_{1\phi}$), and Martinelli-Nelson correlation with Jones's fitting for two-phase flow ($f_{2\phi}$). The local pressure loss, M_{local} , is expressed as follows:

$$M_{local} = \begin{cases} \sum \frac{\kappa_{1\phi,i}}{2} \rho_l u_{in}^2 \delta(z - z_i), & \text{(single-phase flow)} \\ \sum \left[\frac{\kappa_{2\phi,g,i}}{2} \alpha \rho_g u_g^2 + \frac{\kappa_{2\phi,l,i}}{2} (1 - \alpha) \rho_l u_l^2 \right] \times \delta(z - z_i), & \text{(two-phase flow)} \end{cases} \quad (2.4)$$

A single-phase flow experiment was conducted to determine the local friction coefficients of the orifices and changes in the flow area. The measured values of these coefficients are summarized in Table 2.1. Detailed experimental procedures are summarized in Furuya *et al.* (1995). Assuming thermal equilibrium conditions, the non-boiling length (distance between the inlet of the measurement region and the boiling boundary), $Z_{1\phi}$, and the boiling length, $Z_{2\phi}$, is expressed on the basis of energy equation as:

$$Z_{1\phi} = \frac{\rho_l C_p l \Delta T_{sub,in} u_{in} A_c}{\pi D q''}, \quad (2.5)$$

$$Z_{2\phi} = l - Z_{1\phi}. \quad (2.6)$$

The u_{in} denotes the velocity at the channel inlet, A_c is the flow area of the channel, D denotes the heater diameter and q'' refers to the heat flux, l is length of measurement region. The liquid and vapor velocities are related by a drift flux model (Ishii, 1977). The differential pressure of the channel region, $P_{ex} - P_{in}$, is expressed as the measured value of the differential pressure measurement system (DPMS), ΔP_{DPMS} :

$$\Delta P_{DPMS} = P_{ex} - P_{in} + \rho_{DPMS} g (Z_{1\phi} + Z_{2\phi}), \quad (2.7)$$

where ρ_{DPMS} is the liquid density in the connecting pipes of the DPMS, which is higher than that under saturated conditions because the liquid flow is stagnant and at a lower temperature (due to heat loss). Neglecting this effect would result in a large error in the estimated void fraction, especially when the void fraction is low and the system pressure is high. Therefore, ρ_{DPMS} was determined experimentally as a function of ambient temperature and the local saturation temperature.

The void fraction in the two-phase region, $\alpha_{2\phi}$, is obtained by integrating equation (2.2) over the liquid single-phase and two-phase regions with equation (2.7) as a constraint. This procedure requires an iterative method, since coefficients in the momentum equation are functions of the void fraction. The total void fraction in each measurement region of the DPMS, α_{total} , is then calculated as follows:

$$\alpha_{total} = \frac{z_{2\phi}}{z_{1\phi} + z_{2\phi}} \alpha_{2\phi} \quad (2.8)$$

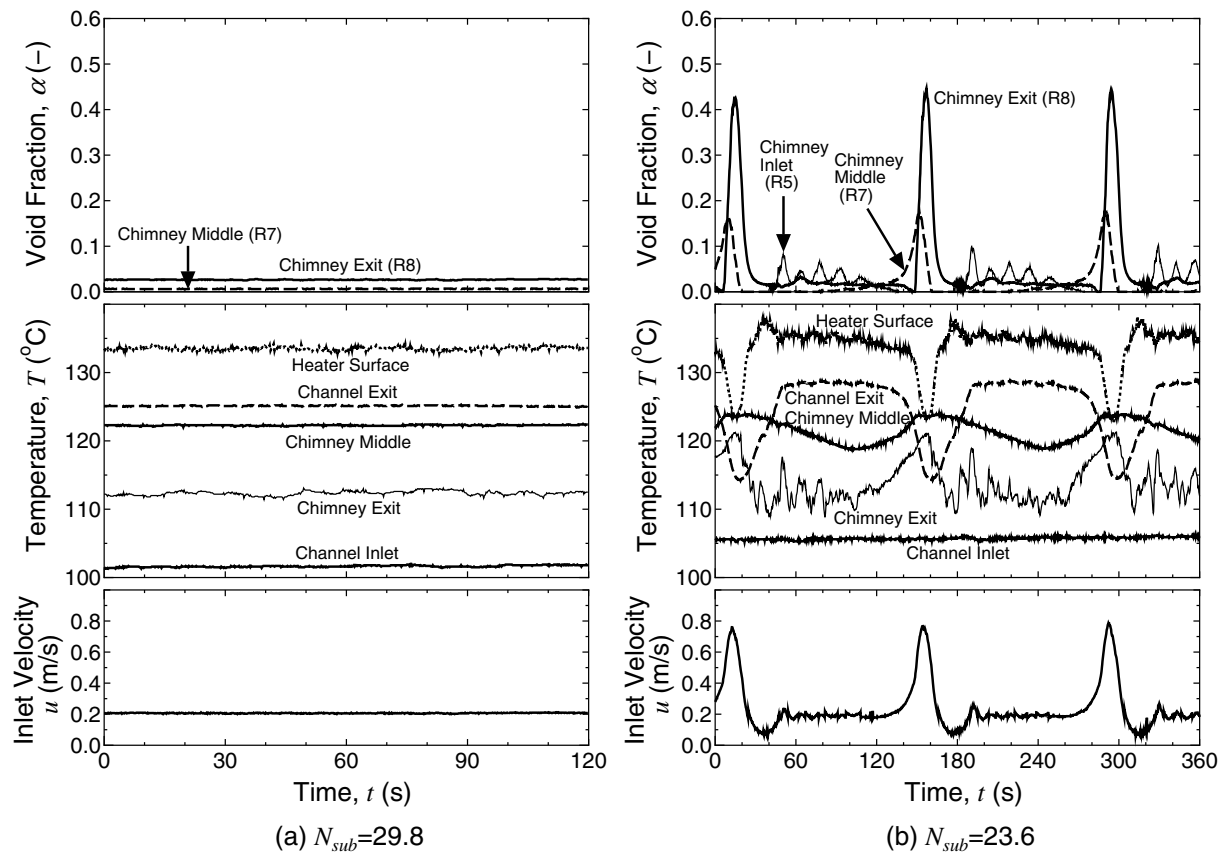


Figure 2.3: Time traces of signals measured when $P_s = 0.2$ MPa and $q'' = 53$ kW/m². Figure (a) shows stable flow condition. Void fractions, temperatures, and inlet velocity are constant in time. Void fractions of 0.6% and 2.7% appear in the chimney, generated by flashing in the chimney center and exit (R8). Figure (b) shows intermittent oscillations when the channel inlet temperature exceeds a certain value. Temperatures at the chimney inlet and exit are out of phase.

2.3 Experimental Results

2.3.1 Signal Time Traces

In this section, the measured time trace signals for different operational conditions are discussed. More specifically, the phenomenon of flashing is investigated.

Figures 2.3 (a)-(d) show time traces of the signals acquired when $P_s = 0.2$ MPa and $q'' = 53$ kW/m². The graphs (from top to bottom) show the void fractions in the chimney, the temperature, and the channel inlet velocity in time. Each figure was obtained at a different channel inlet subcooling condition: (a) stable condition, (b) intermittent but periodic oscillation, (c) sinusoidal oscillations, and (d) stable condition. Similar waveforms were observed at other system pressures and heat fluxes.

As for the stable condition at the higher subcooling which is shown in Figure 2.3 (a), temperatures at the chimney inlet (= the channel exit) and center may coincide with the local saturation temperatures. When the flow rate is small, the temperature at the chimney exit indicates the temperature in the separator dome, which is, in fact, somewhat lower than the fluid temperature at the chimney exit. Although void fractions of 0.6% and 2.7% were generated by flashing in the chimney center (corresponding to region R7, see Figure 2.2) and exit (R8), respectively, both the void fractions and the temperatures remained constant. Therefore, no instabilities were found.

When the channel inlet temperature exceeds a certain value, the channel inlet flow rate and

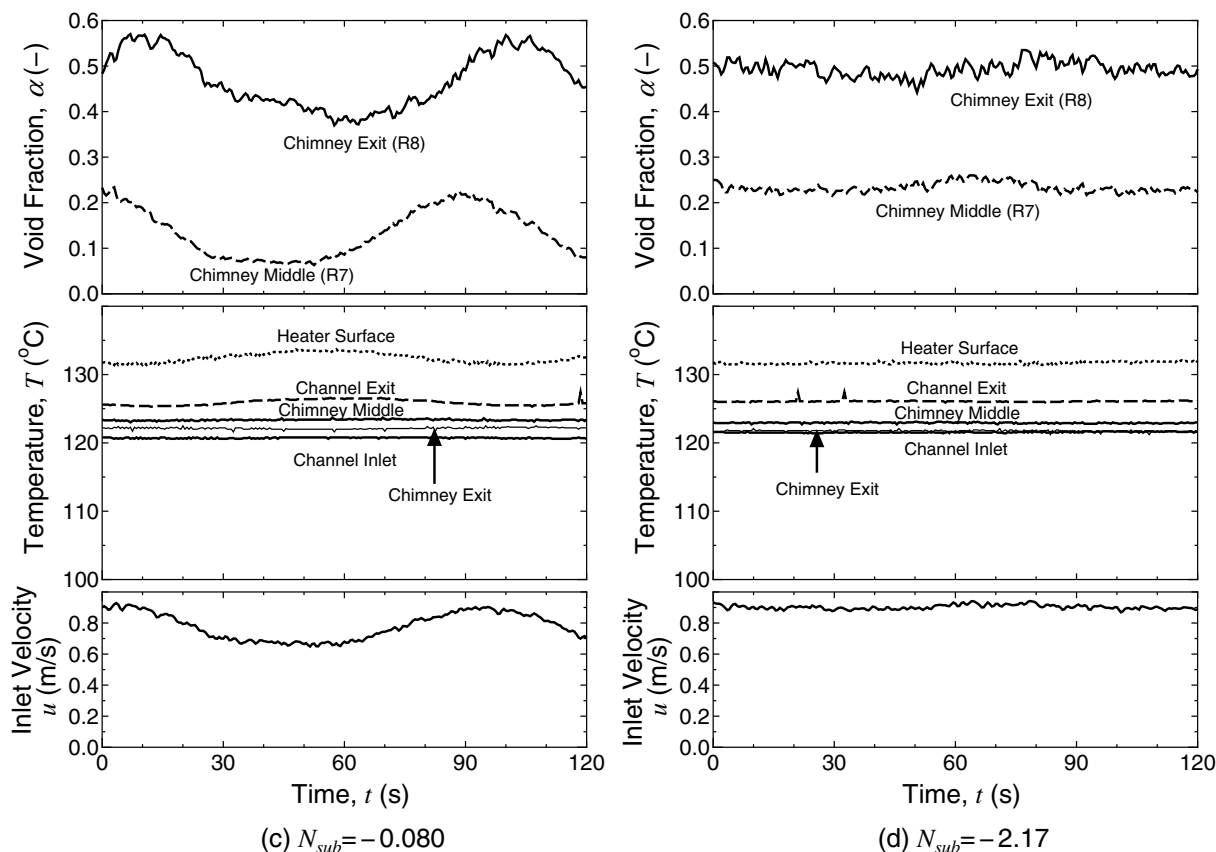


Figure 2.3: Time Traces of Signals At $P_s = 0.2$ MPa And $q'' = 53$ kW/m² (Cont'd). Figure (c) shows sinusoidal oscillations. The temperatures at the chimney inlet and chimney exit are out of phase. The oscillation amplitude decreases as inlet subcooling decreases. As shown in Figure (d), the flow stabilizes as the temperature approaches its local saturation condition at the chimney inlet.

the void fractions pulsate intermittently as shown in Figure 2.3 (b). This phenomenon will be discussed later. Although the channel inlet temperature was kept constant, temperatures pulsed because of flow oscillations induced by flashing. Note that the time scale in Figure 2.3 (b) is three times larger than the time scale in the other figures.

A further increase in inlet temperature decreases the oscillation period and amplitude, resulting in a sinusoidal curve as shown in Figure 2.3 (c). In both oscillatory conditions (shown in Figure 2.3 (b) and (c)), a phase lag occurs between the void fractions at different locations in the chimney. Flashing bubbles are initiated in the chimney inlet for $N_{sub} = 23.6$ and in the chimney center for $N_{sub} = -0.080$. The bubble volume increases and travels through the chimney toward its exit. Moreover, an increase in the inlet temperature reduces the flow rate amplitude, void fraction, and temperature fluctuations. Finally, the flow stabilizes as the temperature approaches its local saturation condition at the chimney inlet as shown in Figure 2.3 (d).

As mentioned in Section 2.2.2, the experiments were performed by increasing the inlet temperature. In order to investigate the influence of the experimental procedure on the stability boundary, the experiments were also carried out by decreasing inlet temperature. The stability boundaries obtained for increasing and decreasing inlet temperature agreed well. In other words, the stability boundary remained the same whether it was determined from the stable or from the unstable side of the boundary. This fact indicates that the nonlinearity of the instability phenomenon caused by flashing is small when the experimental parameter is close to the stability boundary.

The interaction between two parallel heated channels was investigated to determine the

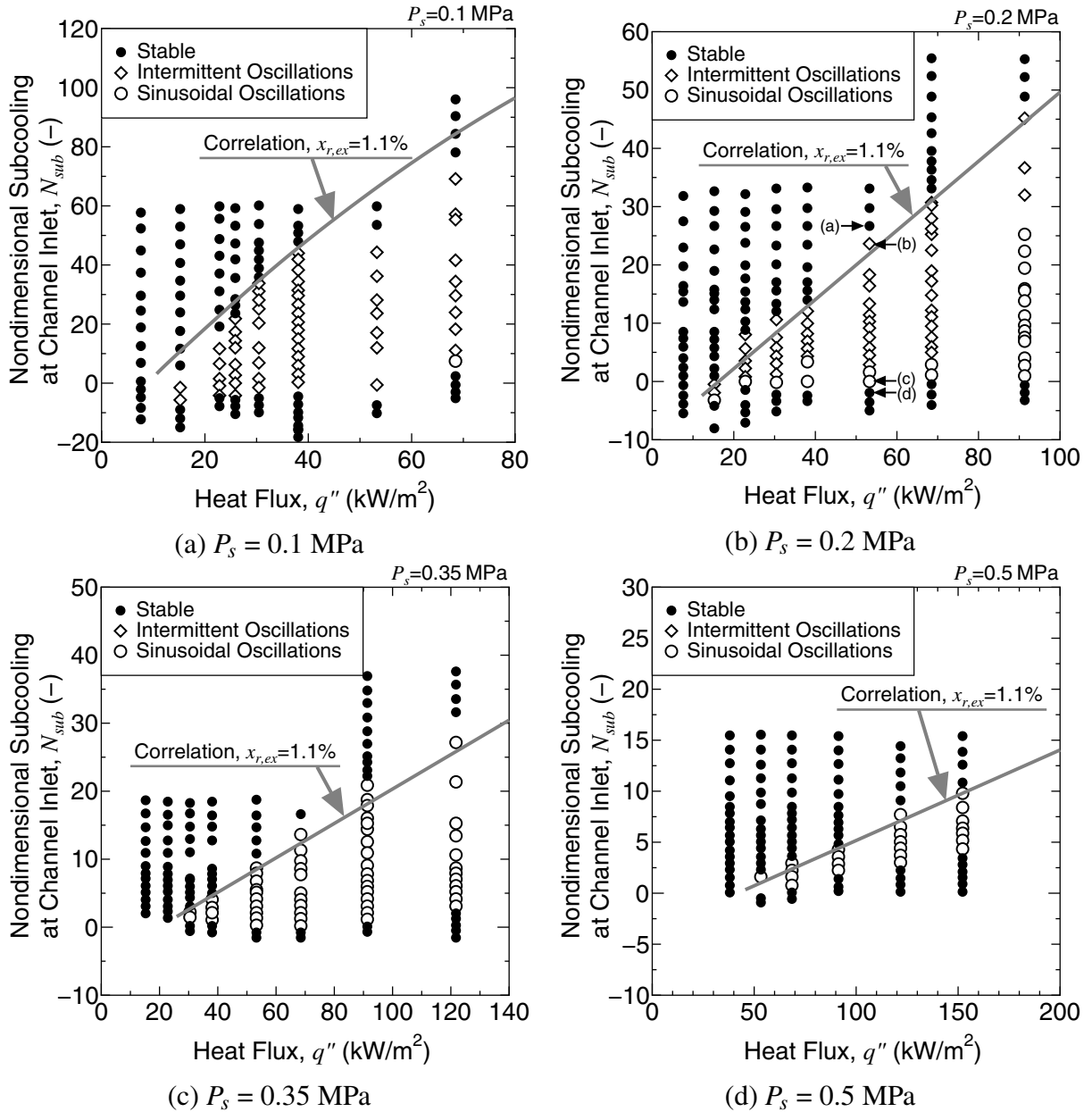


Figure 2.4: Stability maps for a range of heat fluxes and inlet subcooling. For every system pressure used in the study (Figures (a)-(d)), instability occurred within a certain range of the inlet subcooling. The unstable range grows as the heat flux was increased. The stability boundary at higher subcooling agrees well with the correlation ($x_{r,ex} = 1.1\%$), as is discussed in further detail in Section 2.6.

instability mode (in phase or out of phase). The oscillation mode was found to be in phase; no significant phase lags and amplitude differences were observed between the channels for all tested conditions. As discussed later, this lack of phase lag or amplitude difference is directly related to bubbles generated by flashing in the chimney and not to phenomena occurring in the two heated sections.

2.3.2 Stability Maps for Different Pressures

In order to investigate the effects of the experimental parameters (system pressure, heat flux, and inlet subcooling), stability maps were obtained. Figures 2.4(a)-(d) show the stability maps for nondimensional inlet subcooling and heat flux at system pressures of 0.1, 0.2, 0.35, and

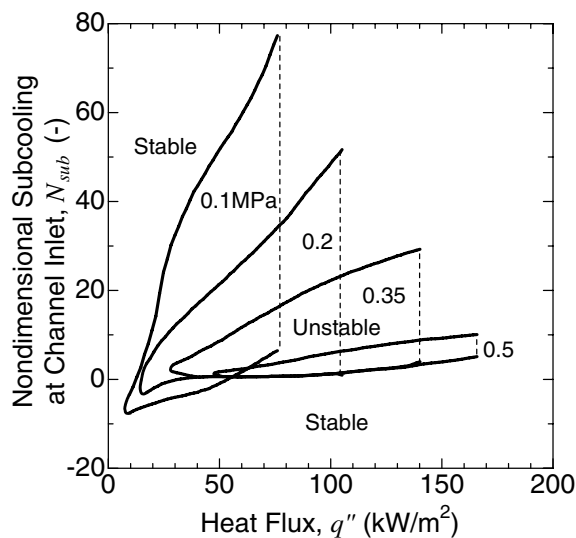


Figure 2.5: Stability maps for $P_s = 0.1, 0.2, 0.35,$ and 0.5 MPa. Instability was observed within the interior region surrounded by solid lines. The region of stability increased in size as the system pressure was increased. No instabilities were observed below a certain heat flux. This region is of practical importance, because one can start up a reactor, from cold state to high power conditions without encountering a region of instability.

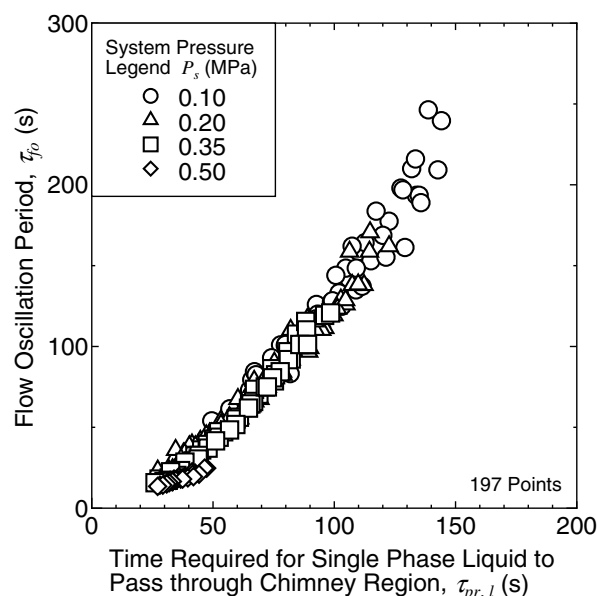


Figure 2.6: The relationship of the enthalpy wave propagation time and the oscillation period. All unstable data correlate well in a single curve regardless of system pressure, heat flux, and inlet subcooling. The oscillation period is nearly one to two times the time required for the fluid to travel through the chimney section, which is typical for density-wave oscillations.

0.5 MPa. In the figures, the horizontal axis refers to the heat flux instead of the phase change number in order to avoid a busy graph (see e.g. Figure 3.15 all points are situated near the zero-quality line).

The flow conditions were classified and plotted using different symbols, based on the acquired signal time traces. The symbol ‘●’ means stable condition; ‘◇’, means intermittent but periodic oscillations, as shown in Figure 2.3 (b); and ‘○’, means sinusoidal oscillations, as shown in Figure 2.3 (c). In this study, the flow condition was classified as stable when the root mean square (r.m.s.) of the inlet velocity was less than 10% of the average inlet velocity. This threshold value is often applied in thermal-hydraulic stability research.

Figure 2.4 (b) shows the stability map at 0.2 MPa. Symbols (a)-(d) in Figure 2.4 (b) correspond to the conditions of the representative signal time traces in Figures 2.3 (a)-(d). The solid line in the figure represents a correlation indicating conditions with an exit quality of 1.1%, which will be described in Section 2.6.

As mentioned above, instability occurs within a certain range of the inlet subcooling. Figure 2.4 shows that the unstable range enlarges as the heat flux increases. It is interesting to note that there were no instabilities observed below 8 kW/m^2 . This region is of practical importance: one can start up a reactor without encountering an area of instability.

Intermittent oscillations occurred at higher subcooling numbers, whereas sinusoidal oscillations were observed in the lower subcooling region. The border between intermittent and sinusoidal oscillations remained unclear, as the oscillation period and amplitude continuously changed with inlet subcooling.

When the stability map at 0.2 MPa is compared with those at other system pressures, in-

intermittent oscillations are observed mainly under unstable conditions at 0.1 MPa, as shown in Figure 2.4 (a). However, only sinusoidal oscillations were observed at 0.35 and 0.5 MPa, as shown in Figures 2.4 (c) and (d). This occurs because flashing becomes more dominant as the pressure decreases. Note that both scales are different in Figures 2.4 (a)-(d).

Figure 2.5 shows the stability boundaries at system pressures of 0.1, 0.2, 0.35, and 0.5 MPa, as determined from the data in Figure 2.4. Instability is shown within the interior region surrounded by solid lines. It is obvious from this figure that the stable region increases in size as the system pressure goes up. Other studies reported the same tendency (Masuhara *et al.*, 1993; Manera and Van der Hagen, 2003). Furthermore, as the system pressure increases, the region of instability shifts to a higher heat flux. According to the stability map, one can conclude that stability can be improved during the cold startup process of a reactor by pressurizing the reactor sufficiently before increasing reactor power.

2.4 Instability Mechanism

The types of the instabilities which should be considered in this facility configuration are: flow pattern transition instability, geysering, natural circulation oscillations, and density-wave oscillations (Bouré *et al.*, 1973). Acoustic oscillation is excluded because its mechanism is related to pressure-wave resonance with a period much shorter than that of the oscillations observed in this experiment (ranging from 13 to 250 seconds).

Pressure drop oscillations is the dynamic instability caused by a dynamic interaction between a heated channel and a compressible volume. Pressure perturbations in the separator dome are, however, relatively small ($\leq 0.5\%$ of P_s). Pressure drop oscillations are excluded for this reason. Hereafter, the discussions on possible instability mechanisms is therefore restricted to density-wave oscillations, geysering, flow pattern transition instability, and natural circulation oscillations.

Density-wave oscillations can be induced by multiple regenerative feedback among the flow rate, vapor generation rate, and pressure drops. Experiments show that the oscillation period is approximately one-and-a-half to two times the period required for the fluid to travel through the pipe (Bouré *et al.*, 1973).

Figure 2.6 illustrates the relationship between the flow oscillation period, τ_{fo} , and the time required for the fluid to pass through the chimney region, $\tau_{pr,l}$, which was calculated as the volume, V_r , divided by the average volumetric flow rate of the liquid, $\langle Q_r \rangle$:

$$\tau_{pr,l} = \frac{V_r}{\langle Q_r \rangle}. \quad (2.9)$$

Time $\tau_{pr,l}$ accounts only for the chimney region, since the density-waves (known as the void-sweep phenomenon) propagate mainly in the chimney region. All unstable data (197 points) correlate closely in a single curve, regardless of system pressure, heat flux, and inlet subcooling. In addition, the oscillation period is roughly one-and-a-half to two times the period required for the fluid to travel through the chimney region. These characteristics are typical for density-wave oscillations. Intermittent (but periodic) and sinusoidal oscillations in this experiment are both included in the density-wave oscillation category, because data for both oscillations correlate well on the same curve.

Figure 2.7 illustrates the proposed process for flashing-induced density-wave oscillations. Imagine an adiabatic vertical pipe with a heater rod inserted from the bottom. Suppose that the pressure at the top of the chimney is 0.1 MPa (corresponding to a saturation temperature of approximately 100°C) and that the length of the chimney is 10 m. The pressure at the bottom

of the chimney will then be approximately 0.2 MPa because of the static head of water (with a saturation temperature of approximately 120°C). The colors in Figure 2.7 indicate water temperature from cold (blue) to hot (red). The magnitudes of the arrows at the bottom indicate the flow rate. Flashing-induced density-wave oscillation is believed to occur as a result of the steps outlined in Figure 2.7.

- (a) Water heated by the heater (at 110°C for instance) flows into the chimney.
- (b) Boiling is initiated at a location where the water temperature exceeds the local saturation temperature.
- (c) A decrease in the static head of water immediately promotes further evaporation, a phenomenon known as flashing.
- (d) The natural circulation flow rate increases due to an enlarged vapor volume, resulting in an outflow of steam bubbles. The temperature at the chimney inlet becomes relatively low in turn because of the short dwell time in the heated region.
- (e) After the chimney is filled with cold water, the flow rate decreases and the temperature at the chimney inlet becomes relatively high because of the long dwell time in the heated region caused by flow stagnation. The process then repeats itself beginning with process (a).

The periods of flashing and bubble outflow, corresponding to processes (b) through (d), are relatively short compared to the timescale of the entire loop. It is found that the oscillation period indeed almost agrees with the time required for the single-phase liquid to pass through the chimney region, as shown in Figure 2.6.

2.5 Comparison with Other Kinds of Instabilities

In the previous section, the observed oscillations were shown to be caused by the flashing-induced density-wave oscillations, and a process for flashing-induced density-wave oscillations (DWO) was proposed. This section elaborates on the characteristics of flashing-induced density-wave oscillations by comparing them with other kinds of instabilities.

2.5.1 Geysering

Geysering has been observed in a variety of closed end (or forced flow at low flow rate) vertical columns of liquid which are heated at the base. The process can be broken down into three sub-processes: boiling delay, condensation (or expulsion of vapor) and liquid returning to the main column of liquid (Nakanishi *et al.*, 1978). Studies have also shown that the period of flow oscillation, τ_{fo} , is nearly equal to the boiling delay time, τ_{bd} , because the boiling delay time is much longer than that of the other two sub-processes. Since geysering has not yet been clearly defined for natural circulation flow in relation to density-wave oscillations, geysering characteristics in a natural circulation system have been assumed to be the same as those in a closed end or forced circulation system. The boiling delay time is defined as the time required for fluid having some degree of subcooling $\Delta T_{sub,in}$ to be heated to saturation temperature, based on the pressure at the channel inlet. It is expressed by the following equation (Nakanishi *et al.*, 1978):

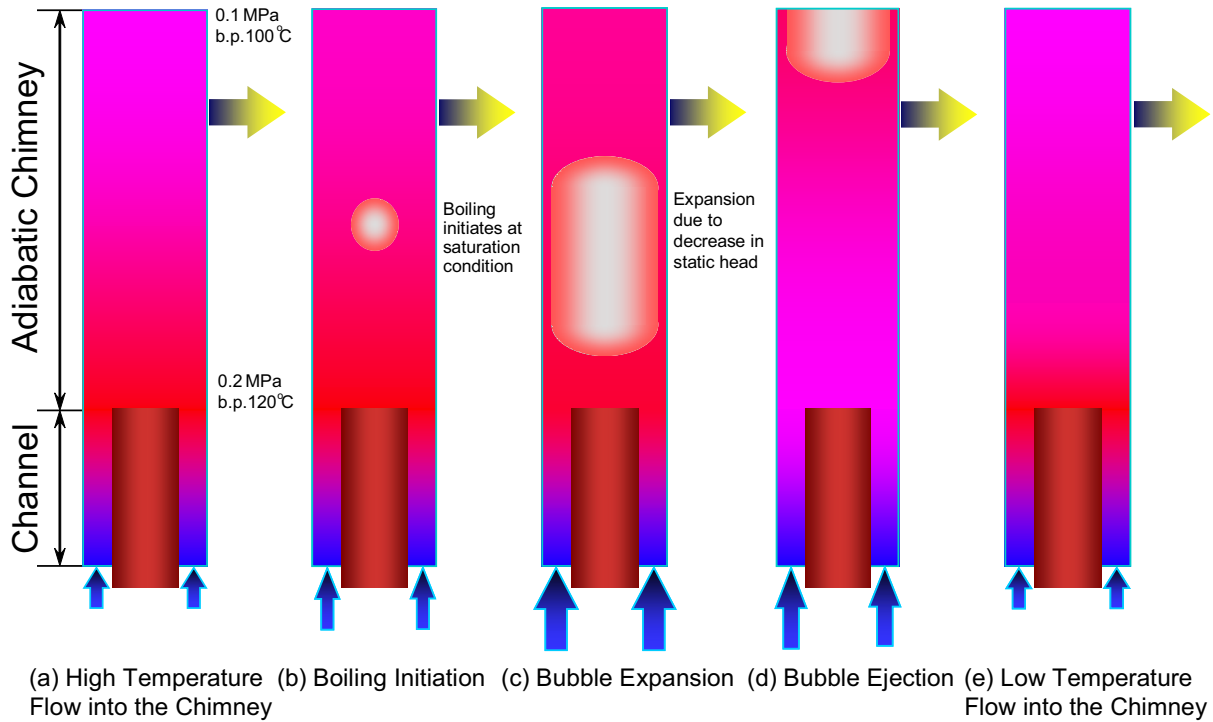


Figure 2.7: Proposed process for flashing-induced density-wave oscillations. Consider an adiabatic vertical pipe with a heater rod inserted from the bottom. The colors in the figure indicate the water temperature from cold (blue) to hot (red). The magnitudes of the arrows at the bottom indicate the flow rate. Flashing-induced density-wave oscillation is believed to occur through the following steps: (a) Water heated by the heater flows into the chimney. (b) Boiling occurs where the water temperature exceeds the local saturation temperature. (c) A decrease in the static head of water immediately promotes further evaporation (i.e., the flashing phenomenon). (d) The natural circulation flow rate increases as a result of the enlarged vapor volume, resulting in an outflow of steam bubbles. (e) After the chimney is filled with cold water, the flow rate decreases. Then the process starts all over again from step (a).

$$\tau_{bd} = \frac{\rho_{l,in} C_{pl,in} \Delta T_{sub,in} A_c l_c}{q''} \quad (2.10)$$

Figure 2.8 depicts the relationship between boiling delay time and the flow oscillation period. The density, $\rho_{l,in}$, and the specific heat capacity at constant pressure, $C_{pl,in}$, both depend on the channel inlet temperature. A_c and l_c are the flow area and length of the heated section, respectively. The oscillation period was found to be one order of magnitude longer than the boiling delay time and increased in proportion to the boiling delay time. Based on these results, we can conclude that the flow oscillations are not caused by geysering. Two additional facts also support the conclusion that geysering does not cause the instability: (1) the flow rate is large enough to prevent formation of a superheated water layer; and (2) there is not enough subcooled water to condense large bubbles, as shown in Figures 2.3 (b) and (c).

2.5.2 Flow Pattern Transition Instability

Flow pattern transition instabilities have been postulated to occur when the flow conditions are close to the point of transition between bubbly flow and annular flow pattern. Nayak *et al.* (2003) performed numerical analyses and took into account flow pattern transition criteria for a natural circulation heavy-water-moderated boiling light water cooled reactor. Analytical results

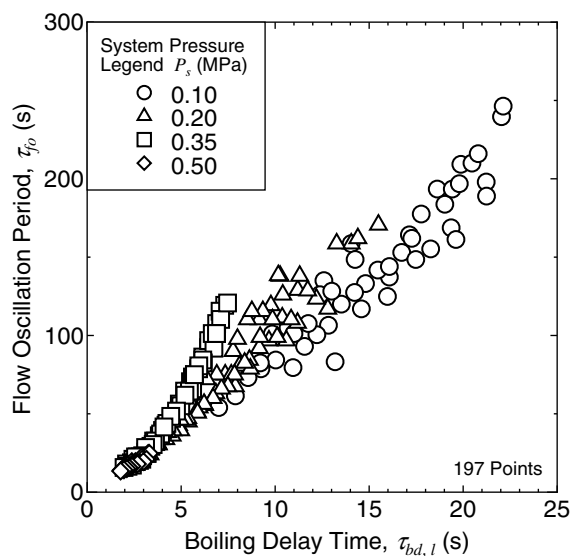


Figure 2.8: The relationship between boiling delay time and the oscillation period. The oscillation period was one order of magnitude longer than the boiling delay time. This shows that the flow oscillations were not caused by geysering.

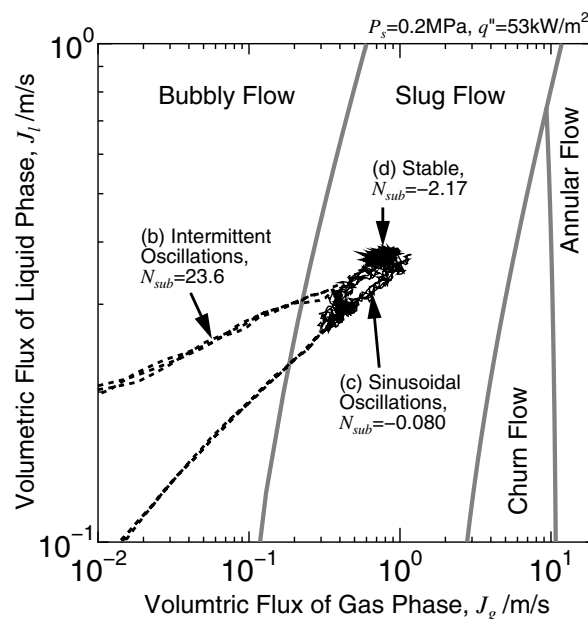


Figure 2.9: Transient flow patterns plotted for three cycles show a change from a bubbly flow pattern to a sluggish one. The flow pattern never changed to a churn or annular flow pattern.

show that increasing the pressure and decreasing the inlet subcooling has a stabilizing effect on the flow pattern transition instability. Although the facility used in this study was roughly as high as a standard natural circulation BWR, the chimney diameter of the facility was made relatively small for accurate demonstration of high quality flow patterns, such as churning and annular flow. The transient flow pattern was examined to clarify its relationship with flow pattern transition instability.

Figure 2.9 shows experimentally obtained transient flow patterns drawn according to the method used in Mishima-Ishii's diagram (Mishima and Ishii, 1984). The experimental data are plotted for approximately three oscillation cycles at the chimney exit region, R8 (see Figure 2.2), when $P_s = 0.2$ MPa and $q'' = 53$ kW/m². Labels (b), (c), and (d) correspond to those in figures 2.3 (b), (c), and (d). Because of the low void fraction, no plot is shown for a highly subcooled stable condition as shown in 2.3(a).

The flow pattern changed from liquid single-phase flow to slug flow during the intermittent oscillations. Boiling always took place in the chimney during the sinusoidal oscillations, so the flow regime was slug flow and the locus resembles an ellipse. Decreasing inlet subcooling reduces the area of the ellipse, and the flow then stabilizes. Consequently, the flow pattern never changed to a churn or annular flow pattern, hence flow pattern transition instabilities were not found in our experiments.

2.5.3 Natural Circulation Oscillation

Chiang *et al.* (1993b) observed an interesting flow oscillation phenomenon in a loop having a section in which bubbles could accumulate. They called this phenomenon "natural circulation oscillation," and postulated the following mechanism for it:

- (a) Vapor accumulates in an unheated pipe (connecting the outlet plenum to the separator

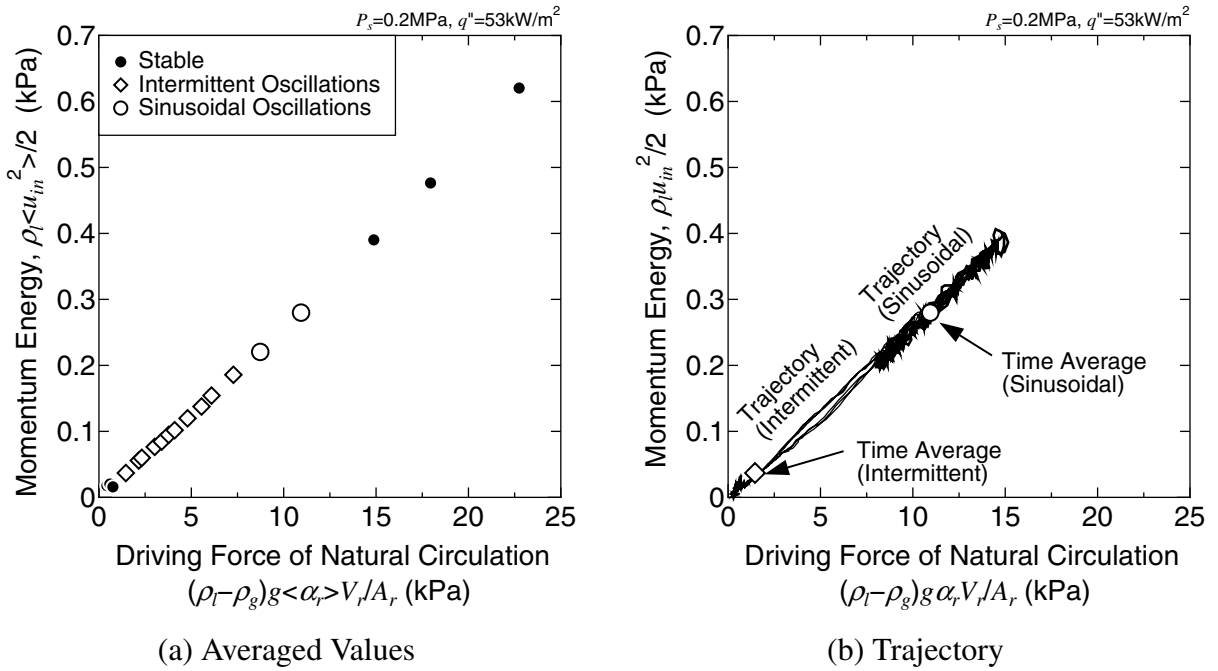


Figure 2.10: Momentum response to a natural circulation driving force. Figure (a) shows that the average values form a straight line that passes through the origin in such a way that the static characteristics are well correlated whether the flow condition is stable or unstable. Figure (b) shows that the trajectory follows the straight line of the static characteristics. Therefore, the resulting oscillations are not caused by natural circulation oscillations for which the trajectory would be ellipsoidal.

tank, which consists of vertical and horizontal pipes), when the evaporation rate is insufficient.

- (b) Bubbles coalesce with the incoming vapor, and then the hydrostatic head decreases gradually.
- (c) An increase in the flow rate flushes the accumulated vapor and water fills in.
- (d) The hydrostatic head increases and therefore the circulation rate decreases (resulting in a return to process (a)) and then the process repeats itself.

This phenomenon repeats periodically. Although bubbles cannot accumulate in the present SIRIUS-N facility, a method to investigate the natural circulation oscillation was proposed. Figure 2.10 illustrates the response of the momentum energy to the natural circulation driving force at $P_s = 0.2 \text{ MPa}$ and $q'' = 53 \text{ kW/m}^2$. Natural circulation was induced by a decrease in apparent density as a result of vapor generation. Therefore the driving force can be expressed as $(\rho_l - \rho_g)g\alpha_r V_r/A_r$. The subscript 'r' denotes the value defined at the chimney. The momentum energy is expressed as $\rho_l u_{in}^2/2$.

The average values are plotted in Figure 2.10(a). The values form a straight line that passes through the origin. This means that static characteristics are well correlated under both stable and unstable conditions.

The trajectory is shown in Figure 2.10(b) for representative intermittent and sinusoidal oscillations, as shown in Figures 2.3(b) and (c). The trajectory follows the straight line of the static characteristics, as illustrated in Figure 2.10(a). Apparently, the response of the momentum energy to the natural circulation driving force was very fast, so vapor did not accumulate in the

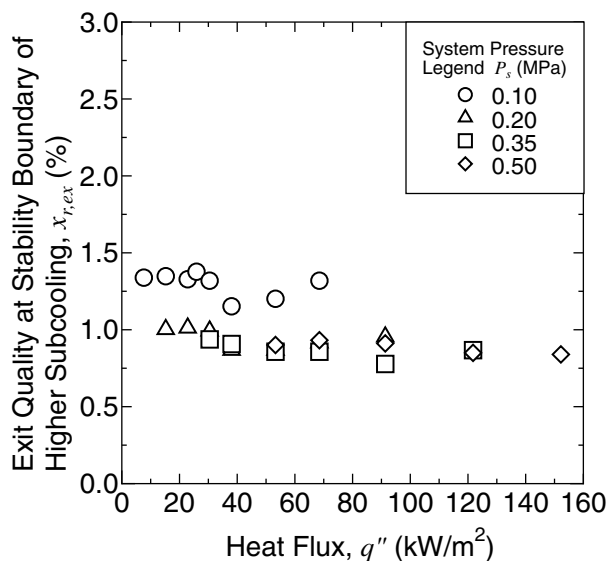


Figure 2.11: Exit quality at the stability boundary for higher subcooling. Variations of $x_{r,ex}$ are very small, ranging from 0.9% to 1.3% regardless of the heat flux and system pressure. Flashing occurs when the exit quality exceeds zero at the chimney exit. Flow oscillations caused by flashing occur for the exit qualities higher than approximately 1.1%.

two-phase section. Since the trajectory is not ellipsoidal, we conclude that natural circulation oscillations are absent here.

2.6 Stability Boundary and Stability Estimation for the ESBWR

The unstable region shown in Figure 2.5 can be considered to be composed of two lines at higher and lower subcooling. Those two lines may be considered to merge near the origin. In this section, this linear approximation of the stability boundary at higher subcooling is investigated.

Figure 2.11 shows the exit quality at the stability boundary for the upper line, $x_{r,ex}$, versus the heat flux. $x_{r,ex}$ is estimated as follows:

$$x_{r,ex} = \frac{h_{ch,ex} - h_{l,r,ex}}{h_{g,r,ex} - h_{l,r,ex}} \quad (2.11)$$

where $h_{g,r,ex}$ and $h_{l,r,ex}$ are the vapor and liquid saturation enthalpy at the chimney exit respectively (based on the system pressure). $h_{ch,ex}$ is the enthalpy estimated by the pressure and temperature at the channel exit. The enthalpy defined at the channel exit is used in place of that defined at the chimney exit, because these two values are almost the same under the adiabatic condition. Remarkably, variations in $x_{ch,ex}$ are very small, ranging from 0.9% to 1.3% regardless of heat flux and system pressure. Flashing occurred when the exit quality exceeded zero at the chimney exit. For flow oscillations to be caused by flashing, the exit quality should probably be higher than approximately 1.1%. For a reference, a constant exit-quality line ($x_{r,ex} = 1.1\%$) is drawn by the homogeneous equilibrium mixture (HEM) analysis in the stability maps in Figure 2.4. Flashing induces flow oscillations below this line in the stability map.

2.7 Conclusions

- The observed instability at low pressures was shown to be related to flashing-induced density-wave oscillations, as the oscillation period correlated well with the passing time of a single-phase liquid in the chimney section regardless of system pressure, heat flux, or inlet subcooling.
- Geysering is not occurring in this experiment, since the oscillation period was found to be one order of magnitude longer than the boiling delay time.
- When the instability was found, the flow pattern in the chimney never changed to a churn or annular flow pattern. Therefore, the observed instability was not caused by flow pattern transient oscillations.
- The response of the momentum energy to the natural circulation driving force was very fast. This indicates that the vapor did not accumulate in the two-phase section. Therefore, natural circulation oscillations were absent in this experiment.
- Stability maps were obtained for a range of inlet subcooling and heat fluxes at system pressures of 0.1, 0.2, 0.35, and 0.5 MPa. Instability was observed to occur within a certain range of inlet subcooling. The stability boundary at higher inlet subcooling agreed well with the condition where the chimney exit quality was approximately 1.1%. Flashing induces instabilities above this quality, though flashing also occurs at low quality.
- The flow became stable below a certain heat flux regardless of the channel inlet subcooling. The region of stability grew in size as the system pressure was increased. Based on these results, stability can be improved in the cold startup process of a reactor by pressurizing the reactor sufficiently before increasing reactor power.

Subsequent experiments were extended to study the stability at relatively high system pressures (1.0 - 7.2 MPa) with the same SIRIUS-N facility. The differences between thermal-hydraulic instabilities occurring at low and high pressures are discussed in Chapter 3.

Chapter 3

High-Pressure Thermal-Hydraulic Stability

Abstract

Experiments were conducted to investigate two-phase flow instabilities in a boiling natural circulation loop with a chimney at relatively high pressure (1 - 5MPa). The SIRIUS-N facility used in the experiment was designed and constructed to simulate the boiling two-phase flow of a prototypical natural circulation BWR. The obtained stability map demonstrates that the rated operating condition of the ESBWR is found to have significant stability margin (approximately 64 K of inlet subcooling) to the unstable region.

Two distinct branches are found in relation of the oscillation period to liquid passing time in the chimney, indicating that the driving mechanisms of the instabilities are different for low and high pressures. The demarcation lies between 0.5 MPa and 1.0 MPa, since flashing diminishes with increasing pressure. In contrast to the flashing induced density wave oscillations at low system pressures, the oscillation period correlates well with the passing time of bubbles in the chimney section regardless of the system pressure, the heat flux, and the inlet subcooling. The observed oscillations are found to be density wave oscillations, since the void fraction variations in the chimney inlet and exit are out of phase. They belong to the Type-I category since they occur at low flow qualities.

A linear stability analysis was developed based on the homogeneous equilibrium mixture model. The stability boundaries obtained by the analysis agreed well with those obtained by the experiments. Moreover, the linear stability analysis demonstrates the relation of the oscillation period to the liquid passing time in the chimney.

3.1 Introduction

In simplified BWRs, the flow is driven by natural circulation. A chimney is installed on top of the core to increase the natural circulation flow rate (see Figure 2.1). To achieve reliable cooling performance, natural circulation BWRs have to be designed such that stable flow conditions are guaranteed.

In Chapter 2, we have focused on the suddenly increased vapor generation due to the reduction in hydrostatic head, hereinafter abbreviated as ‘flashing.’ The importance of flashing is indicated by the flashing number. The flashing number is a nondimensional form of saturated

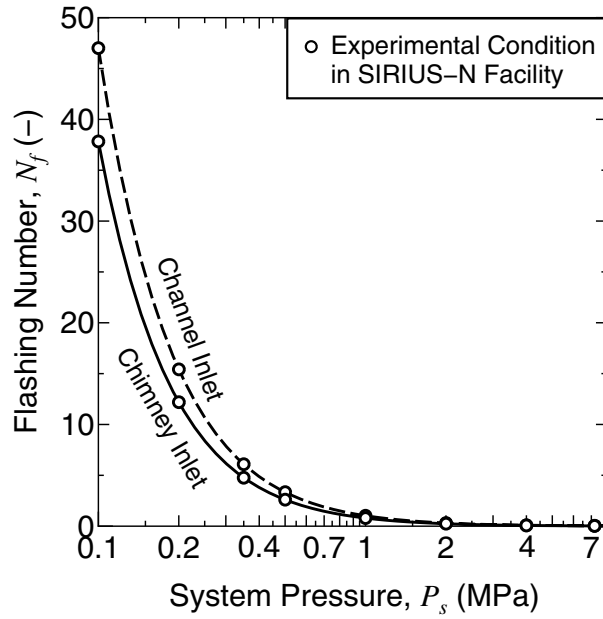


Figure 3.1: Effect of flashing in terms of pressure. The pressure conditions tested in the SIRIUS-N facility are plotted as open circles. Flashing becomes less dominant as pressure increases.

enthalpy difference, which is defined as follows :

$$N_f \equiv \frac{h_{l,in}(P_{in}) - h_l}{h_{gl}} \left(\frac{\rho_l}{\rho_g} - 1 \right). \quad (3.1)$$

Figure 3.1 shows the effect of flashing in terms of the system pressure. The pressure conditions tested in the SIRIUS-N facility are included in the figure (open circle). As shown in the figure, flashing becomes less dominant above roughly 1 MPa.

Since the flashing effect diminishes at relatively high pressure ($P_s > 0.5$ MPa), only few papers address thermal-hydraulic instability of a natural circulation loop at higher pressures. Mathisen (1967) reported that large amplitude oscillations were observed in the natural circulation loop at high pressures ($1 \text{ MPa} \leq P_s \leq 7 \text{ MPa}$), which are induced by the flow dynamics of the natural circulation. Van der Hagen *et al.* (2000) demonstrated Type-I instability at low power and high pressure condition with Dodewaard natural circulation BWR according to Fukuda-Kobori's classification (Fukuda and Kobori, 1979).

This chapter addresses the experimental results at relatively high system pressures ranging from 1 to 7.2 MPa with the SIRIUS-N facility, which exhibits flashing instability at low system pressures ranging from 0.1 to 0.5 MPa described in Chapter 2. In addition, the instability characteristics as well as the conditions where oscillations take place will be addressed. Description of the SIRIUS-N facility and experimental procedure can be found in Chapter 2.

3.2 Instability Characteristics

3.2.1 Representative Signals and Instability Phenomenology

Figure 3.2 shows a set of representative time traces of the signals measured for a system pressure, $P_s = 2$ MPa, a channel heat flux, $q'' = 228 \text{ kW/m}^2$ and a nondimensional channel inlet subcooling, $N_{sub} = 5.46$. Figure 3.2 includes the temperatures, the channel inlet velocity, and the void fractions in the channel (R3 and R4, see Figure 2.2) and chimney region (R5 - R8) tran-

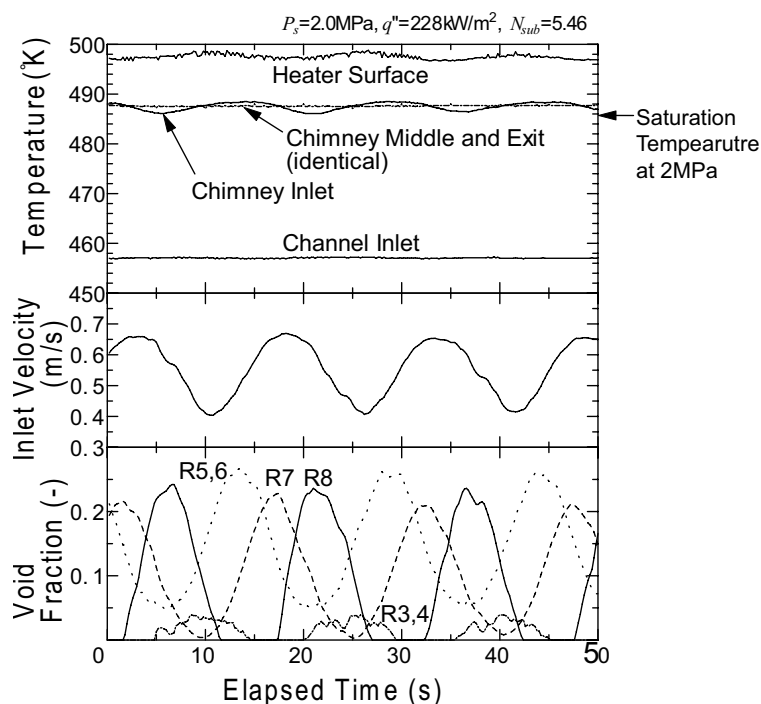


Figure 3.2: Representative time traces of the signals measured when $P_s = 2$ MPa and $q'' = 228$ kW/m², $N_{sub} = 5.46$. The temperatures at the chimney middle and exit agree with saturation temperatures. Boiling occurred at the channel exit, and then bubbles propagated through the chimney toward its exit (R5,6 → R7 → R8). The volume of the propagated bubbles remained constant which contrasts to the bubble growth occurring in the flashing at low pressure as discussed in Section 2.3.1. Out-of-phase oscillations were clearly observed in the void fraction between chimney inlet and exit, which exhibits the characteristics of density wave oscillations.

sients with time from the top to the bottom. Similar time traces of the signals were observed for other system pressures, heat fluxes, and subcoolings.

In contrast to the flashing-induced density wave oscillations at low pressure (see Section 2.3.1), it can be seen from the figure that all the instability signals are sinusoidal. Although the flashing phenomenon may distort the signals from the sinusoidal to intermittent at higher subcooling, the effect of flashing diminishes at elevated pressure (see Figure 3.1).

As shown in Figure 3.2, temperatures at the chimney middle and exit may agree with saturation temperatures at the system pressure of 2 MPa. There are small perturbations observed in the chimney inlet temperature, which coincide with perturbations in the local saturation temperature due to hydrostatic head perturbations.

Figure 3.2 also shows that boiling occurs at the channel exit only, since the non-boiling region was long. It can be seen that the bubbles propagated through the chimney toward its exit (R5,6 → R7 → R8). Moreover, it is clear that the volume of the propagated bubbles remain constant which contrasts to the bubble growth occurring in the flashing at low pressure as discussed in Section 2.3.1. Out-of-phase oscillations were clearly observed in the void fraction between chimney inlet and exit, which exhibits the characteristics of density wave oscillations.

The void fraction in the chimney oscillates in synchronization with the inlet velocity. This is because the driving force of the natural circulation is mainly created by the void generation in the chimney. This issue will be discussed in detail in Section 3.3.4.

The SIRIUS-N facility has two identical parallel channels to investigate so-called channel-to-channel instabilities where the phase of oscillations in one channel is opposite to that in the other. Such oscillations were not observed in these experimental series. The measured values

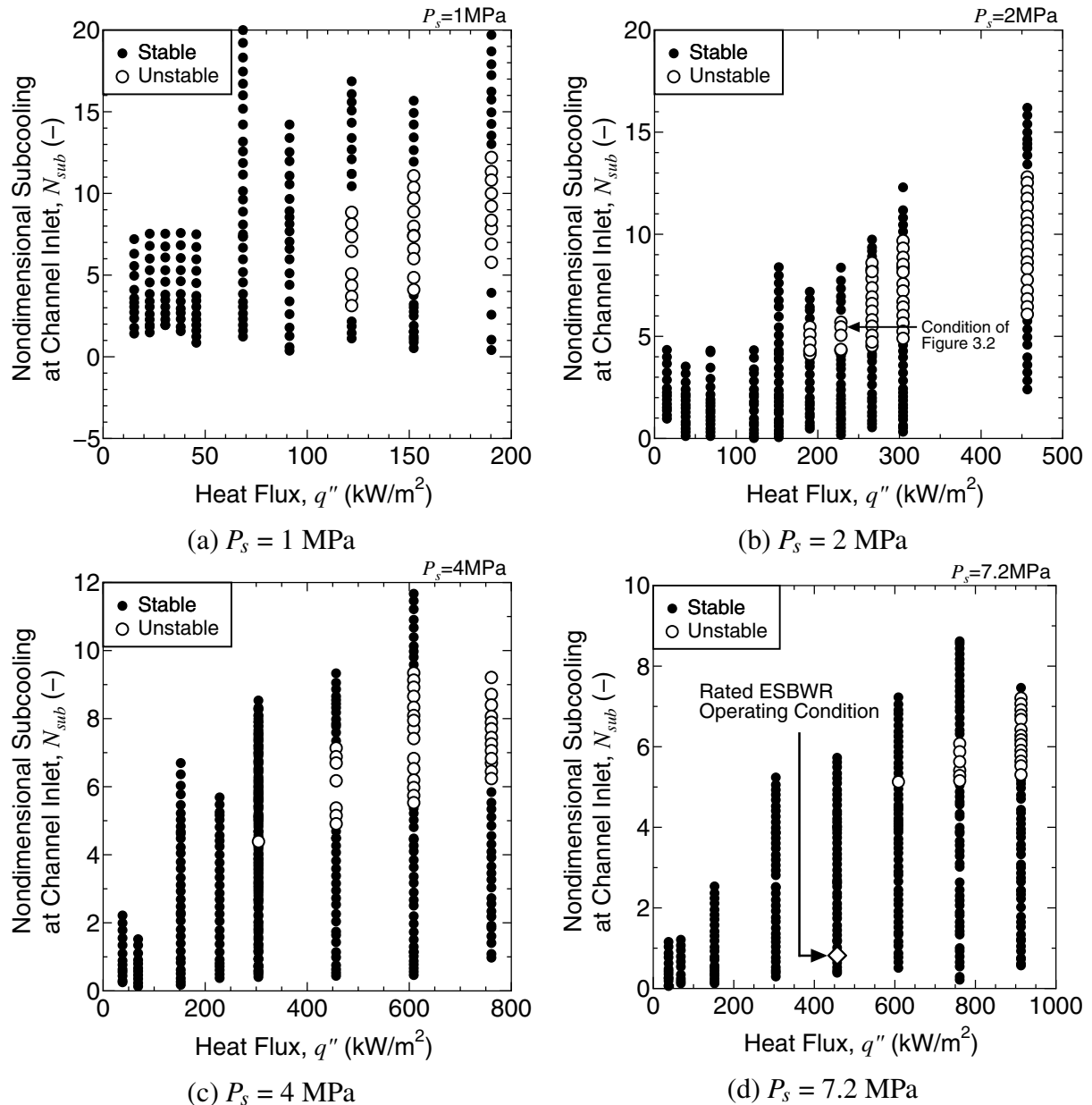


Figure 3.3: Stability maps in reference to heat flux and inlet subcooling. Instability occurs within a certain range of the inlet subcooling. The unstable range is enlarged with increasing heat flux.

of each channel were the same at any moment and location even under oscillatory flow. This is because the primary factor of the instability is governed by void fraction perturbations in the chimney, which affect the driving force of the natural circulation, rather than boiling incipience fluctuations in the channel, as will be discussed later.

In order to investigate the degree of nonlinearity, stability boundaries are compared with increasing and decreasing inlet temperature (approaching from stable to unstable or the other way around). The stability boundaries agree well with each other. Therefore, the degree of nonlinearity is small in the vicinity of the stability boundary.

3.2.2 Effect of System Pressure, Heat Flux, and Inlet Subcooling

The stability maps are plotted in Figure 3.3 with respect to heat flux and nondimensional inlet subcooling for system pressures of 1, 2, 4, and 7.2 MPa. The solid circle '●' means stable condition and open circle '○', means sinusoidal oscillations as shown in Figure 3.2. In this

study, the flow condition is classified “stable” condition when the root mean square (r.m.s.) of the inlet velocity is less than 10 % of the average. This threshold value is often applied in thermal-hydraulic stability researches. The horizontal axis is the heat flux in place of the phase change number to avoid a busy graph (see Figure 3.15). In Section 3.4, we will use the phase change number as a horizontal axis to compare the stability boundary based on the linear stability analysis.

At first, we focus on Figure 3.3 (b), which is the stability map at 2 MPa. The arrow in Figure 3.3 (b) points to the conditions of Figure 3.2. The instability occurs within a certain range of the inlet subcooling. Figure 3.3 (b) shows that the unstable range is enlarged with increasing heat flux. It is interesting to note that no instabilities were observed at 15, 38, 68, 121, and 152kW/m² regardless of the inlet subcooling. In contrast to the experimental results, most linear stability analyses show that there is definitely an unstable region along the zero-quality line toward the origin of heat flux-subcooling (or phase change-subcooling) plane (Van Bragt and Van der Hagen, 1998d; Wang *et al.*, 1994). This is because the nonlinear terms, which are ignored in linear stability analyses, have a damping effect in the region. This (small subcooling and heat flux) region is practically important, since one can startup a reactor from a cold to a high temperature and high power condition without encountering instability. Similar stability trends were observed for other system pressures and heat fluxes as shown in figures 3.3 (a)-(d).

In general, BWRs are designed to operate with a core inlet subcooling ranging from 7K to 18K, so for $N_{sub} = 0.7$ to 1.2. The rated operating condition of the ESBWR (The General Electric new design of a natural circulation BWR) (Cheung *et al.*, 1998) is plotted in Figure 3.3 (d) for comparison. According to the stability map, the reactor can operate at higher inlet subcoolings up to 76K of core inlet subcooling, or 5.1 of N_{sub} without experiencing thermal-hydraulic instability. Additionally, the reactor does not encounter a thermal-hydraulic instability regardless of the heat flux within the experimental range shown in Figure 3.3 (d). Therefore, the ESBWR design has a significant stability margin at the rated operating condition.

Figure 3.4 gives the stability boundaries at system pressures of 1, 2, 4, and 7.2 MPa, obtained from Figure 3.3. Instability was observed within the internal region surrounded by solid lines. It is obvious from this figure that the stable region becomes larger with increasing system pressure. In addition, as the system pressure is increased, the unstable region shifts to higher heat flux. The same tendency was also obtained at low pressures of 0.1, 0.2, 0.35, and 0.5 MPa as shown in Figure 2.5, though the unstable regions are much larger. Comparing the stability maps at high and low pressures, it is clear that the area of stability becomes larger in a cold startup process of a reactor by pressurizing the reactor sufficiently before withdrawing the control rods (heating the reactor core).

In the previous chapter, we defined flashing-induced density wave oscillations. As shown in Figure 3.1, flashing is less dominant at higher pressure. Therefore, one may expect the instability observed at higher pressure to be different from flashing-induced density wave oscillations. The following two sections elaborate on the instability mechanism on the basis of the experimental results at high system pressures in the same manner as we discussed for low system pressures in Sections 2.4 and 2.5. Some parts of Sections 2.4 and 2.5 are intentionally repeated in this section so that one can read this section almost independently.

The types of the instabilities which we should consider in this configuration of the facility are the flow pattern transition instability, geysering, natural circulation oscillations, and density wave oscillations (Yadigaroglu, 1981b; Ozawa, 1999). Acoustic oscillations are excluded because the oscillations are induced by the resonance of pressure waves and the period of oscillations is much smaller than that of the oscillations found in this experiment (ranging from 10 to 18 seconds).

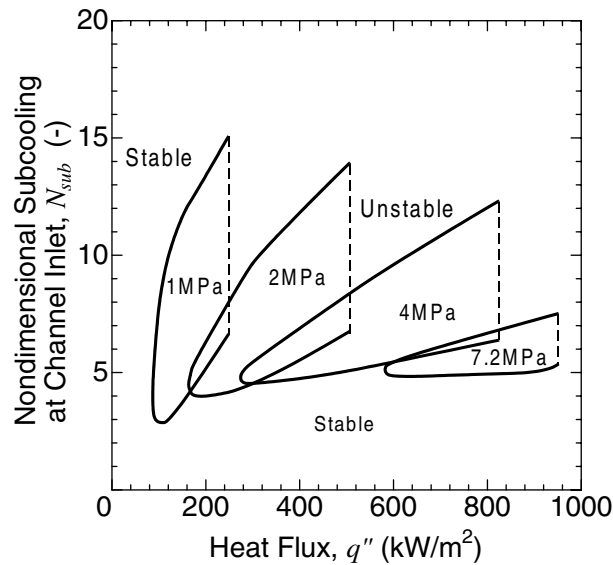


Figure 3.4: Stability maps at $P_s = 1, 2, 4,$ and 7.2 MPa. Instability was observed within the internal region surrounded by solid lines. The stable region enlarges with increasing system pressure. No instabilities were observed below a certain heat flux. This region is of practical important, since one can startup a reactor from a cold to high power and low subcooling condition without encountering instability.

Pressure drop oscillations is the dynamic instability caused by a dynamic interaction between a heated channel and a compressible volume. Pressure perturbations in the separator dome are, however, relatively small ($\leq 0.5\%$ of P_s). Pressure drop oscillations were excluded for this reason. Hereafter, the discussions on possible instability mechanisms is therefore restricted to density-wave oscillations, geysering, flow pattern transition instability, and natural circulation oscillations.

When the boiling system experiences density wave oscillations, the oscillations are due to multiple regenerative feedbacks between the flow rate, vapor generation rate and pressure drop. It is reported that the period is approximately one and a half to two times the time required for a fluid to travel through the two-phase region (Ozawa, 1999).

Figure 3.5 illustrates the relationship between the flow oscillation period, τ_{fo} , and the time required for bubbles to pass through the chimney region, $\tau_{pr,g}$. $\tau_{pr,g}$ is equal to the volume of the chimney, V_r , divided by the average volumetric flow rate of the gas phase, $\langle Q_{g,r} \rangle$. $\langle Q_{g,r} \rangle$ is determined by the drift flux model using the experimentally-obtained inlet velocity and void fractions. The volume accounts only for the chimney region, since the flow oscillation period is normally compared to two-phase flow region and the void fractions in channel regions are small.

All unstable data (148 points) correlate well in the single clusters regardless of the system pressure, heat flux, and inlet subcooling. The oscillation period was 1.1 to 1.8 times the time required for bubbles to travel through the chimney region. In addition, the void fraction fluctuations in the inlet and exit of the chimney were out of phase (shifted by approximately 180 degrees) as shown in Figure 3.2. These two facts are practical characteristics of density wave oscillations due to the time delay of bubbles that are generated in the channels to travel through the chimney to create the driving force of the natural circulation. According to the Fukuda-Kobori's classification (Fukuda and Kobori, 1979), the observed oscillation is so-called Type-I density wave oscillations, since it occurred at low quality condition.

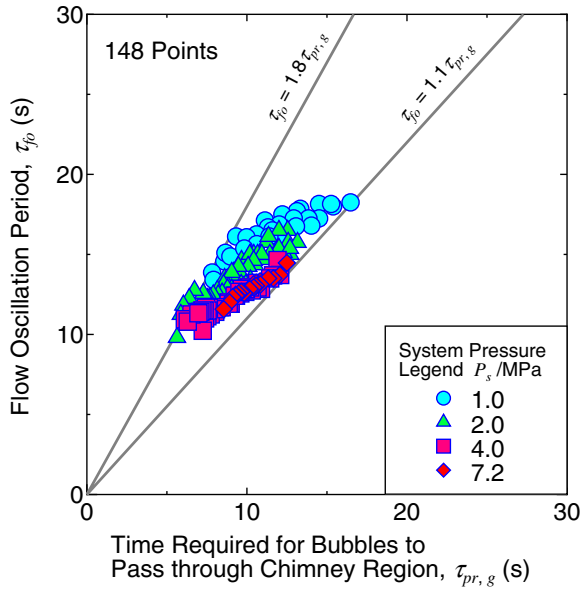


Figure 3.5: All unstable data correlate well in the single clusters regardless of the system pressure, heat flux, and inlet sub-cooling. The oscillation period was 1.1 to 1.8 times the time required for bubbles to travel through the chimney region, exhibiting practical characteristics of density wave oscillations.

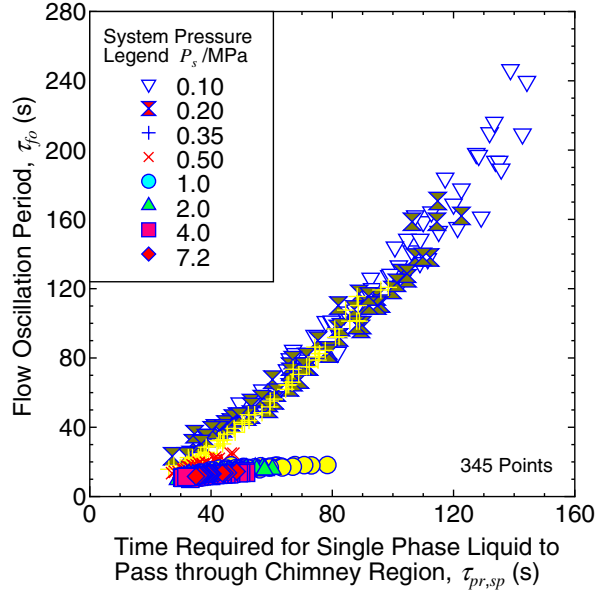


Figure 3.6: Two distinct branches are found in the relation between the oscillation period and liquid passing time in the chimney. This indicates that the driving mechanisms of the instabilities are different for low and high pressures. The demarcation lies somewhere in between 0.5 MPa and 1.0 MPa.

3.3 Comparison with Other Kinds of Instabilities

3.3.1 Flashing-induced Density Wave Oscillations

In contrast to Type-I density wave oscillations at high pressure, the oscillation period correlates well with single-phase liquid travel time for flashing induced density wave oscillations at low pressure as shown in Figure 3.6. The horizontal axis denotes the time required for single-phase liquid to pass through the chimney region, $\tau_{pr,l}$, which is equal to the volume, V_r , divided by the average volumetric flow rate of the liquid, $\langle Q_{l,r} \rangle$. The obtained high pressure data are also plotted in the same figure. Two distinct branches in Figure 3.6 clearly indicate that the driving mechanisms of the instabilities are different for low and high pressures. It can be seen in the figure that some plots of 0.5 MPa are laid in between the two branches, which implies the transition region of the two mechanisms. Therefore, the demarcation lies somewhere in between 0.5 MPa and 1.0 MPa.

The difference of the two mechanisms at high and low pressures can be explained by the role of flashing. As shown previously in Figure 3.1, flashing becomes less dominant above roughly 1 MPa at which the two mechanism are divided. At high pressures, the oscillation period correlates well with the bubble passing time in the chimney, since the instability is caused by a delay of the bubbles created in the channels flowing into the chimney to dominate natural circulation flow. On the other hand, the oscillation period at low pressures correlates well with the single-phase liquid passing time in the chimney, since the instability is caused by a delay of single phase liquid flowing into the chimney to dominate natural circulation flow by flashing.

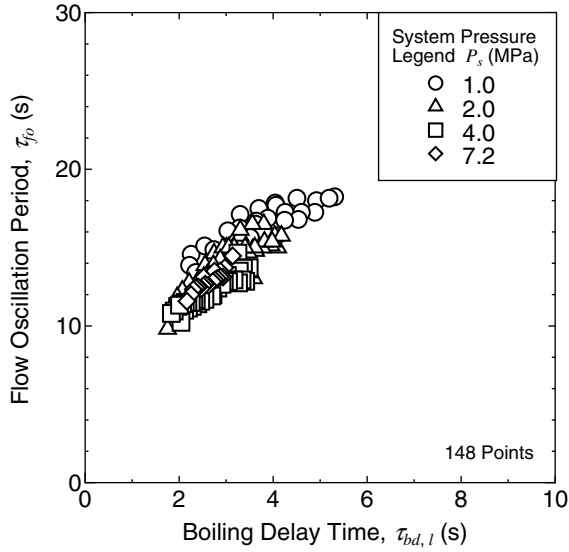


Figure 3.7: The oscillation period is several times larger than the boiling delay time. This indicates the flow oscillations are not caused by geysering.

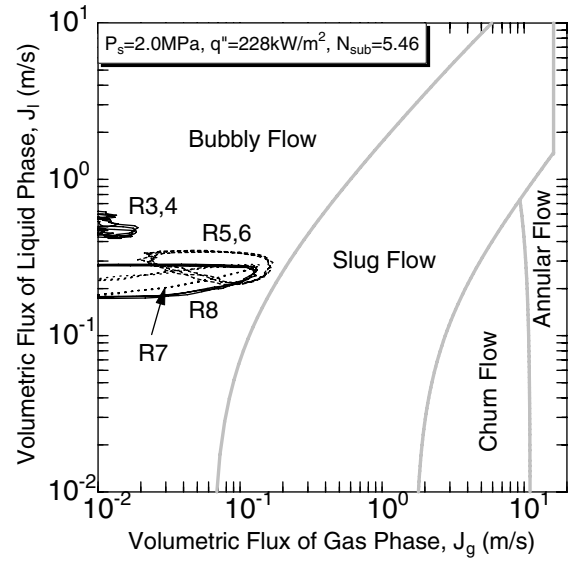


Figure 3.8: Transient flow patterns are plotted for three cycles. The flow pattern at regions R3 - R8 is found to be bubbly flow. The flow pattern is checked for all conditions in this experiment and found not to fall in or change to churn or annular flow with its characteristically lower pressure drop initiating flow pattern transition instability.

3.3.2 Geysering

Geysering has been observed in a variety of closed end (or forced flow at small flow rate) vertical columns of liquid which are heated at the base. Geysering consists of three consecutive processes, viz. boiling delay, condensation (or expulsion of vapor), and liquid returning (Nakanishi *et al.*, 1978). It is also reported that the period of flow oscillation, τ_{fo} , is nearly equal to the boiling delay time, τ_{bd} , because the boiling delay time is much longer than that of the other two processes in most cases.

Since geysering has not yet been defined clearly for natural circulation flow in relation with density wave oscillations, we treat the characteristics of geysering in the natural circulation system in a similar way as those in a closed end or forced circulation system. The boiling delay time is defined as the time required for the fluid having some degree of subcooling, $\Delta T_{sub,in}$ to be heated up to the saturation temperature based on the pressure at the channel inlet and is expressed by the following equation.

$$\tau_{bd} = \frac{\rho_{l,in} C_{pl,in} \Delta T_{sub,in} A_c l_c}{q''} \quad (3.2)$$

A_c and l_c represent the flow area and length of the heated section, respectively. The properties of the density, $\rho_{l,in}$, and the specific heat capacity at the constant pressure, $C_{pl,in}$ are based on the temperature at the channel inlet. The relationship between the boiling delay time and the flow oscillation period is depicted in Figure 3.7. The oscillation period is several times larger than the boiling delay time, and increases with increasing boiling delay time. Therefore, this flow oscillation caused by Type-I density wave oscillations is not geysering as defined above. The reasons are (1) the flow rate is large enough to prevent the formation of a water super-heated

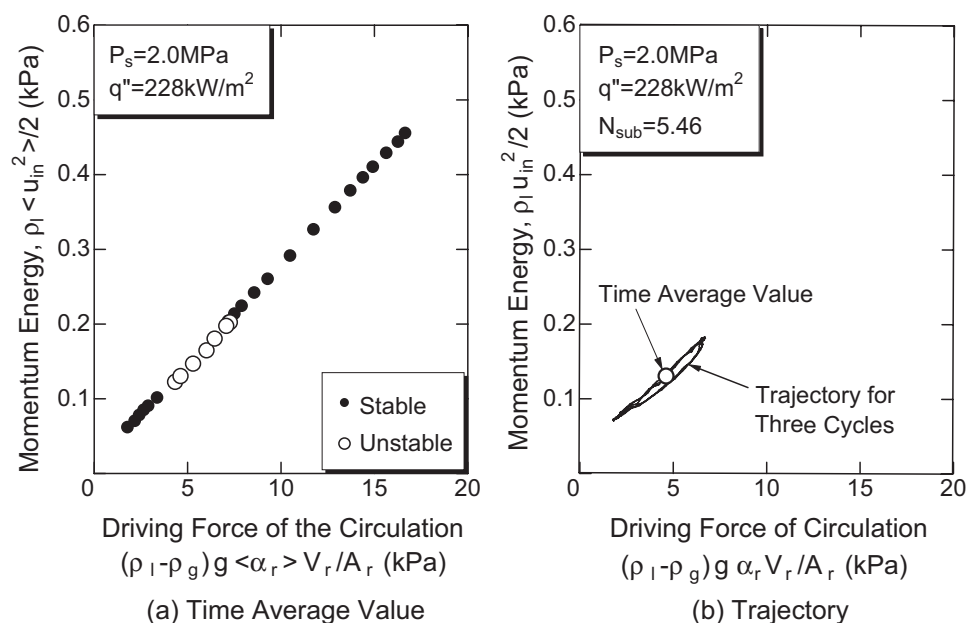


Figure 3.9: Momentum response of natural circulation driving force. Figure (a) shows that the average values are on a straight line that passes through the origin. The static characteristics are therefore well correlated whether the flow condition is stable or unstable. Figure (b) shows the oscillatory behavior that moves on the straight line of static characteristics. Therefore, the oscillations are not caused by natural circulation oscillations, where the trajectory would be ellipsoidal.

layer from forming and (2) there is not enough subcooled water to condense large bubbles as shown in Figure 3.2.

3.3.3 Flow Pattern Transition Instability

Flow pattern transition instabilities have been postulated to occur when the flow conditions are close to the point of transition between bubbly flow and annular flow with its characteristically lower pressure drop initiating flow pattern transition instability. Nayak *et al.* (2003) performed numerical analysis, thereby taking account of the flow pattern transition criteria for a natural circulation heavy water moderated boiling light water cooled reactor. They found that an increasing pressure and a decreasing inlet subcooling have a stabilizing effect on the flow pattern transition instability. Although our facility is as high as a prototypical natural circulation BWR, the chimney diameter of the facility is relatively small to simulate high quality flow pattern such as churn and annular flow. In this section, the transient flow pattern is compared with the flow pattern transition instability.

Figure 3.8 shows a transient flow pattern in reference to Mishima-Ishii's diagram (Mishima and Ishii, 1984). Experimental data are plotted for about three cycles of oscillations at regions R3 - R8, when $P_s = 2$ MPa and $q'' = 228$ kW/m², $N_{sub} = 5.46$. Flow pattern at regions R3 - R8 are found to be bubbly flow as shown in the figure.

The flow pattern was checked for all conditions in this experiment and was found not to fall within or change to churn or annular flow when the instability occurred. Therefore, it can be concluded that the observed instability is not caused by the flow transition instability.

3.3.4 Natural Circulation Oscillation

Chiang *et al.* (1993a) observed a flow oscillation induced by an accumulation of bubbles in a specific part of the two-phase flow loop. They called this phenomenon natural circulation oscillation, and explained the successive process as follows:

- (a) Vapor accumulates in a non-heated pipe (connecting the outlet plenum to the separator tank, which consists of vertical and horizontal pipes in their apparatus), when the evaporation rate is insufficient.
- (b) Bubbles coalesce with incoming vapor bubbles, and then the hydrostatic head decreases gradually.
- (c) Accumulated vapor flushed out as a result of increasing flow rate, and water, in turn, filled in.
- (d) The hydrostatic head increases and therefore the circulation rate decrease (resulting in a return to process (a)) and then the process repeats itself.

This phenomenon repeats periodically, as momentum energy is shifted quasi-statically by about 180 degree against the driving force of the circulation.

Bubbles may not accumulate in a natural circulation BWR and the SIRIUS-N facility. We propose a method to investigate the amount of bubble accumulation as postulated in the mechanism of the natural circulation oscillation. Figure 3.9 illustrates a response of momentum energy to natural circulation driving force at $P_s = 2$ MPa and $q'' = 228$ kW/m², $N_{sub} = 5.46$. The natural circulation is induced by a decrease in apparent density as a result of vapor generation. Therefore driving force can be expressed as $(\rho_l - \rho_g)g\alpha_r V_r / A_r$. The subscript r denotes a value defined at the chimney. The momentum energy is expressed as $\rho_l u_{in}^2 / 2$.

The average values are plotted in Figure 3.9(a). All values are on a straight line that passes through the origin so the static characteristics are well correlated both under stable and unstable conditions. The trajectory is shown in Figure 3.9(b) for the conditions of representative intermittent and sinusoidal oscillations as shown in Figures 3.2(b) and (c). The trajectory moves on the straight line of static characteristics as illustrated in Figure 3.9(a). It is clear that vapor did not accumulate in the two phase section so that the response of the momentum energy to the natural circulation driving force was fast. The type of instability in this experiment is governed by Type-I density wave oscillations rather than natural circulation oscillations in which the trajectory would be ellipsoidal.

3.4 Modeling of Boiling Two-Phase Flow Dynamics for Stability Estimation

In order to understand physics behind the boiling two phase flow in a natural circulation BWR, a linear stability analysis describing the boiling two phase flow is conducted. In the following sections, after a brief introduction of the analytical modeling, a reduced model is described to validate the experimentally-obtained stability boundary with the SIRIUS-N facility. Moreover, the model will be modified to investigate the effect of single-phase natural circulation on the stability.

3.4.1 Historical Perspective of Analytical Modeling

In the 1950's, DeShong and Lipinski (1958) and Thie (1958) developed a simple point-kinetic model to examine the reactivity-to-power transfer function and the root loci of the BWR dynamics. March-Leuba *et al.* (1986a) and March-Leuba *et al.* (1986b) derived a simplified, phenomenological model to study linear and nonlinear dynamical behavior of BWRs. They found that at least three zeros and four poles are required to properly describe the reactivity-to-power transfer function of a BWR. They used, however, a strongly simplified description for the thermal-hydraulics: a second-order model that is not able to predict two-phase flow instabilities.

Lahey and Moody (1993), Yadigaroglu (1981a) and Miida and Suda (1963) used more sophisticated thermal-hydraulic models to couple with the neutronics on the basis of the intensive experimental research on the boiling two-phase flow systems, which are carried out in the 1960's and 1970's. In the last two decades, more elaborated, but reasonably simple, models are applied for the stability analysis of natural circulation two-phase flow systems (Rao *et al.*, 1995; Karve *et al.*, 1997; Clausse and Lahey, 1991; Lee and Lee, 1991; Wang *et al.*, 1994; Pinheiro Rosa and Podowski, 1994; Garea *et al.*, 1994; Chang and Lahey, 1997).

This and the following sections are devoted to the linear stability analysis of natural-circulation BWRs and the underlying (two-phase) thermal-hydraulic system via the root-locus method. The reduced-order model of Van Bragt and Van der Hagen (1998c) is used, which is sufficient to predict most thermal-hydraulic instability phenomena in natural circulation BWRs. Because of its simplicity, it has the potential to increase the insight into the relation between the main physical processes determining BWR stability.

3.4.2 Reduced-Order Model

Figure 3.10 gives an schematic overview of the flow path in a natural-circulation BWR loop showing all the components that are accounted for in the reduced-order model of Van Bragt and Van der Hagen (1998c). Although the steam dome above the chimney is not modeled explicitly (compare with Figure 1.2), a constant water level in the system is assured by adjusting the feedwater flow to the steady-state steam flow. The system components outside of the reactor vessel are not modeled. Therefore, the steam line pressure and feedwater temperature are imposed as boundary conditions. Local pressure losses are modeled using friction factors at the core inlet, core exit, chimney exit and downcomer inlet. Distributed pressure losses (tube friction) are modeled in the core and in the chimney.

The most important assumptions and approximations applied in the reduced-order model can be summarized as follows:

1. The neutron kinetics is modeled by the point-kinetic equations with one effective delayed neutron group.
2. The heat transfer from fuel to coolant is modeled as a first-order process using one effective time constant.
3. The two-phase flow in the multiple parallel coolant channels of a BWR is analyzed on the basis of the one-dimensional homogeneous-equilibrium-mixture (HEM) model using one effective (average) coolant channel.
4. The core section is divided into a single-phase and a two-phase axial node. The differential balance equations are integrated over each node by assuming a time-dependent and spatially linear profile of a one-phase enthalpy and the two-phase flow quality in the axial direction.

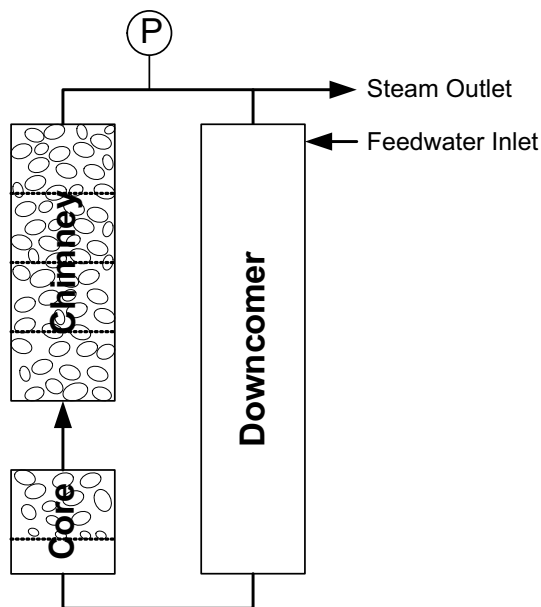


Figure 3.10: Reduced-order model diagram. The natural circulation flow loop through the downcomer, core chimney is modeled. The arrows indicate flow directions.

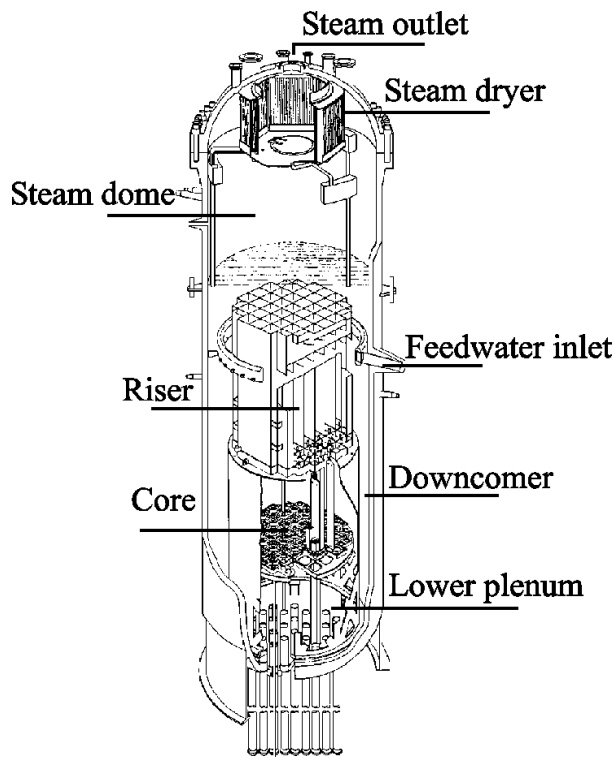


Figure 3.11: A cut-away scheme of Dodewaard natural-circulation BWR. No recirculation pumps are present in this design. A relatively long chimney is placed on the top of the core to increase the natural-circulation flow rate.

5. Subcooled boiling and void flashing phenomena are ignored.
6. To analyze a system with a chimney, the chimney is divided into several axial nodes, and the aforementioned linear spatial approximation is used for the flow quality and mass flux within each node.
7. The downcomer is assumed to be filled only with a liquid. Therefore, carry under (intrusion of vapor bubbles into a liquid downstream) is neglected. The liquid is assumed to be incompressible with a fluid temperature uniform in space and time.

The governing differential balance equations for the thermal-hydraulics are transformed into ordinary differential equations (ODEs) using the above assumptions. A comprehensive list of the model equations is given in Appendix A.

Van Bragt *et al.* (1999) have shown that using four axial nodes in the chimney represents a reasonably good approximation for the case of the Dodewaard natural-circulation reactor as illustrated in Figure 3.11. The data set and geometry of this reactor, dividing the chimney into four axial nodes, is used as a model reactor in this study.

By using four nodes in the chimney the model consists of ten nonlinear ODEs which are linearized and Laplace-transformed to facilitate a frequency-domain analysis. The underlying relations between the system variables can be represented in the block diagram shown in Figure 3.12. For the thermal-hydraulic subsystem, shown within the dashed rectangle, $G_{x,y}$ denotes the normalized transfer function from variable y to x . The explicit expressions of the transfer functions are listed in Appendix A. The transfer functions in the block diagram are all functions

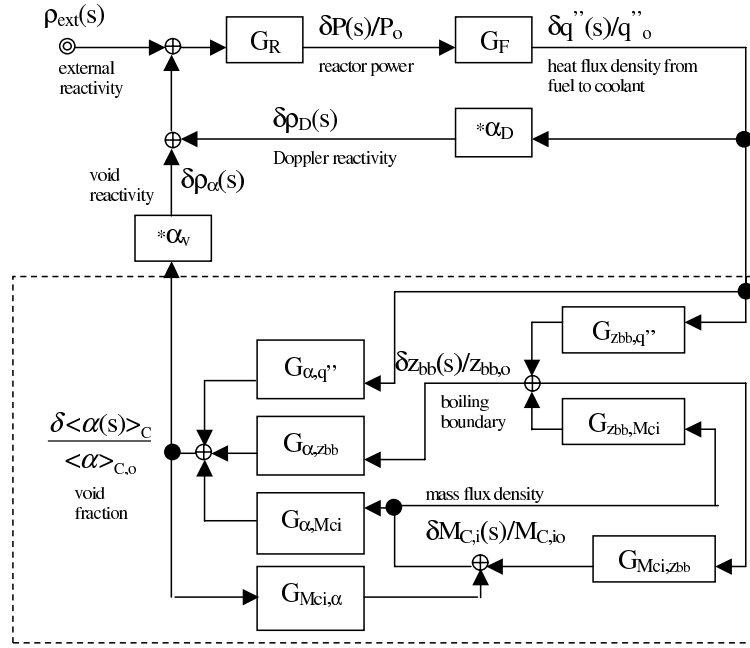


Figure 3.12: Block diagram representing the closed-loop, 'external reactivity' to 'reactor power', transfer function of a BWR for the linearized, frequency-domain model (Van Bragt and Van der Hagen, 1998a). The thermal-hydraulic transfer functions are clustered in the dashed rectangle. The Doppler and void reactivity is obtained by multiplying the fuel-temperature and void-fraction oscillations with the corresponding reactivity coefficients, C_D and C_α .

of the Laplace variable $s = \sigma + i\omega$, where σ is the real part and ω is the imaginary part. The model represents the inherent feedback mechanisms in a BWR (void- and Doppler-reactivity feedback), as depicted in Figure 3.12. The transfer function of the thermal-hydraulic subsystem from heat flux to core-average void fraction is given by

$$G_A \equiv \frac{\frac{\delta \langle \alpha(s) \rangle_C}{\langle \alpha \rangle_{C,o}}}{\frac{\delta q''(s)}{q''_o}} = \frac{G_1}{1 + G_{M_{C,i},\alpha} G_1 + G_{M_{C,i},z_{bb}} G_{z_{bb},q''}}, \quad (3.3)$$

where

$$G_1 = G_{\alpha,q''} + G_{\alpha,z_{bb}} G_{z_{bb},q''}.$$

The closed-loop reactor transfer function from external reactivity to reactor power is then

$$G_T = \frac{\frac{\delta P}{P_o}}{\rho_{ext}} = \frac{G_R}{1 - G_R G_F [C_\alpha + C_D G_A]}. \quad (3.4)$$

The poles of the closed-loop transfer function are obtained by considering the roots of the characteristic equation:

$$1 - G_R G_F [C_D + C_\alpha G_A] = 0. \quad (3.5)$$

The closed-loop transfer function of a higher-order system, as with a BWR, has several poles, which are real and/or form complex conjugate pole pairs. The dynamic stability of a pole is usually quantified by its decay ratio (DR), which is defined as $DR = \exp 2\pi\sigma/|\omega|$ for a pole at $s = \sigma + i\omega$. The least stable pole, with the largest $\sigma/|\omega|$ ratio, determines the stability of the system. The poles of the system at a specific operating point are determined by a numerical search algorithm, a quasi-Newton method.

To make the analysis more transparent, the thermal-hydraulic subsystem is examined separately. The characteristic equation of the thermal-hydraulic subsystem, using equation (3.3), is

$$1 + G_{M_{C,i},\alpha}(G_{\alpha,q''} + G_{\alpha,z_{bb}}G_{z_{bb},q''}) + G_{M_{C,i},z_{bb}}G_{z_{bb},q''} = 0. \quad (3.6)$$

Considering that

$$G_{M_{C,i},\alpha} = -\frac{\frac{\delta\Delta P_{total}}{\delta\langle\alpha\rangle_C} \langle\alpha\rangle_{C,o}}{\frac{\partial\Delta P_{total}}{\partial M_{C,i}} M_{C,i,o}}, G_{M_{C,i},z_{bb}} = -\frac{\frac{\delta\Delta P_{total}}{\delta z_{bb}} z_{bb,o}}{\frac{\delta\Delta P_{total}}{\partial M_{C,i}} M_{C,i,o}} \quad (3.7)$$

and

$$G_{z_{bb},M_{C,i}} = -G_{z_{bb},q''}, G_{\alpha,q''} = -G_{\alpha,M_{C,i}} \quad (3.8)$$

The characteristic equation of the thermal-hydraulic subsystem can be written in a form that is frequently used in literature (Yadigaroglu, 1981a; Rao *et al.*, 1995)

$$\frac{\delta\Delta P_{total}}{\delta M_{C,i}}(s) = 0, \quad (3.9)$$

where $\frac{\delta\Delta P_{total}}{\delta M_{C,i}}(s)$ is the total transfer function from the inlet mass flux to the total pressure drop over the circulation loop. The left-hand side of this characteristic equation (the characteristic polynomial) can be split into a sum of transfer functions from inlet mass flux to the different types of physical pressure drops:

$$\frac{\delta\Delta P_{total}}{\delta M_{C,i}}(s) = \sum_{j=1-\phi, 2-\phi} \left[\frac{\delta\Delta P_{in}}{\delta M_{C,i}}(s)_j + \frac{\delta\Delta P_{fr}}{\delta M_{C,i}}(s)_j + \frac{\delta\Delta P_{gr}}{\delta M_{C,i}}(s)_j + \frac{\delta\Delta P_{acc}}{\delta M_{C,i}}(s)_j \right] = 0. \quad (3.10)$$

The following physical pressure drop terms are distinguished in both the one- and the two-phase region: inertial, frictional, gravitational, and accelerational pressure drop. We will refer to the foregoing transfer functions from inlet mass flux to the different types of pressure drop shortly as pressure drop transfer functions throughout the text. By fixing all the system parameters except one, the threshold of *dynamic* instability for that parameter and the corresponding oscillation frequency can be obtained numerically from equation (3.10) if one sets $s = i\omega$ (the latter corresponds to $DR = 1$). Incrementally varying another system parameter an entire stability map can be drawn in a two-dimensional parameter space. Equation (3.10) also provides the threshold of the *static* instability as the $\omega \rightarrow 0$ limit is taken (Lahey and Yadigaroglu, 1982). We note here that if a system without chimney is modeled, then all the transfer functions in the characteristic equation, equation (3.6), are (ratios of) second- or first-order polynomials in s in such a combination that the left-hand side of the equation is equivalent to a third-degree polynomial (third-order system). If a system with four chimney nodes is modeled, then the order of the system increases to seven. Obviously, the same holds for equation (3.9).

3.4.3 Verification of Static Characteristics with Experimental Data

In order to obtain a reliable stability boundary, static characteristics (stationary part of parameters) of the analysis must be validated with the experimental data. The natural circulation flow rate is the most significant variable in the boiling natural circulation loop.

Figure 3.13 shows a comparison of the velocities at the channel inlet between the analytical and the experimental results for different inlet subcoolings. Experimental results were obtained for the system pressure 2.0 MPa and the heat flux 228 kW/m² with the SIRIUS-F facility. The experimental results show that the inlet velocity increases with decreasing inlet subcooling. It can be seen that the experimental results agree well with analytical results, indicating the validity of the analysis.

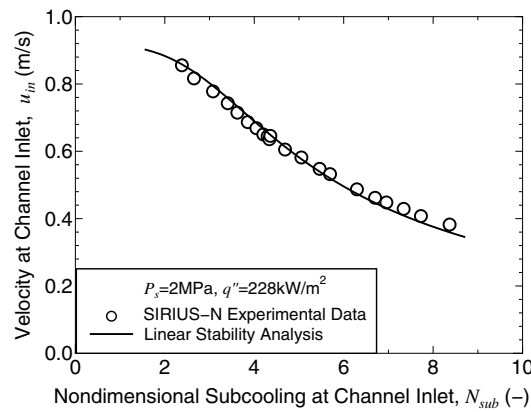


Figure 3.13: Validation of the reduced-order model at stationary conditions. The analytically-obtained velocity at the channel inlet was compared with the experimental results for different inlet subcoolings at 2 MPa and 228 kW/m². The analytical results agree well with experimental results.

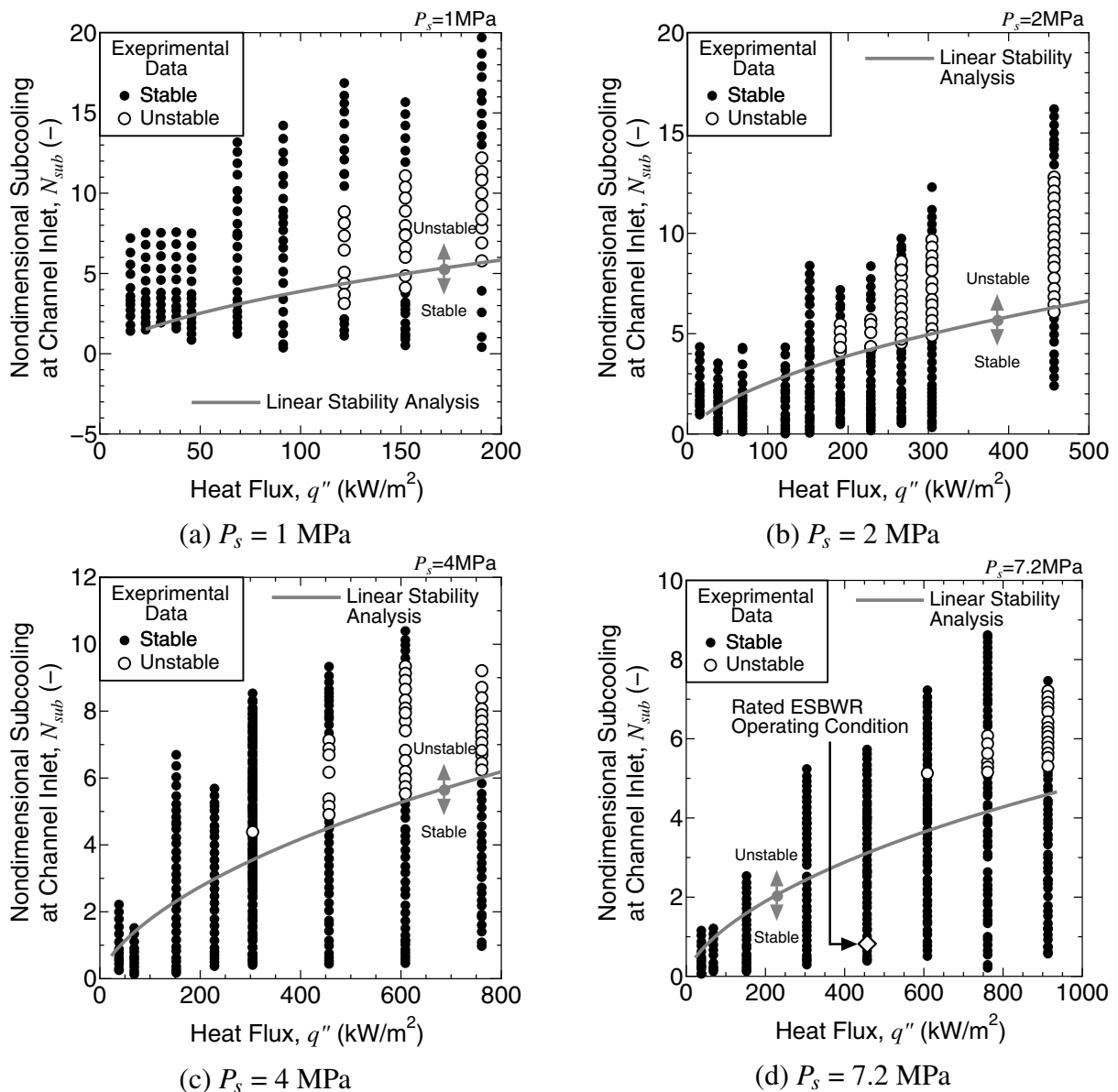


Figure 3.14: Analytically obtained stability boundary at low subcooling is overlaid with the experimentally-obtained stability map. The linear stability predicts the stability boundary at the lower subcooling well

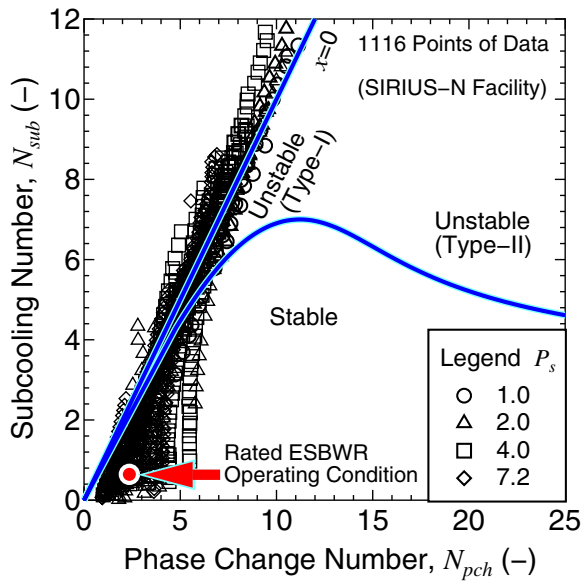


Figure 3.15: All experimental data are plotted to identify experimental range for high pressures. The curve indicates analytical stability boundary. The rated operating condition of the ESBWR is more susceptible to Type-I instability than Type-II instability.

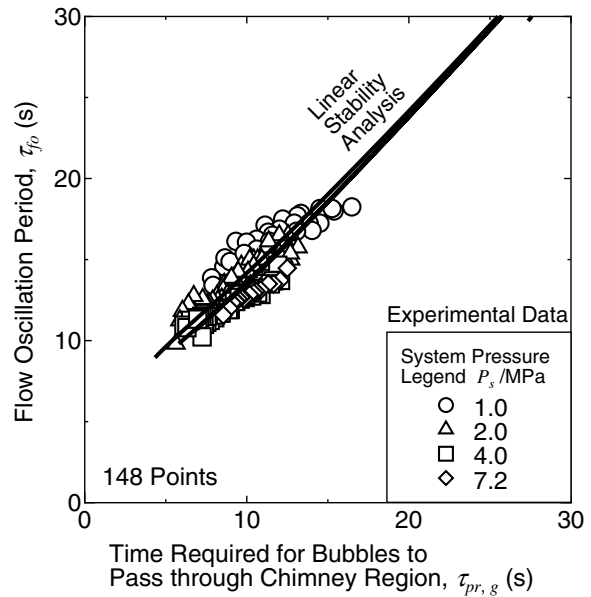


Figure 3.16: The four curves indicate analytical results for different system pressures, though differences among these curves are small. The linear stability analysis clearly demonstrates the relationship of the bubble passing time and the flow oscillation period.

3.4.4 Analytical Prediction of the Lower Subcooling Stability Boundary

In order to demonstrate the validity of the reduced-order model, a linear stability analysis was carried out for high system pressures (1.0 - 7.2 MPa). The analytical inlet subcooling at the stability boundary was obtained as a function of the heat flux. Figure 3.14 shows the analytical stability boundary together with the experimentally-obtained stability maps in terms of the inlet subcooling and the heat flux for different pressures. It can be seen that the flow condition is stable below the curve in the figure estimated by the linear stability analysis. As mentioned before, Type-I instability occurred within a certain range of the inlet subcooling. The analytical stability boundary for the lower subcooling agrees well with the experimentally-obtained stability boundary.

3.4.5 Instability Characterization by Linear Stability Analysis

Fukuda and Kobori (1979) proposed the Type-I instability (only occurring with a chimney installed) and the Type-II instability. The Type-I instability is dominant when the flow quality is low, while the Type-II instability is dominant when the flow quality is high. The Type-II instability is the most commonly observed form of density wave oscillation. In order to discriminate Type-I and Type-II instabilities, stability maps are often plotted in the subcooling - phase change numbers. The phase change number is a nondimensional form of the heat flux divided by the flow rate. In Section 3.2.2, stability maps were shown in terms of two independent experimental parameters (the subcooling and the heat flux) to avoid a busy stability map. Experimental data are replotted in the subcooling - phase change numbers to identify the instability mode.

Figure 3.15 shows the stability map in terms of subcooling and phase change numbers. All

experimental data (1116 points) are plotted whether the flow condition is stable or unstable to identify experimental range for high pressures. Moreover, the rated operating condition of the ESBWR is plotted in the figure. It is clearly seen from the figure that the rated operating condition of the ESBWR is more susceptible to Type-I instability than Type-II instability. It is also found, however, that the rated operating condition of the ESBWR has significant stability margin (approximately 64 K of inlet subcooling) to the unstable region according to the obtained stability map.

As we discussed in Section 3.2.2, the flow oscillation period is well correlated with the time required for bubbles to travel through the chimney region regardless of the system pressure, the heat flux, and the inlet subcooling for the system pressure ranging from 1 MPa to 7.2 MPa. It is of interest to examine this correlation with a linear stability analysis. The flow oscillation period, τ_{fo} , is obtained as a reciprocal of the frequency, f :

$$\tau_{fo} = \frac{1}{f}. \quad (3.11)$$

The time required for bubbles to pass through the chimney region, $\tau_{pr,g}$, is expressed as:

$$\tau_{pr,g} = \frac{\rho_l l_r}{M_{R,i}}. \quad (3.12)$$

Figure 3.16 shows the flow oscillation period in terms of the time required for bubbles to pass through chimney region. Although the four curves indicate analytical results for different system pressures (1.0 - 7.2 MPa), the differences among these curves are small. All unstable data obtained with the SIRIUS-N facility (open symbols in the figure) are plotted along the curves. It can be concluded from this figure that the linear stability analysis clearly demonstrates the relationship of the bubble passing time and the flow oscillation period, which is characteristic for the Type-I instability.

3.4.6 Effect of Single-Phase Liquid Natural-Circulation

Several analytical models have been successfully used in the past to predict flow oscillations in boiling channels and BWRs. Because the mathematical form of the conservation equations governing two-phase flow dynamics is nonlinear, simplifying assumptions are made to analyze two-phase flow instability. In nearly all of them, however, the dependence of the liquid density on the fluid temperature is neglected. Since this simplified approach might give non-conservative results, it is important to investigate the effects of liquid density differences on two-phase flow stability.

As an example, Figure 3.17 shows a typical stability map in the dimensionless plane of the phase change number and the subcooling number, obtained for a natural circulation system consisting of a heated core, adiabatic chimney and downcomer, where the liquid density differences are being neglected. The straight line in the figure indicates the operational points where the flow quality at the core exit is zero. Points A and B are selected for representative Type-I and Type-II instability boundary conditions in this analysis.

This section is focused on the effect of liquid density differences on thermal-hydraulic stability. The model, which is described in the previous section, is now extended to take into account the dependence of the liquid density on the fluid temperature. Physical insight is obtained by investigating Type-I and Type-II instability as represented by operational points A and B in Figure 3.17.

Table 3.1: Dynamic Pressure Drops in the Natural Circulation Loop

Location	Description
1. Inertia	
Core	$Z_{bb}(t) \frac{dM_{C,i}(t)}{dt} + (L_C - Z_{bb}(t)) \frac{dM_{C,e}(t)}{dt} + (M_{C,i}(t) - M_{C,e}(t)) \frac{dZ_{bb}(t)}{dt}$
Chimney	$\sum_{n=1}^{N_R} \frac{L_R}{N_R} \frac{d\langle M(t) \rangle_{R,n}}{dt}$
Downcomer	$\left[\sum_n^{N_D} \frac{L_{D,n}}{A_{D,n}} \right] A_{C,i} \frac{dM_{C,i}(t)}{dt}$
2. Acceleration	
Core	$\frac{M_{C,e}^2(t)}{\rho_{l,sat}} \phi^2 x_{C,e} - \frac{M_{C,i}^2(t)}{\rho_{l,sub}}$
Chimney	$\frac{M_{R,e}^2(t)}{\rho_{l,sat}} \phi^2 x_{R,e}(t) - \frac{M_{R,i}^2(t)}{\rho_{l,sat}} \phi^2 x_{R,i}(t)$
Downcomer	$\frac{M_{C,i}^2(t) A_C^2}{2\rho_{l,sub}} \left[\frac{1}{A_{D,e}^2} - \frac{1}{A_{D,i}^2} \right]$
3. Gravity	
Core	$\frac{\rho_{l,sat} + \rho_{l,sub}}{2} g Z_{bb}(t) + \left[\rho_{l,sat} \left(1 - \langle \alpha(t) \rangle_{C,br} \right) + \rho_g \langle \alpha(t) \rangle_{C,br} \right] g (L_C - Z_{bb}(t))$
Chimney	$\sum_{n=1}^{N_R} \left[\rho_{l,sat} \left(1 - \langle \alpha(t) \rangle_{R,n} \right) + \rho_g \langle \alpha(t) \rangle_{R,n} \right] g \frac{L_R}{N_R}$
Downcomer	$-\rho_{l,sub} g (L_C + L_R)$
4. Wall Friction	
Core	$\frac{f_C}{D_C} \frac{M_{C,i}^2(t)}{\rho_{l,sat} + \rho_{l,sub}} Z_{bb}(t) + \frac{f_C}{2D_C} \frac{M_{C,e}^2(t)}{\rho_{l,sat}} \phi^2 \langle x(t) \rangle_{C,br} (L_C - Z_{bb}(t))$
Chimney	$\sum_{n=1}^{N_R} \frac{f_R}{2D_R} \frac{M_{R,i}^2(t)}{\rho_{l,sat}} \phi^2 \langle x(t) \rangle_{R,n} \frac{L_R}{N_R}$
Downcomer	$\sum_n^{N_D} \frac{f_D}{2D_{D,n}} \frac{M_{C,i}^2(t)}{\rho_{l,sub}} \frac{A_C^2}{A_{D,n}^2} L_{D,n}$
5. Local Pressure Drop	
Inlet Core	$\kappa_{C,i} \frac{M_{C,i}^2(t)}{\rho_{l,sub}}$
Exit Core	$\kappa_{C,e} \frac{M_{C,e}^2(t)}{\rho_{l,sat}} \phi^2 x_{C,e}(t)$
Exit Chimney	$\kappa_{R,i} \frac{M_{R,i}^2(t)}{\rho_{l,sat}} \phi^2 x_{R,e}(t)$
Inlet Downcomer	$\kappa_{D,i} \frac{M_{D,i}^2(t)}{\rho_{l,sub}}$

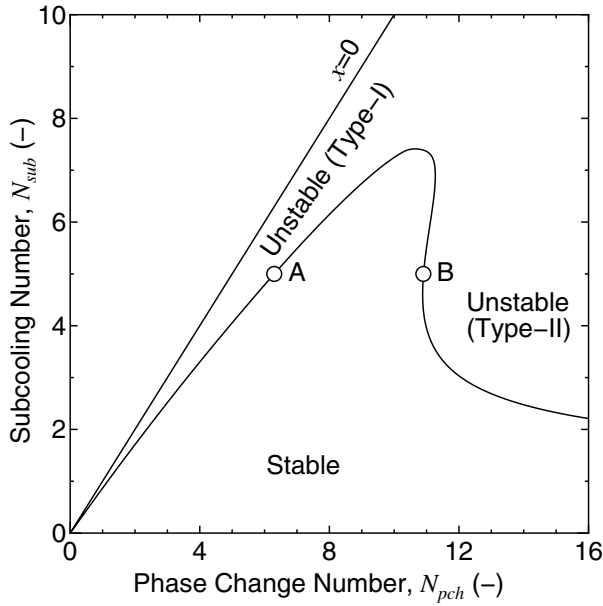


Figure 3.17: Stability boundaries are shown for Type-I and Type-II density wave oscillations in the phase change number - subcooling number plane. Points A and B are selected for representative Type-I and Type-II instability boundary conditions in this analysis.

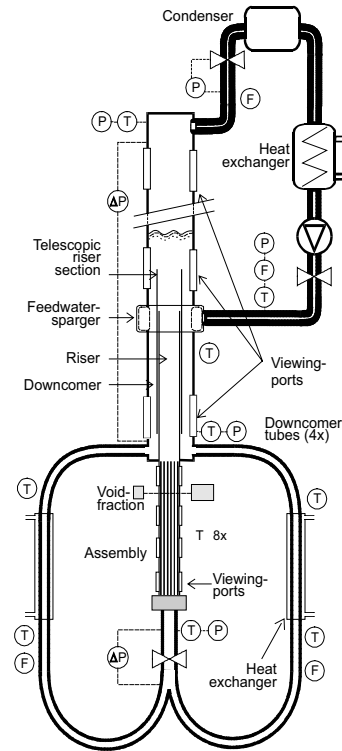


Figure 3.18: Schematic of DESIRE facility. P, T and F denote pressure, temperature and flow sensors, respectively. Freon R12 enters the heated section (962 mm) from the bottom.

The liquid density for the subcooled fluid, $\rho_{l,sub}$, was expanded from the liquid density for the saturation condition, $\rho_{l,sat}$, as a linear function of the fluid subcooling:

$$\rho_{l,sub} = \rho_{l,sat} - \frac{\partial \rho_l}{\partial T} \Delta T_{sub} \quad (3.13)$$

In order to demonstrate the effect of the single-phase liquid natural circulation on the stability, the DESIRE facility (Kok and Van der Hagen, 1999b,c) is selected as target of the stability analysis. This facility is designed and constructed by Delft University of Technology (Delft, the Netherlands) to investigate BWR natural circulation and reactor stability at nominal conditions; it is a scaled copy of the Dodewaard BWR (see Figure 3.11), which is cooled by natural circulation. Figure 3.18 shows a scheme of the DESIRE facility consisting of a single simulated BWR fuel assembly and its recirculation loop (including a chimney of variable length, condenser and downcomer). The test fluid used is Freon-12. The dimensions of the facility are summarized in Table 3.2. Rated conditions of the stability analysis are given in Table 3.3. The results described here are applicable for the ESBWR on the basis of the similarity law.

The solid lines in Figure 3.19 show the effect of fluid density differences on stability. Each line is drawn by changing the density derivative with respect to temperature (see equation 3.13) for the same power level as point A or B. The subcooling number is kept at 5. The density derivative of Freon-12 with respect to temperature is estimated as approximately $-4.2 \text{ kg/m}^3\text{K}$ at 1.14 MPa. Therefore, the influence of liquid density differences is exaggerated using values beyond this value, whereas zero on the horizontal axis indicates that liquid density differences are neglected; corresponding to the previous model. When the density difference ($\rho_{l,sub} - \rho_{l,sat}$)

Table 3.2: Dimension of DESIRE Facility

Parameter	Legend	Value
Core Height	L_C	0.95 m
Chimney Height	L_R	1.33 m
Downcomer Flow Area	A_D	$1.96 \times 10^3 \text{ m}^2$
Channel Flow Area	A_C	$1.78 \times 10^{-3} \text{ m}^2$
Chimney Flow Area	A_R	$3.15 \times 10^{-3} \text{ m}^2$

Table 3.3: Rated DESIRE Conditions for Stability Analysis

Parameter	Legend	Value
Test Fluid		R-12
System Pressure	P_s	1.14 MPa
Orifice Coefficient at Channel Inlet	$\kappa_{C,i}$	10
Orifice Coefficient at Channel Exit	$\kappa_{C,e}$	3.02
Orifice Coefficient at Chimney Exit	$\kappa_{R,e}$	1.00
Orifice Coefficient at Downcomer Inlet	$\kappa_{D,i}$	3.84

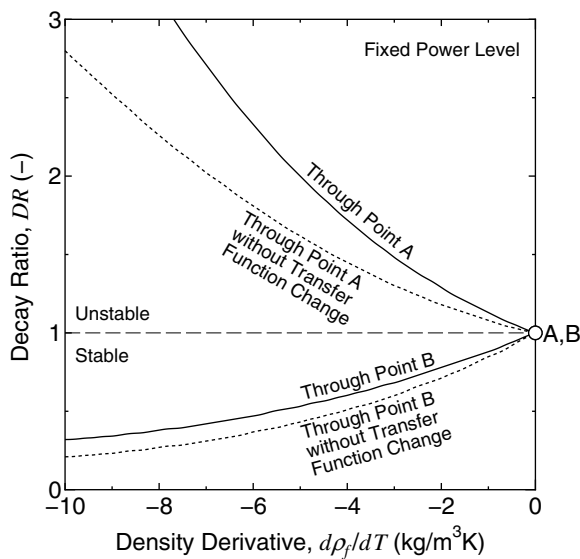


Figure 3.19: Stability effect of the liquid density derivative with respect to temperature. When the density difference is large, corresponding with a more negative density derivative, the decay ratio increases for point A, while it decreases for point B.

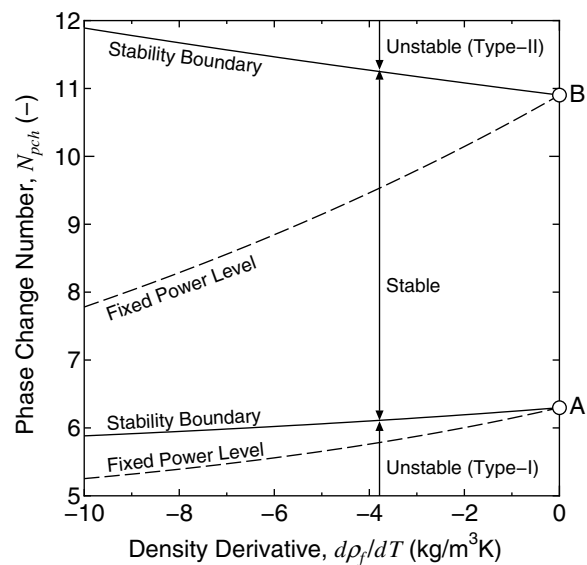


Figure 3.20: For Type-II instability, the overall effect of neglecting density differences is a too high decay-ratio estimate. For Type-I instability, on the other hand, it is a too low decay-ratio estimate, because the operating point shifts towards the stable region.

is large, corresponding with a more negative density derivative, the decay ratio increases for point A, while it decreases for point B.

The stability is both influenced by changes in the transfer function and by changes in the operating points. A sensitivity analysis is carried out to examine the influence of the transfer function itself. The dotted lines in Figure 3.19 show the influence on the stability of the shift in operating point, neglecting the density differences in the modeling of the transfer function.

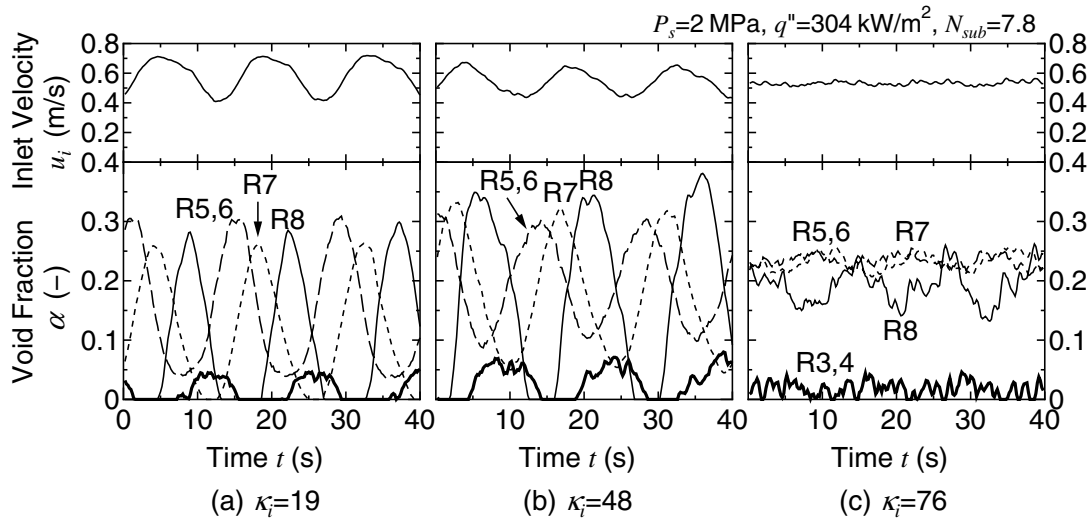


Figure 3.21: Effect of the inlet restriction on the inlet velocity and the void fraction at the locations R3 through R8. The inlet restriction is varied for $\kappa_i = 19, 48,$ and 76 . Increasing the inlet restriction reduces the amplitude of oscillation at this subcooling.

Comparing the dotted lines with the solid ones, it can be concluded that neglecting perturbations of density differences in the transfer function leads to a lower decay-ratio estimation and is therefore non-conservative for both points A and B. However, by comparing the solid lines in the figure with the decay-ratio value for the reference cases (no density effect; decay ratio is unity), two interesting conclusions can be drawn: for Type-II instability (as represented by point B) the overall effect of neglecting density differences is a too high decay-ratio estimate and is therefore a conservative estimation, because of the shift in operating point. For Type-I instability (as represented by point A), on the other hand, the overall effect of neglecting density differences is a too low decay-ratio estimate (non-conservative), because also the operating point shifts towards or into the stable region, when liquid density differences are neglected.

One has to realize that the flow rate increases due to liquid density differences, causing a decrease in the phase change number and a shift of the operating point in the stability map. Figure 3.20 demonstrates this shift of the operation condition due to liquid density differences. The phase change number decreases with reducing the density derivative for a fixed power level (dashed lines) for both operating points A (Type-I instability) and B (Type-II instability) since the flow rate increases. Stability boundaries are also drawn in Figure 3.20 as solid lines by searching operating condition where the decay ratio equals unity. Note that the subcooling number is equal to 5 for all cases. As indicated in Figure 3.17, the flow is stable in the internal region surrounded by two stability boundaries. As the density derivative becomes more negative, the phase change number for the fixed power level through point A decreases more than for the stability boundary and the flow becomes unstable. These findings support the conclusions given in the previous paragraph.

3.5 Effect of Inlet Throttling

Installing inlet throttle and an orifice are effective ways to stabilize the density wave oscillations under forced circulation conditions (Bouré *et al.*, 1973) due to the enlargement of the pressure drop in the single-phase section. These inlet restrictions, however, may not always stabilize the flow under natural circulation condition since a natural circulation flow rate decreases with increasing inlet restriction, leading to a relatively high power to flow ratio that is a typical

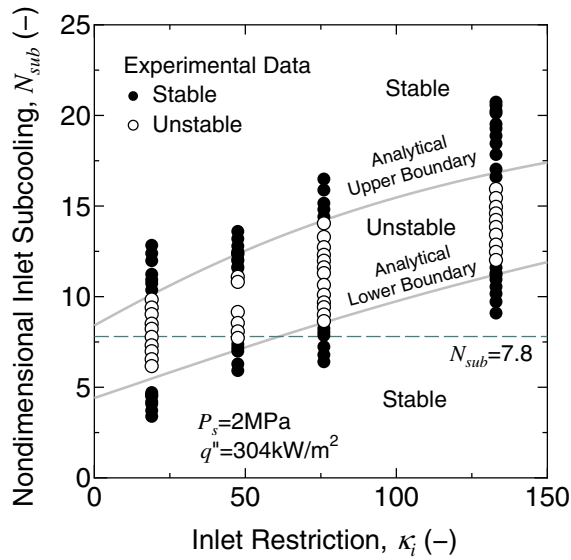


Figure 3.22: Stability map in reference to the inlet subcooling and the inlet restriction. Instability occurs within a certain range of the inlet subcooling. As the inlet restriction increases, the unstable range shifts to high inlet subcooling.

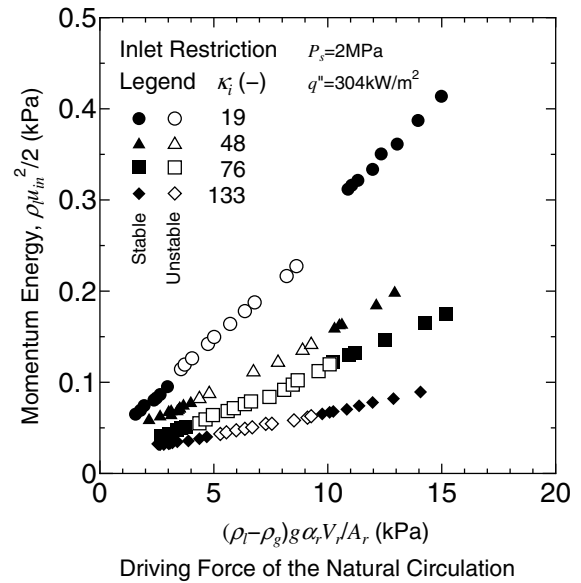


Figure 3.23: Relationship of the driving force of natural circulation to the momentum energy in reference to the inlet restrictions. Instability occurs within a certain range of the momentum force regardless of the inlet restriction.

condition of the density wave oscillations (Nayak *et al.*, 1998). The inlet restriction effect remains unknown especially with respect to the boiling natural circulation loop with a long and large diameter chimney comparing to the length and flow area of a heated section such as the natural circulation BWR.

3.5.1 Experimental Investigation

Experiments were conducted to investigate the inlet restriction effect on the thermal-hydraulic stability. The SIRIUS-N facility is used (see Figure 2.2 for detailed description). An orifice is inserted at each channel inlet. The orifice coefficient (κ_i) accounts to 19, based on the velocity at the channel inlet. The inlet restriction effect was examined by throttling a gate valve attached at the downcomer. Its local pressure drop was measured by a differential pressure measurement system and converted into enlargement of the inlet orifice coefficient (κ_i).

Figure 3.21 shows the time traces of the signals measured when the system pressure is 2 MPa, the heat flux is 304 kW/m², and the nondimensional inlet subcooling is 7.8. inlet velocities and void fractions for different inlet restrictions. The R3 through R8 in the figure corresponds to the measurement regions of differential pressures (see Figure 2.2). Operating conditions were fixed at the system pressure (P_s) of 2 MPa, a channel heat flux (q'') of 304 kW/m², and a nondimensional inlet subcooling (N_{sub}) of 7.8. It can be seen from the figure that the amplitude of the inlet velocity fluctuates decreases with increasing inlet restriction from 19 to 76, therefore the flow stabilizes by the inlet throttling.

Figure 3.22 shows a stability map in reference to the nondimensional inlet subcooling and the inlet restriction when the system pressure is 2 MPa and the channel heat flux is 304 kW/m². If the r.m.s. value of the inlet velocity exceeds 10% of an average, the flow condition is classified as unstable indicated by open circle. Otherwise, it is categorized as stable and plotted as a solid

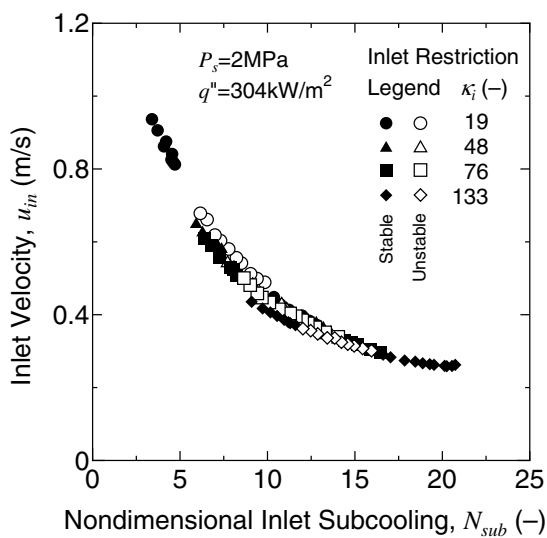


Figure 3.24: Decrease in the inlet velocity with increasing inlet restriction was small since increasing inlet restriction enlarges the momentum force of the natural circulation.

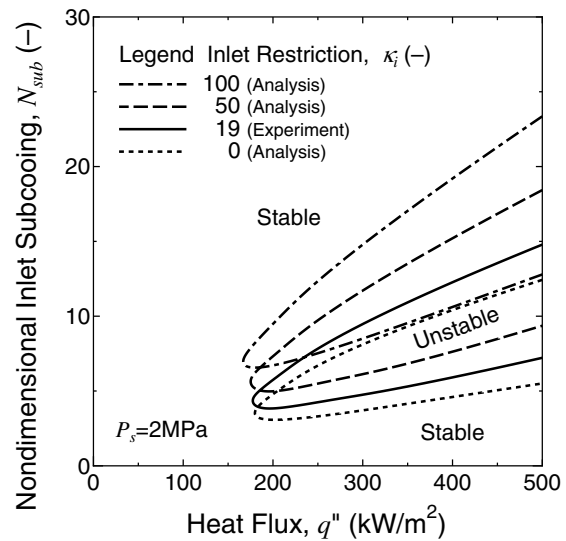


Figure 3.25: Analytical stability boundaries for various inlet restrictions. The unstable region shifts to higher inlet subcoolings with increasing inlet restriction and becomes larger with increasing heat flux.

circle. As investigated previously, increasing the inlet restriction stabilizes the flow for low inlet subcooling numbers. This result is consistent with the behavior of forced circulation loops under typical density wave oscillations, since increasing the inlet restriction reduces the relative magnitude of two-phase pressure loss perturbations. An opposite effect can be seen for high inlet subcoolings. If the flow loop is operated under natural circulation conditions, increasing the inlet restriction reduces the circulation flow rate and increases the void fraction leading to typical unstable conditions as depicted in Figure 3.22 for high subcooling condition. In total, the unstable region shifts to high inlet subcoolings.

Figure 3.23 shows the relationship of the driving force of natural circulation to momentum energy for different inlet restrictions when the system pressure is 2 MPa and the channel heat flux is 2 kW/m^2 . Stable and unstable flow conditions are plotted as solid and open symbols. Average values for the different inlet subcooling are on a straight line regardless of the flow condition (stable or unstable). The slope of the line becomes steeper with decreasing inlet restriction. It is found that instability occurs within a certain range of the driving force of the natural circulation (or the void fraction) regardless of the inlet restriction.

Figure 3.24 shows the relationship of the inlet velocity to inlet subcooling for different inlet restrictions. Different symbols are used for different flow conditions and the inlet restrictions. The inlet velocity decrease with increasing inlet restriction. The differences are, however, small for $\kappa_i = 19 - 133$, since increasing inlet restriction enlarges the momentum force of the natural circulation (proportional to the void fraction) as depicted in Figure 3.23.

3.5.2 Numerical Investigation

In order to extend the stability data base in terms of the inlet restriction, the stability boundary is estimated by a numerical analysis on the basis of the threshold value of the driving force of the natural circulation (or the void fraction). The numerical analysis is based on the homogeneous equilibrium mixture (HEM) model as described in Section 3.4.2. In this section,

we will estimate the stability boundary by the steady-state solution of the HEM model (static characteristics) without help of the linear stability analysis (dynamic characteristics).

The steady-state solution in terms of the void fraction and inlet subcooling is obtained by integrating momentum and energy equations over the circulation loop. As stated before, instability was observed within a certain range of the void fraction. Void fractions at the upper and lower stability boundary are converted into the inlet subcooling based on the steady state analytical solution, then plotted in Figure 3.22 as solid lines for a given pressure and heat flux. It can be seen that the analytical stability boundaries agree well with experimental ones. Therefore, the analytical model in terms of the inlet restriction is validated with the experimental data.

The numerical simulations were performed to obtain the stability boundaries for other channel heat flux conditions. Figure 3.25 is a stability map in the nondimensional inlet subcooling - channel heat flux plane for different inlet restrictions. As shown in Figure 3.25, the unstable region shifts to higher inlet subcoolings with increasing inlet restriction and becomes larger with increasing heat flux. As a result, the numerical analysis is shown to be able to extend the stability data base in terms of the inlet restriction.

3.6 Conclusions

- The observed oscillations are found to be density wave oscillations, since the void fraction fluctuations in the chimney inlet and exit are out of phase. They belong to the Type-I instability category since they occur at low flow qualities.
- Two distinct branches are found in the relation of the oscillation period and the liquid passing time in the chimney, indicating that the driving mechanisms of the instabilities are different for low and high pressures. The demarcation lies between 0.5 MPa and 1.0 MPa. The oscillation period correlates well with the passing time of bubbles in the chimney section regardless of the system pressure, the heat flux, and the inlet subcooling. This contrasts to the flashing induced density wave oscillations at low system pressures.
- Differences from other instabilities such as flow pattern transient oscillations, geysering, and natural circulation instability are indicated by investigating the transient flow pattern, the relationship of the oscillation period to the boiling delay time, and response of natural circulation driving force.
- Stability maps were obtained in reference to the inlet subcooling and the heat flux at the system pressures of 1, 2, 4, and 7.2 MPa. Instability was observed to occur within a certain range of inlet subcooling. The flow becomes stable below a certain heat flux regardless of the channel inlet subcooling. The stable region enlarges with increasing system pressure. Therefore, the stability enhances in a cold startup process of a reactor by pressurizing the reactor sufficiently before withdrawing the control rods (heating the reactor core). The obtained stability map demonstrates that the rated operating condition of the ESBWR is found to have significant stability margin (approximately 64 K of inlet subcooling) to the unstable region.
- The linear stability analysis code developed by Van Bragt and Van der Hagen (1998c) was used to predict stability boundaries at lower subcooling. The analytical stability boundary agrees well with the experimentally-obtained stability boundary. Moreover, the linear stability analysis demonstrates the relation of the oscillation period to the bubble passing time in the chimney.

- In order to investigate the effect of liquid density differences on thermal-hydraulic stability, the code is modified to include the dependence of liquid density on temperature. Analytical results show that neglecting density differences yields a conservative estimate of Type-II instability. On the other hand, it gives a non-conservative estimate of Type-I instability, since operating conditions shift towards or into the stable region. Therefore, it is recommended to include the dependence of liquid density on the temperature in a stability analysis, if a boiling natural circulation loop with an adiabatic chimney encounters low flow quality conditions.
- Experiments were extended to investigate the effect of inlet restriction. The instability region shifts to higher subcoolings with increasing inlet restriction. The void fraction at the stability boundary is approximately constant regardless of the inlet restriction for fixed system pressure and heat flux. Stability maps in reference to the inlet subcooling and the channel heat flux can be provided for different inlet subcooling based on the steady state analysis using experimentally-obtained momentum forces of the natural circulation at the stability boundary.

In the following chapters, the SIRIUS-N facility was modified to simulate core-wide and regional stabilities. The method to implement the artificial void-reactivity feedback is described in Chapter 4. Core-wide and regional stability experimental results are addressed and discussed in Chapter 5.

Chapter 4

Implementation Method for Neutronic-Thermalhydraulic Coupling

Abstract

A new method is implemented in the SIRIUS-F facility that simulates the real-time thermalhydraulic-neutronic interactions. By measuring the void-reactivity feedback in the reactor core by means of differential pressure sensors, an artificial void-reactivity feedback system could be implemented by using the modal kinetics of the reactor neutronics.

Solid-state, series-regulated power supplies that act as simulation output, were used to attain fast response speed without loss of accuracy (time constant of 0.3ms based on a step response test; accuracy of 99.9% in power amplitude and less than one degree of phase lag based on a noise response test within a target frequency range of 0.3 to 0.5 Hz).

A verification test was conducted to obtain the fuel rod time constant of the heater rods and the measurement system used in the SIRIUS-N facility. These delay times are added to the fuel rod time constant in the real-time simulation for an accurate simulation of core-wide and regional stabilities.

4.1 Introduction

Instability cannot occur in a single channel in a BWR only, because it is neutronically coupled with neighboring channels. Therefore, stability tests have been performed at operating BWRs for many years. In order to understand regional instability, early test programs at the Peach Bottom reactor (Larsen, 1978; Carmichael and Niemi, 1978) and Vermont Yankee reactor (Sandoz and Chen, 1983) provided a large quantity of data on core-wide stability and the onset of limit cycle oscillations in the natural circulation region of the power/flow map. Regional oscillations in the out-of-phase mode were first seen at the Caorso plant in 1982. Subsequently, another test program was set up in October 1983 (Gialdi *et al.*, 1984) to study out-of-phase mode oscillations. The stability test performed during the startup of the Leibstadt plant in 1984 also resulted in regional oscillations at minimum pump speed conditions. A few occurrences of regional oscillations have been observed in other plants as well.

In addition to stability experiments conducted in nuclear power plants, out-of-pile facilities have been built to study thermal-hydraulic stability. Since void-reactivity feedback does not exist in out-of-pile facilities, most of the facilities could only be used to estimate so-called channel stability, which is defined as the thermal-hydraulic stability at a fixed power condition. Uehiro (1997) was the first to introduce artificial void-reactivity feedback into the facility lo-

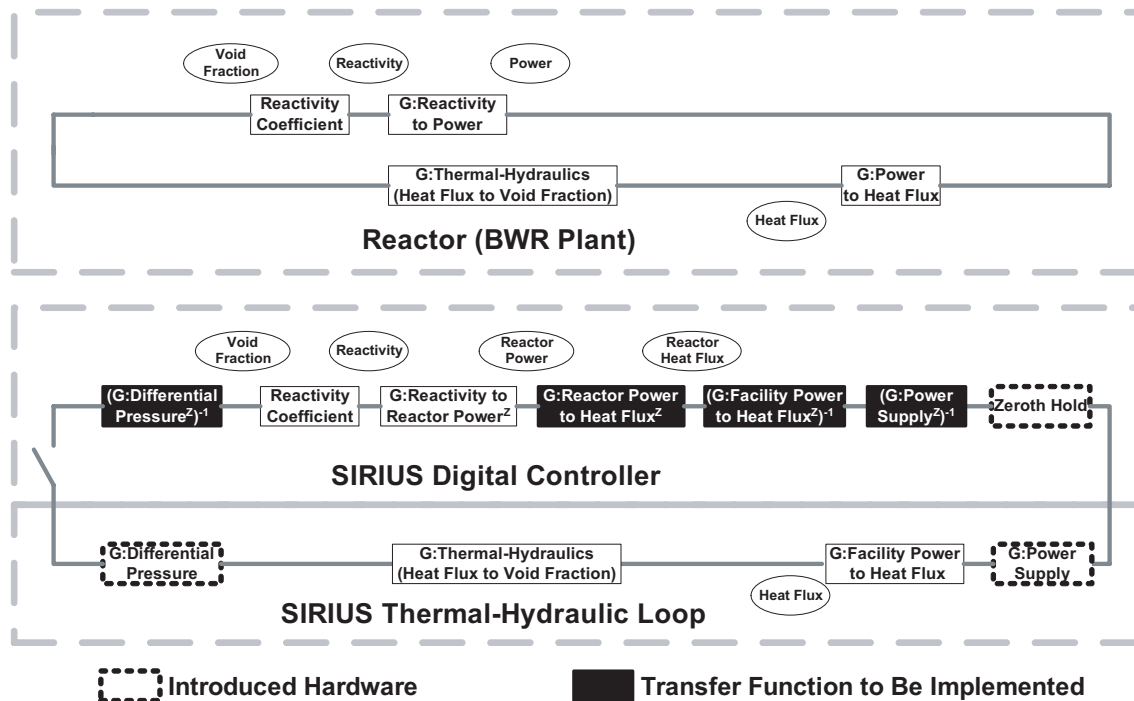


Figure 4.1: Block diagram representing the closed-loop transfer functions for void-reactivity feedback. Distortion of the set of transfer functions occurs upon installing measurement and controlling systems, which should be canceled out by including inversed transfer functions.

cated at Kyushu University, Japan. Later, Kok and Van der Hagen (1999a) designed a scaled loop (DESIRE), with Freon as the working fluid, at the Delft University of Technology, the Netherlands, and investigated instability characteristics in detail. Recently, Iguchi *et al.* (2000) and Iguchi *et al.* (2003) also constructed a core-wide stability facility (THYNC) at the JAERI research institute, Japan. However, the THYNC facility was not designed with the same friction factors as those in a BWR core, which are important in the simulation of BWR stabilities. All these facilities were used for fundamental research on core-wide stability. At present, there is no facility suitable for investigating regional stability.

This chapter describes the methodology to implement an artificial void-reactivity feedback in the SIRIUS-N facility, so that the core-wide and regional stabilities of a BWR can be determined accurately.

4.2 Methodology to Implement Artificial Void Reactivity Feedback

Void-reactivity feedback is a crucial phenomenon in core-wide and regional instabilities. In order to simulate the void-reactivity feedback, which does not exist in out-of-pile facilities, void fractions are measured over the core sections, and these are subsequently used as input for real-time simulations of the void-reactivity feedback and the modal point kinetics. The power supplies are controlled in accordance with the simulation output.

Figure 4.1 illustrates sets of transfer functions in terms of the core-wide and regional stabilities. The upper part describes the closed transfer function of a BWR including void-reactivity feedback. For instance, perturbations in void fractions feedback to themselves through void-reactivity, generated power density, surface heat flux, and thermal-hydraulic transfer functions. In order to reproduce core-wide and regional stabilities, one must perform a real-time simu-

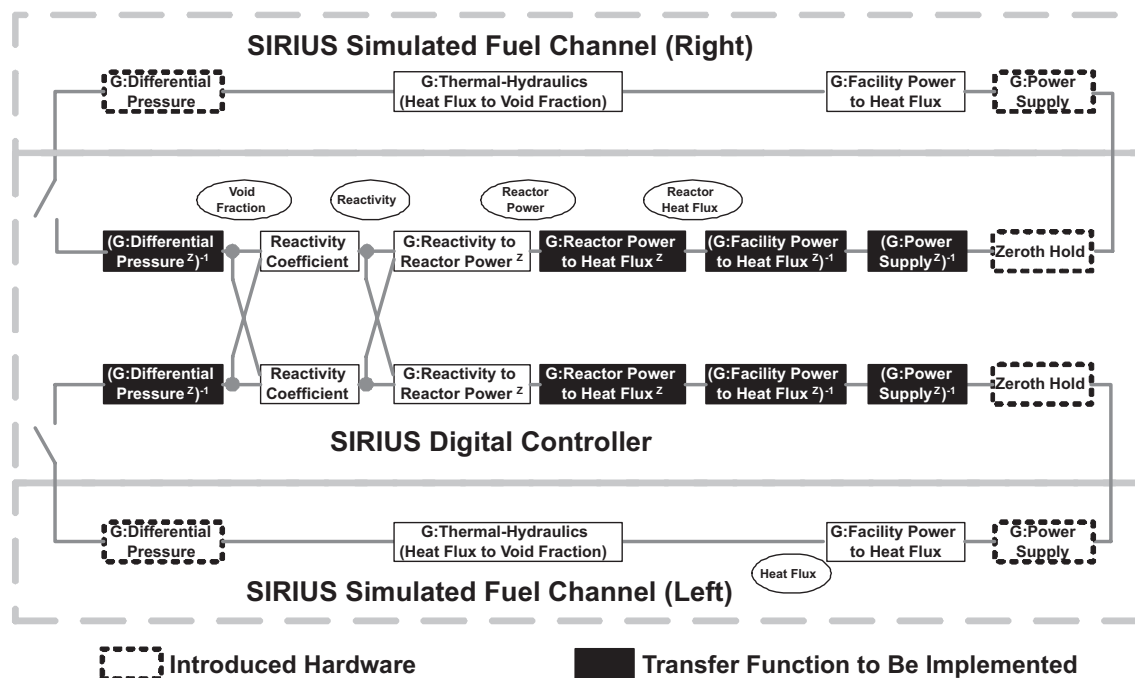


Figure 4.2: Transfer functions in terms of core-wide and regional stability. Interaction between half cores are analyzed in the digital controller through the transfer functions of 'Reactivity Coefficient' and 'Reactivity to Reactor Power.'

lation of the void-reactivity feedback. This simulation requires void fractions over the core sections as an input and controls the power supplies accordingly.

The lower part of Figure 4.1 illustrates a block diagram representing the closed-loop transfer functions for the void-reactivity feedback. The fuel pellets of a BWR are ceramic and the time constant in terms of gap conductance and heat conduction in cladding and fuel pellet ranges from 4 to 8 s depending on the composition and diameter of the pellet, pellet-to-cladding gap conductance. In contrast, the typical time constant of a metallic heater, which is commonly used in the out-of-pile facility, is approximately 1 s. Therefore, two additional transfer functions should be implemented to cancel out these differences: the inversed transfer function of thermal conduction in the metallic heater and a transfer function of thermal conduction in the target fuel.

One must note that distortion of the set of transfer functions occurs upon installing measurement and controlling systems, which should be canceled out by including inversed transfer functions, as illustrated in Figure 4.1.

Although the illustrated transfer functions comprise one single channel, neutron diffusion in space and the multichannel effect of thermal-hydraulics should also be considered in a BWR configuration. In this study, two simulated fuel channels are used to represent half cylindrical cores to demonstrate the fundamental mode (core-wide stability) and the first-azimuthal mode (regional stability). Figure 4.2 shows two set of transfer functions and these interactions. Interactions between two simulated fuel channels are solved numerically in order to take account of reactivity exchange between them (Hashimoto, 1993). Detailed formulation of the reactor neutronics is described in Section 4.4.2.

4.3 Measurement and Control System

Figure 4.3 shows the measurement and control system of the SIRIUS-N facility. A digital controller cluster consists of five computers (SIRIUS-PC1 to PC5). Each computer has a 100Base-

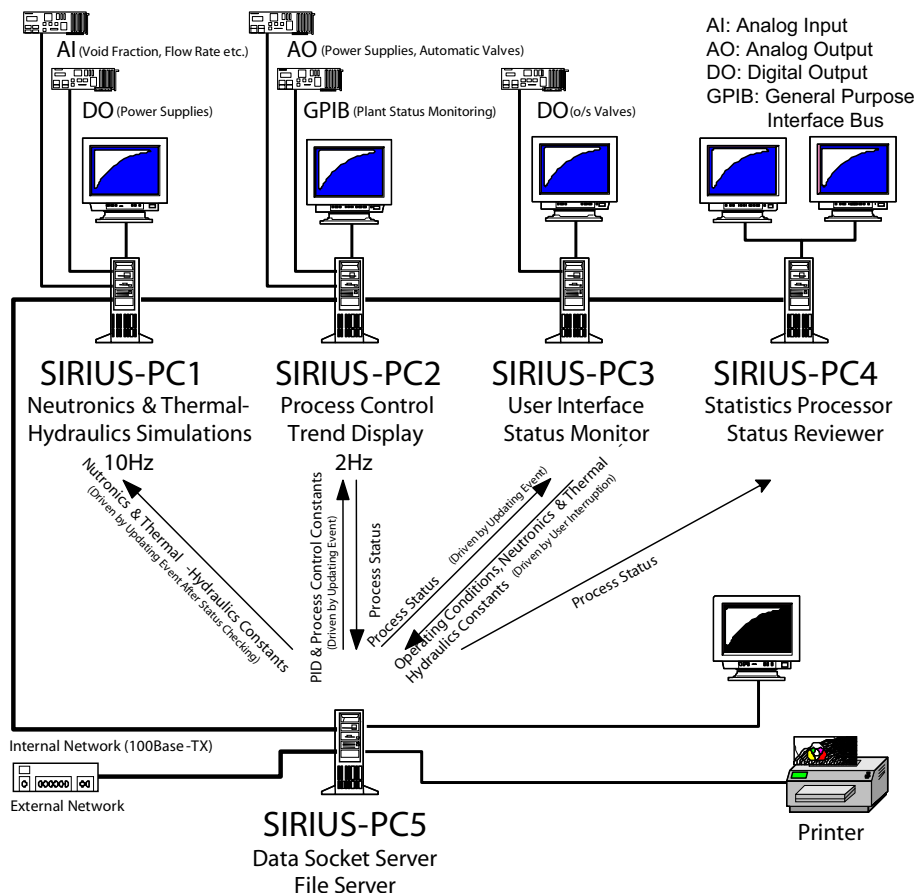
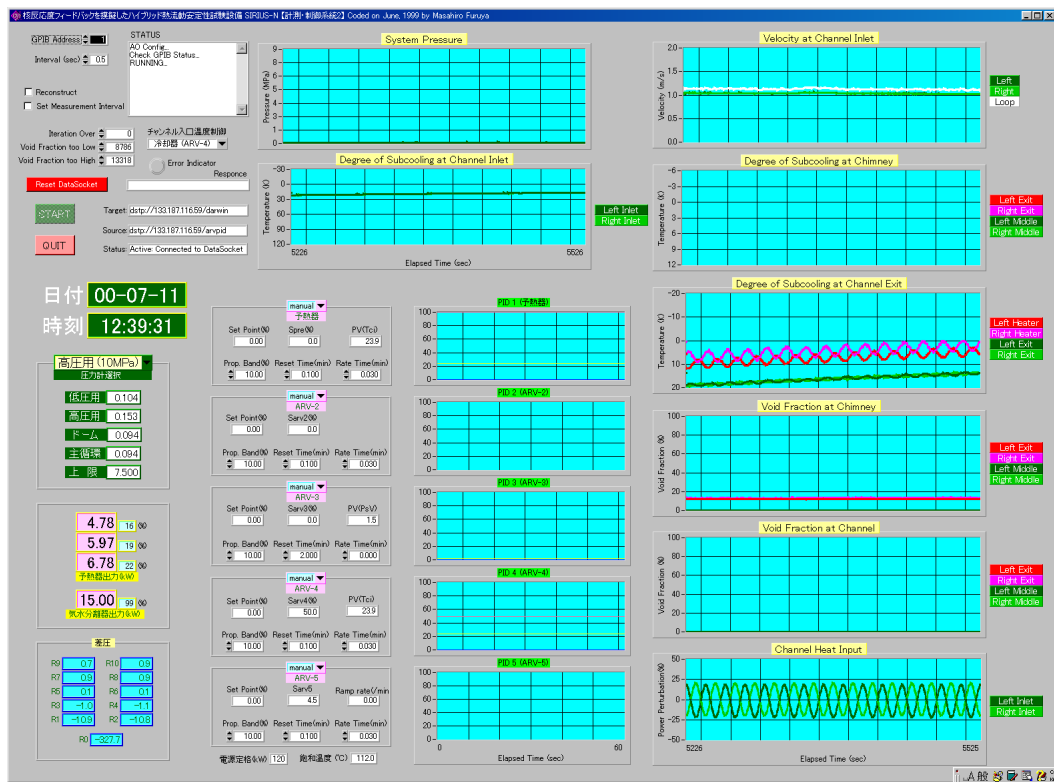


Figure 4.3: Overview of the digital controller of the SIRIUS-N facility. The digital controller cluster consists of five computers. Each computer has its own role in a distributed processing system.

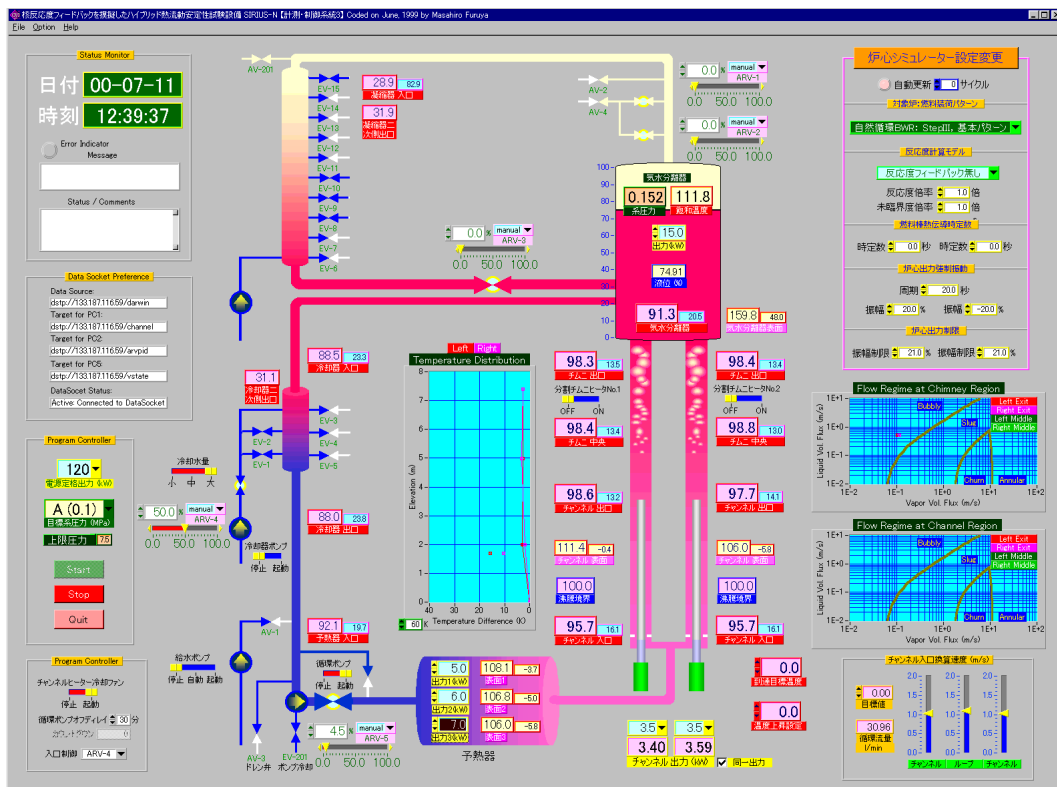
TX NIC and is connected with other computers via a switching hub using a TCP/IP protocol.

SIRIUS-PC1 acquires data, performs real-time simulation, and sends the simulation output to the power supplies via a 16-bit digital line. It repeats the process at 10 Hz synchronized with a hardware timer with a timing error smaller than 0.05 ms. SIRIUS-PC2 acquires whole-plant conditions at 2 Hz, which is sufficiently higher than the thermal-hydraulic oscillation frequency for the prototypical natural circulation BWR ($0.004 \text{ Hz} < f < 0.15 \text{ Hz}$). SIRIUS-PC2 also calculates the void fractions, velocities, temperatures, and thermal powers from the measured values, then sends them to the network server, SIRIUS-PC5.

Figure 4.4 shows the trend panel of SIRIUS-PC2 and the status monitor of SIRIUS-PC3. These graphical user interfaces (GUIs) provide information on the temperature distribution and flow pattern as well. An operator can change constants relevant for the reactor kinetics and the fuel rod time constant online at any time. A PID control system enables us to set boundary conditions automatically without help of manual operations. This automation feature is practically important to attain stability data with high accuracy. SIRIUS-PC4 can reproduce previous data at any specified time from the accumulated database in the network server (SIRIUS-PC5). It also can perform time-series analysis to estimate the decay ratio and the resonance frequency, and to perform statistical calculations.



(a) SIRIUS-PC2 Trend Display Panel



(b) SIRIUS-PC3 Plant Status Display Panel

Figure 4.4: User Interfaces of SIRIUS-N Control and Monitoring System

4.4 Formulations of Real-Time Analysis

4.4.1 Thermal-hydraulics

In order to implement the artificial void-reactivity feedback, the void fraction must be acquired with high accuracy. Furthermore, the acquired void fraction should be consistent with the value that has to be used for the void-reactivity model. Iguchi *et al.* (2000) and Iguchi *et al.* (2003) and Kok and Van der Hagen (1999a) used a locally measured void fraction for void-reactivity feedback simulation. In an oscillatory flow, an axial profile of void fraction cannot be estimated from the locally measured void fraction only. Moreover, the local void fraction fluctuates with large amplitude by nature of the two-phase flow: e.g. slug flow, which is a coarse mixture of dispersed vapor bubbles in a continuous liquid. Therefore, use of the local void fraction can overestimate the amplitude of void reactivity.

Therefore in this study, the void fraction along the core section was acquired from the differential pressure over the heated channel section together with the inlet velocity and inlet temperature. The method to estimate the void fraction from the differential pressure has been described in Section 2.2.3.

4.4.2 Neutronics

Hashimoto (1993) derived the linearized formulation of reactor neutronics including the eigenvalue separation of the higher-harmonic neutronic mode, as follows:

$$\frac{dn_m(t)}{dt} = -\frac{\rho_m^S(t) + \beta}{\Lambda_m} n_m(t) + \lambda c_m(t) + \frac{\rho_{m0}^F(t)}{\Lambda_m} N_0 + \sum_{n=0}^{\infty} \frac{\rho_{mn}^F(t)}{\Lambda_m} n_n(t), \quad (4.1)$$

$$\frac{dc_m(t)}{dt} = \frac{\beta}{\Lambda_m} n_m(t) - \lambda c_m(t). \quad (4.2)$$

N_0 is the density of prompt neutrons at criticality. n and c are variations in precursor number densities of prompt and delayed neutrons, respectively. λ is the decay constant of the delayed neutron precursor, β denotes the delayed neutron fraction and Λ the generation time of prompt neutrons. Subscripts n and m indicate the order of the higher harmonic mode. $\rho_m^S(t)$ is the subcriticality (λ -mode eigenvalue separation) of the m -th harmonic mode, defined as:

$$\rho_m^S(t) \equiv \frac{1}{\lambda_m} - 1, \quad (4.3)$$

where λ_m is the m -th mode eigenvalue. $\rho_{mn}^F(t)$ is the excitation reactivity of the m -th mode.

When liquid turns into vapor ('void') the neutron balance is affected via changes of the neutron absorption and scattering cross-sections, leading to a reactivity change. In fact, even the neutron fission cross section is influenced via changes of the neutron spectrum. We assume that the change in neutron absorption is dominating the core-wide instability and regional instability. Using first-order perturbation theory (Ott and Neuhold, 1985) a change of macroscopic absorption cross section $\delta\Sigma_a(\vec{r}, t)$ leads to a reactivity change $\rho_{mn}^F(t)$ as :

$$\rho_{mn}^F(t) \approx -\frac{\int d\vec{r} \phi_m^*(\vec{r}) \phi_n(\vec{r}) \delta\Sigma_a(\vec{r}, t)}{\int d\vec{r} \phi_m^*(\vec{r}) \phi_m(\vec{r}) \nu \Sigma_f(\vec{r})}, \quad (4.4)$$

where $\phi_m(\vec{r})$ is the neutron flux of the m -th harmonic mode, the superscript '*' indicates its adjoint function. ν denotes the average number of neutrons released per fission and $\delta\Sigma_f(\vec{r}, t)$ is the macroscopic fission cross section.

As the phase lag of the void fraction between inlet and exit of the core is small for a prototypical natural circulation BWR, only one differential pressure was used to estimate the void fraction in a channel. The axial power profile is uniform for the SIRIUS-N facility, which yields a simplified description of the void reactivity changes. The void reactivity changes of the fundamental and first-azimuthal modes are then given by,

$$\rho_{00}^F(t) = \rho_{11}^F(t) = \frac{1}{2} [C_\alpha(\alpha_{ch1})\delta\alpha_{ch1} + C_\alpha(\alpha_{ch2})\delta\alpha_{ch2}], \quad (4.5)$$

$$\rho_{01}^F(t) = \rho_{10}^F(t) = \frac{1}{2} [C_\alpha(\alpha_{ch1})\delta\alpha_{ch1} - C_\alpha(\alpha_{ch2})\delta\alpha_{ch2}], \quad (4.6)$$

where C_α is the void reactivity coefficient as a function of the void fraction, and α_{ch1} and α_{ch2} are the void fractions in the simulated fuel channels 1 and 2 of the SIRIUS-F facility, respectively.

For forced circulation BWRs without a chimney, however, the phase lag in the void fraction is large within the core. Therefore, differential pressures were measured at seven different regions to estimate the void reactivity, as we will discuss in Chapter 6. In addition, the axial power profile is bottom-peaked instead of uniform (which is often used for licensing reasons since this profile destabilizes the regional mode). Detailed descriptions and formulations will be described in Section 6.3.

In order to estimate core-wide and regional stabilities, the fundamental mode ($m=0$) and the first azimuthal mode ($m=1$) are considered. Neglecting other higher harmonic modes yields (Muñoz-Cobo *et al.*, 2000):

$$\frac{dn_0(t)}{dt} = \frac{\rho_{00}^F(t) - \beta}{\Lambda_0} n_0(t) + \frac{\rho_{00}^F(t)}{\Lambda_0} N_0 + \frac{\rho_{01}^F(t)}{\Lambda_0} n_1(t) + \lambda_{c0}(t), \quad (4.7)$$

$$\frac{dn_1(t)}{dt} = \frac{\rho_{10}^F(t)}{\Lambda_1} (N_0 + n_0(t)) + \frac{\rho_{11}^F(t) - \varepsilon - \beta}{\Lambda_1} n_1(t) + \lambda_{c1}(t), \quad (4.8)$$

$$\frac{dc_0(t)}{dt} = \frac{\beta}{\Lambda_0} n_0(t) - \lambda_{c0}(t), \quad (4.9)$$

$$\frac{dc_1(t)}{dt} = \frac{\beta}{\Lambda_1} n_1(t) - \lambda_{c1}(t). \quad (4.10)$$

The λ -mode eigenvalue separation of the first azimuthal mode is rewritten as ε ($= \rho_1^S(t) = 1 / \lambda_1 - 1$). n_0 and n_1 can be obtained by solving the differential equation (4.7) - (4.10). The heat generation rate per unit volume in channel 1 (q_{ch1}''') and in channel 2 (q_{ch2}''') are determined as follows:

$$q_{ch1}''' = C_{ch1} [N_0 + n_0(t) + n_1(t)] \quad (4.11)$$

$$q_{ch2}''' = C_{ch2} [N_0 + n_0(t) - n_1(t)] \quad (4.12)$$

C_{ch1} and C_{ch2} are proportional constants of the number density to the power generation rate per unit volume in the simulated fuel channels 1 and 2 of the SIRIUS-N facility.

4.4.3 Thermal Conduction in the Fuel Rod

The thermal conduction in the fuel rod is formulated as point kinetics. The representative temperature of the fuel rod, T_f , is expressed on the basis of thermal conduction as

$$\rho_l C_p l A_f \frac{dT_f}{dt} = A_f q''' - P_h q'' \quad (4.13)$$

Where ρ_l is the density, C_{pl} the specific heat at constant pressure of the fuel rod. q'' is the surface heat flux, and q''' is volumetric heat generation in the fuel rod. P_h is the perimeter and A_f is cross sectional area of the fuel rod.

The overall heat transfer coefficient, $h_{overall}$, based on the degree of superheat, $T_f - T_{sat}$, is

$$q'' = h_{overall} (T_f - T_{sat}). \quad (4.14)$$

The fuel rod time constant, τ_f , is defined as

$$\tau_f \equiv \frac{\rho_l C_{pl} A_f}{h_{overall} P_h}. \quad (4.15)$$

Using the above expressions yields the nondimensional form of equation (4.13),

$$\frac{d\hat{q}''}{dt} = \frac{1}{\tau_f} (\hat{q}''' - \hat{q}''). \quad (4.16)$$

The symbol ' $\hat{\quad}$ ' denotes nondimensionalized variables, following

$$\hat{q}'' \equiv \frac{q''}{q_0''}, \quad (4.17)$$

$$\hat{q}''' \equiv \frac{A_f q'''}{P_h q_0''}. \quad (4.18)$$

Here, q_0'' is the surface heat flux under the critical state.

4.5 Identification of Transfer Functions

As discussed in Section 4.2, three transfer functions related to hardware are introduced in the set of transfer functions (see Figure 4.1): the power supply, the heater rod, and the differential pressure measurement system. In the following section, we will identify those three transfer functions.

4.5.1 Power Supply

The power supply is the output device of the real-time simulation that controls the thermal power. In most cases, a thyristor-controlled power supply is used for heating at such a large power (120 kW/ch for the SIRIUS-N facility). Delay of the power supply in its response, however, generally takes 1 to 2 s, which is of the same order of magnitude as the oscillation period of a forced circulation BWR, being 2 to 3 s. Therefore, it is difficult to use this type of power supply to implement the artificial void-reactivity feedback.

In order to achieve a fast response and high accuracy, solid-state, series-regulated power supplies are used with 3,300 transistors/unit. The linearity of the developed power supply is 0.05% over the full scale (120kW). Figure 4.5 shows a step response of the power supply. The digital-analogue converter caused a 0.05 ms delay in the initial stage. After that, the response curve followed the first-order delay function of 0.3 ms, as illustrated in Figure 4.5. This time constant agrees with that of the CR circuit used to stabilize the control system of the power supply. The response of the power supply is sufficiently fast, since the time constant is four orders of magnitude smaller than the oscillation period of BWRs (2 to 3s).

Figure 4.6 shows the Gaussian white noise response of the power supply. Noise analysis was performed on the basis of the Blackman-Tukey model for 16 000 samples at a sampling

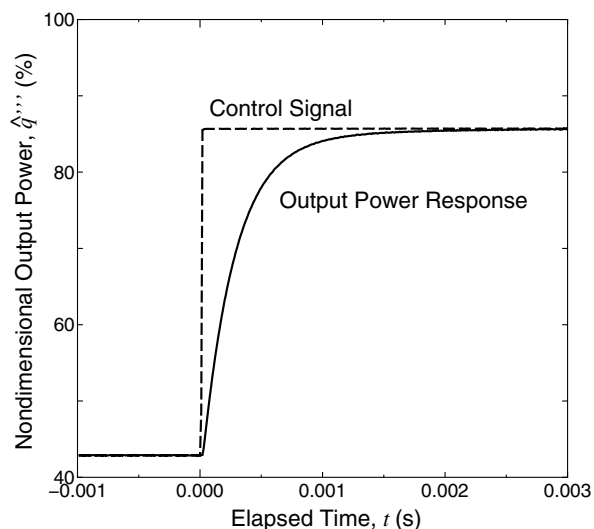


Figure 4.5: Indicial response of the developed power supply. The response curve followed the first-order delay function of 0.3 ms.

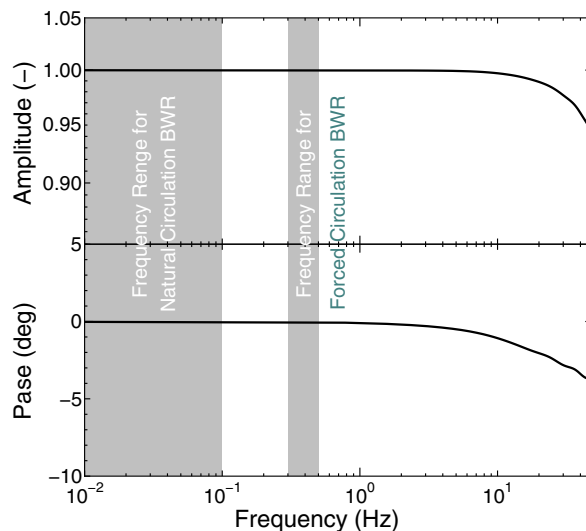


Figure 4.6: Noise response of the developed power supply. The accuracy of the amplitude was more than 99.9 % and the phase lag was less than 1 degree.

Table 4.1: Heater Rod Parameters in Thermal Conductivity Experiment

Parameter	Symbol	Range
System Pressure	P_s	0.12, 7.20 MPa
Inlet Subcooling	$\Delta T_{sub,in}$	1 - 58 K
Inlet Velocity	u_{in}	0.3 - 1.7 m/s
Base Power	q_0	0 - 30 kW
Target Power	q_1	0 - 30 kW
Step Height	$q_1 - q_0$	4.5 - 30 kW

rate of 200 samples/s. The accuracy of the amplitude was more than 99.9 % and the phase lag was less than 1 degree within the frequency range for forced circulation and natural circulation BWRs. The same results were obtained for periodic random noise as input signals. It can be concluded that the response and the accuracy of the power supply are sufficiently fast and accurate for studying the core-wide and regional stability of BWRs.

4.5.2 Heater Rod

An experiment was conducted to obtain the fuel rod time constant of the heater rod used in the SIRIUS-N facility. The temperature response was acquired from the thermocouples embedded in the heater rod surface with stepwise increase and decrease of the heater power. Seventeen measurements were conducted for different values of system pressure, inlet subcooling, inlet velocity, and power as listed in Table 4.1. Figure 4.7 shows a typical response of the heater surface temperature with stepwise increase of the heater power. It was found that the fuel rod time constant ranged from 0.7 to 1.1 s among the 17 cases. We therefore assumed a fixed time constant of 0.9 s, being the average of the time constant found in the 17 measurements.

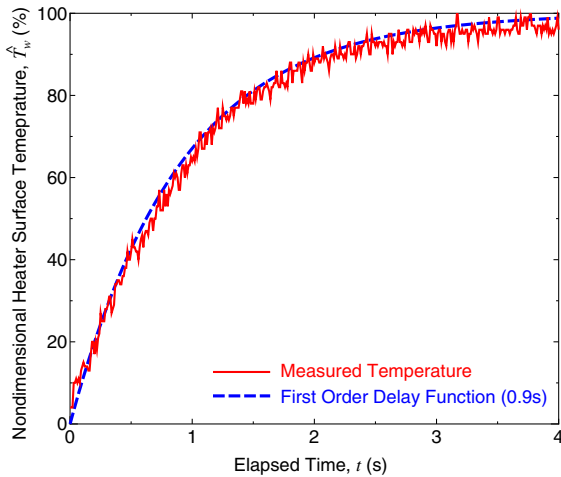


Figure 4.7: Thermal conductivity time constant of heater rod. The indicial response curve follows the first-order delay function of 0.9 s.

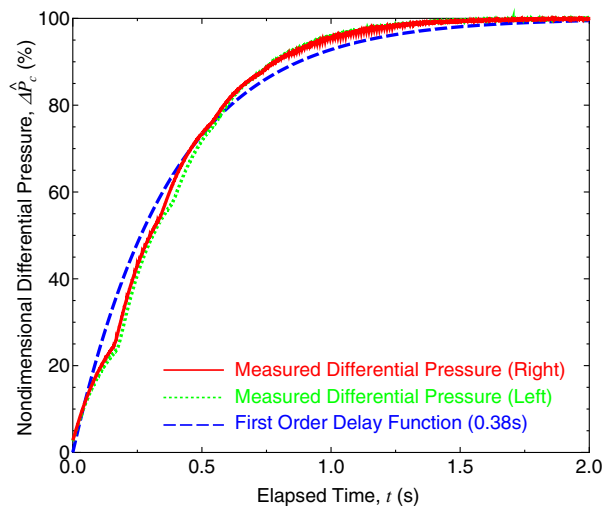


Figure 4.8: Time constant of DPMS. The indicial response curve followed the first-order delay function of 0.38 s.

4.5.3 Differential Pressure Measurement System

The differential pressure measurement system (DPMS) has a certain delay in its response to differential pressure changes. There are two different damping mechanisms in the DPMS. One is mechanical damping of the diaphragm and the other is electronic damping of the distributor. Figure 4.8 shows the response of DPMS with a stepwise increase of the differential pressure. Although there were two time constants corresponding to the two mechanisms, the curve followed the first-order delay function of 0.38 s, as illustrated in Figure 4.8.

Time delays of 0.38 s (DPMS) and 0.9 s (heater rod) are added to the fuel rod time constant in the real-time simulation. Subsequently, the fuel rod time constant indicated as an experimental parameter, τ_f , includes these time delays.

4.6 Conclusions

- In order to simulate core-wide and regional stabilities, a real-time simulation of the void-reactivity feedback was implemented in a boiling two-phase flow loop. By using the measured void fractions in the reactor core sections of the thermal-hydraulic loop, a real-time simulation of the void-reactivity feedback based on the modal point kinetics of reactor neutronics could be established.
- Solid-state, series-regulated power supplies that act as simulation output, were developed to attain fast response speed without loss of accuracy (time constant of 0.3 ms based on a step response test; accuracy of 99.9 % in power amplitude and less than one degree of phase lag based on a noise response test within a target frequency range of 0.3 to 0.5 Hz).
- An experiment was conducted to obtain the fuel rod time constant of the heater rods used in the SIRIUS-N facility. The temperature response curves agree well with the first-order time delay function of 0.9 s. The differential pressure measurement system (DPMS) measuring the void fraction has a certain delay in its response to differential pressure changes. The DPMS response curves follow the first-order delay function of 0.38 s. These delay times are added to the fuel rod time constant in the real-time simulation.

Experimental results of core-wide and regional stabilities, where this void reactivity feedback system has been implemented, will be discussed in Chapter 5. In Chapter 6, this system will also be applied to a forced circulation BWR.

Chapter 5

Natural Circulation BWR Core-Wide and Regional Stabilities

Abstract

The method to implement the artificial void-reactivity feedback described in Chapter 4 is used for the estimation of the core-wide and regional instabilities that may occur in a natural circulation BWR. Experiments were conducted with the SIRIUS-N facility. Channel and regional stability decay ratios were found to be 0.38 and 0.54, respectively at rated operating conditions, indicating sufficient margin for instabilities. The experiments were extended to evaluate the stability sensitivity of the design parameters such as the power profile, the void reactivity coefficients, core inlet subcooling, and the thermal conductance of the fuel rod. Regional instability was encountered, when the fuel rod time constant matches the oscillation period of density wave oscillations.

5.1 Introduction

Core-wide oscillations and regional oscillations have been observed in several forced circulation BWRs (D'Auria *et al.*, 1997) under close-to-natural circulation conditions where the stability margin is lowest in the power/flow map. The term 'core-wide oscillations' refers to the case when oscillations of neutron flux and flow in all the regions of the core are in phase. While the term 'regional oscillations' refers to oscillations of neutron flux and flow in different regions of the core, which are out of phase with respect to each other. Most of the regional oscillations observed are in the first azimuthal mode and therefore out of phase between symmetry regions separated by a diagonal line of the core, since that mode has the highest reactivity of all higher harmonics. The stability margin to regional oscillation becomes smaller when (1) nuclear coupling between regions in the core becomes weaker, (2) channels are thermal-hydraulically less stable, and (3) the reactivity of the corresponding neutronic mode increases, such as with a larger core diameter.

In Chapters 2 and 3, we experimentally examined thermal-hydraulic stability of the natural-circulation BWR with the SIRIUS-N facility, thereby neglecting the void-reactivity feedback. As a result of the experiment, we found two different types of oscillations: flashing-induced density wave oscillations at relatively low pressures (0.1 - 0.5 MPa) and Type-I density wave oscillations at relatively high pressures (1 - 7.2 MPa), and investigated the conditions and mechanisms of occurrence of these instabilities.

In this chapter, we demonstrate and investigate core-wide and regional stability for a natural

circulation BWR. As described in Chapter 4, the void-reactivity feedback simulation was implemented in the SIRIUS-N facility. The stability was determined by measuring by decay ratio and resonance frequency on the basis of noise analysis. The stability characteristics will be discussed based on the parametric study of design parameters of a prototypical natural circulation BWR such as the power profile, the void reactivity coefficients, core inlet subcooling, and the thermal conductance of the fuel rod.

5.2 Stability Estimation Based on Noise Analysis

The stability of the BWR is usually quantified by its decay ratio and resonance frequency as well as the distance of operating conditions to the conditions on the stability boundary. In this section, we introduce a method to analyze the decay ratio and resonance frequency from time series of the signals obtained in the experiments. The method is applied to the acquired data from the SIRIUS-N facility.

5.2.1 Method Description

The closed-loop transfer function, describing the BWR dynamics (core-wide and regional stabilities) has several poles, which are real and/or complex conjugate numbers. Each decay ratio (DR) and resonance frequency (f) can be found by using a pole ($s = \sigma + i\omega$) as follows:

$$DR = e^{\frac{2\pi\sigma}{|\omega|}} \quad (5.1)$$

$$f = \frac{|\omega|}{2\pi}. \quad (5.2)$$

The least stable pole (the largest $\sigma/|\omega|$) determines the stability of the system. In this study, noise analysis was performed to obtain the decay ratio and the resonance frequency by using a time-series of the measured inlet flow rate as follows:

1. In order to obtain a high signal to noise ratio, a linear trend is estimated and then removed from n points of the time-series on the basis of the best straight-line fit.
2. A transfer function in the z -plane, $G(z)$, is estimated by m -th order auto-regressive (AR) model on the basis of Yule-Walker method:

$$G(z) = \frac{c_z}{1 + a_2z^{-1} + a_3z^{-2} + \dots + a_{m+1}z^{-m}}, \quad (5.3)$$

where c_z and a_2, a_3, \dots, a_{m+1} are constants. The Yule-Walker method was selected which gives appropriate coefficients when the signals are relatively stable (De Hoon *et al.*, 1996).

3. Poles, p_1, p_2, \dots, p_m , can be obtained from a partial-fraction expansion of the transfer function:

$$G(z) = \frac{r_1}{1 - p_1z^{-1}} + \frac{r_2}{1 - p_2z^{-1}} + \dots + \frac{r_m}{1 - p_mz^{-1}} \quad (5.4)$$

The magnitude of the residues, r_1, r_2, \dots, r_m , indicates the importance of the corresponding pole.

Table 5.1: Parameters in Parametric Study on Noise Analysis at Rated Operating Conditions

Parameter	Legend	Unit	Reactor	SIRIUS-N
System Pressure	P_s	MPa	7.07	7.20
Heat Flux at Criticality	q_0''	kW/m ²	685	685
λ -mode eigenvalue separation	ε	\$	0.61	0.61
Fuel Rod Time Constant	τ_f	s	4.7	4.7
Nondimensional Core Inlet Subcooling	N_{sub}	-	0.65	0.65

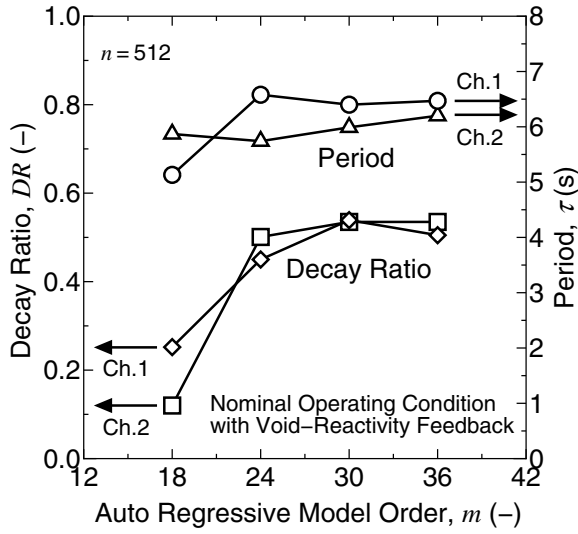


Figure 5.1: Effect of auto regressive model order. When $24 \leq m \leq 36$, decay ratios for both channels are approximately 0.5 and are in good agreement. m is set to be 30 which shows a rather good agreement between the channels.

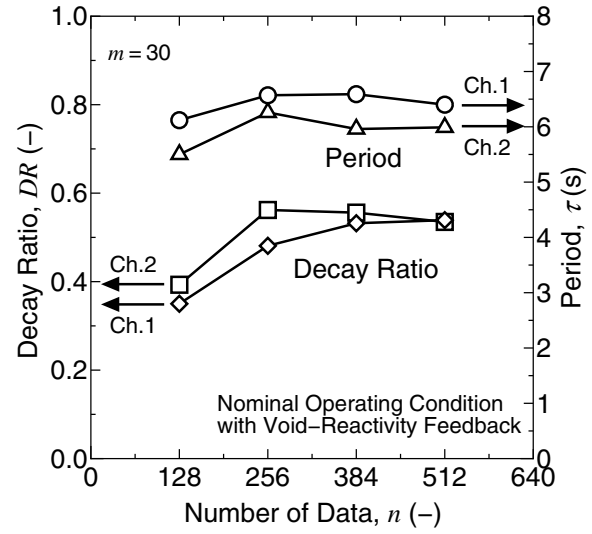


Figure 5.2: Effect of data size for the noise analysis. At least 384 points of time-series data are required for accurate estimation of decay ratio. Therefore, n is set to be 512, since n is more than seven times larger than AR model order.

4. The most dominant pole in the s -plane ($s = \sigma + i\omega$) is obtained by converting from the z -plane ($z = z_r + iz_i$) as:

$$\sigma = \frac{\log(z_r^2 + z_i^2)}{2\Delta t} \quad (5.5)$$

$$\omega = \frac{\tan^{-1} \frac{z_i}{z_r}}{\Delta t} \quad (5.6)$$

5. Decay ratios and frequencies are estimated from equations (5.1) and (5.2).

5.2.2 Optimization of Model Parameter

In order to estimate the decay ratio and the resonance frequency, we must determine two parameters: the AR model order (denoted as m) and the number of data (denoted as n). The optimal value for m can be determined according to an information conduct such as the AIC (Akaike's Information Criterion) (Akaike, 1974) as a function of number of data, n . In this study, m and n were, however, determined by the parametric study using experimental data from the SIRIUS-N

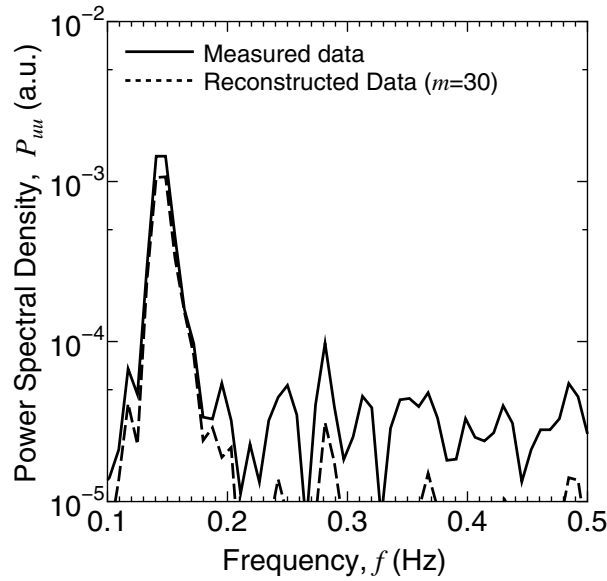


Figure 5.3: In order to demonstrate the validity of the applied AR method, power spectral density of the reconstructed data is compared with that of the measured (original) data. Because of noise and small number of data, high frequency noise contributes to the measured data. Nevertheless, the power spectral density of the measured data is successfully reproduced by the reconstructed data at the dominant frequency of 0.15 Hz.

facility, since the number of available data under a fixed boundary conditions is limited in the experiment.

Experimental parameters and their range (which will be described later) in the parametric study are listed in Table 5.1 together with the rated conditions of a prototypical natural circulation BWR. For a parametric study, time-series data were acquired at the rated (nominal) condition of the prototypical natural circulation BWR, since we will apply this model for the stability experiments at the rated condition and close to it.

Figure 5.1 shows the effect of the AR model order m on the decay ratio and the period ($= 1/f$) at the rated condition with void-reactivity feedback. Since there are two identical channels, a set of time-series data consists of 512 points of the measured inlet velocity at each channel (Ch. 1 and Ch. 2 in Figure 5.1). As shown in Figure 5.1 the period is estimated to be approximately 6 s. The decay ratio reduces significantly when $m = 18$. It is well-known that an insufficient order of the linear predictor results in a lower decay ratio. Van der Hagen *et al.* (1994) found an empirical relation between the necessary model order and the resonance frequency :

$$m \approx \frac{2}{f\Delta t_s}, \quad (5.7)$$

where Δt_s is a sampling time ($= 0.5$ s). In this case, $m \approx 2 / (0.15 \times 0.5) \approx 27$. They also reported that the model order estimated by Equation (5.7) is much larger than those obtained by the AIC. This is because the AIC supplies an optimal model order, which models best the process over the whole frequency range. The decay ratio, on the other hand, is contained in the oscillations around 0.15 Hz, that is, the low-frequency part of the signal. It can be seen from the figure when $24 \leq m \leq 36$, decay ratios for both channels are approximately 0.5 and are in good agreement. In this study, m is therefore set to be 30 which shows a rather good agreement between the channels.

Figure 5.2 shows the effect of the data size (number of data) n on the decay ratio and the resonance frequency at the rated condition with void-reactivity feedback. One can easily

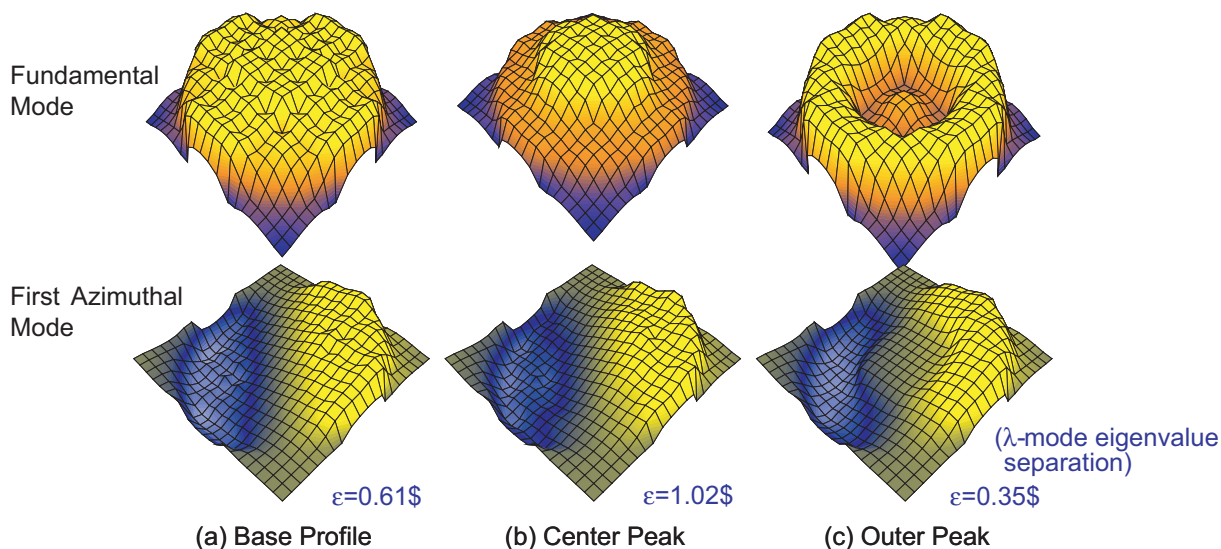


Figure 5.4: Power distributions and their λ -mode eigenvalue separations (ϵ). The upper graphs are for the fundamental mode ($m=0$), while the lower graphs are for the first azimuthal mode ($m=1$). The variation of the power distribution is implemented as the λ -mode eigenvalue separations in the modal-point kinetics.

imagine that an insufficient data size will result in unreliable predictions of the decay ratio and period (Van der Hagen *et al.*, 1994). It is clear from Figure 5.2 that at least 384 points of time-series data are required for an accurate estimation of the decay ratio. Therefore n is set to be 512. The data size is sufficiently large: (1) n is more than seven times larger than AR model order m and (2) the acquired time span (256 s) is more than thirty times longer than the estimated period ($1/f \approx 7$ s). A set of time-series data measured at Ch. 2 will be used for stability estimation because decay ratios for both channels agree well.

In order to demonstrate the validity of the applied AR method, the power spectral density of the reconstructed data is compared with that of the measured (original) data. Figure 5.3 shows the power spectral density of the measured data and reconstructed data from the AR model. The average power spectral density (APSD) was averaged over 4 records of 128 samples each. Because of noise and small number of data, high frequency noise also contributes to the measured data. Nevertheless, the power spectral density of the measured data is accurately reproduced by the reconstructed data at the dominant frequency of 0.15 Hz.

5.3 Regional Stability Estimation with SIRIUS-N Facility

In this section, the stability characteristics of a prototypical natural circulation BWR are investigated in terms of the design parameters such as the power profile, the void reactivity coefficients, core inlet subcooling, and the thermal conductance of the fuel rod. Stability experiments are carried out and decay ratios are estimated by the noise analysis, as described in the previous section. Regional instability is demonstrated to correspond to the least stable mode.

5.3.1 Implemented Power Profile and λ -mode Eigenvalue Separation

The parameters required for the reactor physical model are estimated on the basis of a three-dimensional modified one-group neutron diffusion analysis for the 3.13 GWt prototypical natural-circulation BWR. The reactor is assumed to have been in operation for 24 months (91.8 % usage rate) at 100 % power. Each channel box contains sixty fuel rods with one water rod, which is

Table 5.2: Parameters in Stability Experiment Near Rated Operating Conditions

Parameter	Legend	Unit	Reactor	SIRIUS-N
System Pressure	P_s	MPa	7.07	7.20
Heat Flux at Criticality	q_0''	kW/m ²	685	685
Void Reactivity Coefficient Multiplier	$a_{C\alpha}$	-	1.0	0.0 - 1.5
λ -mode eigenvalue separation	ϵ	\$	0.61	0.00 - 1.83
Fuel Rod Time Constant	τ_f	s	4.7	3.7 - 11.7
Nondimensional Core Inlet Subcooling	N_{sub}	-	0.65	0.65 - 2.37

a so-called $8 \times 8 - 4$ fuel configuration. The average enrichment and burn-up are 3.7 % and 14.4 GWd/t, respectively.

Figure 5.4 illustrates three power distributions with their subcriticalities (λ -mode eigenvalue separations, ϵ). The upper graphs are for the fundamental mode ($m=0$), while the lower graphs are for the first azimuthal mode ($m=1$). These three power distributions are determined to satisfy the safety regulations in terms of the thermal operational restrictions and shut-down margin. The standard power distribution is illustrated in Figure 5.4 (a) with the λ -mode eigenvalue separation of 0.61 \$.

Two additional power distributions are addressed to estimate core-wide and regional stabilities conservatively. Figure 5.4 (b) illustrates a center peak power distribution with a λ -mode eigenvalue separation of 1.02 \$, where the power in the outer channels is suppressed by inserting the control rods, which is a conservative estimate of the core-wide stability. Figure 5.4 (c) illustrates the outer peak power distribution with the λ -mode eigenvalue separation of 0.35 \$, which is a conservative estimate of the regional stability. The variation of the power distribution is implemented as the λ -mode eigenvalue separation in the modal-point kinetics.

5.3.2 Investigation of Rated Operating Conditions

In order to avoid flashing-induced density wave oscillations at relatively low pressures (see Chapter 2) and Type-I density wave oscillations at relatively high pressures (see Chapter 3), the prototypical natural-circulation BWR is started up at a low power density and low subcooling until the pressure reaches 6.8 MPa. During the start-up procedure, the effect of the void-reactivity feedback is negligibly small, since the void fraction in the core is small.

Core-wide and regional stability estimations were conducted for the rated operating conditions when the void fraction is large. During the stability experiments the system pressure and the average heat flux were fixed at rated operating conditions. For the parametric study on the design parameters, core inlet temperature, fuel rod time constant, and λ -mode eigenvalue separation were varied, as tabulated in Table 5.2.

For a conservative evaluation, the flow is classified as unstable, when the standard deviation of the inlet velocity exceeds 2 % of the average in this study, which is the minimum detectable perturbation.

For all parameter ranges listed in Table 5.2, the standard deviation of the inlet velocity is turned out to be smaller than 2% of the average indicating that the flow condition is stable. It can be concluded from the above results and the channel stability investigations (see chapters 2 and 3) that the representative natural-circulation BWR can be started up with a sufficient stability margin.

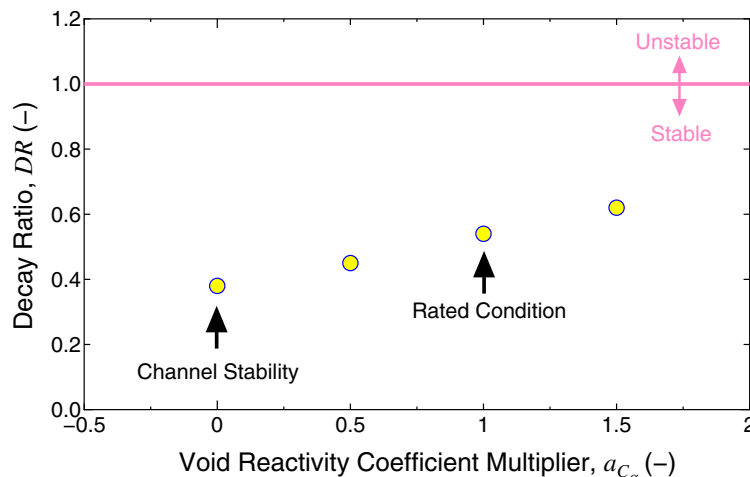


Figure 5.5: Stability effect of void reactivity. The decay ratio for rated operating conditions ($a_{C_{\alpha}} = 1$) is 0.54, which means that the system is sufficiently stable. The decay ratio of the thermal-hydraulic stability without void-reactivity feedback ($a_{C_{\alpha}} = 0$), is 0.38.

5.3.3 Stability Effect of Design Parameters

Core-wide and regional instabilities are not observed at the rated condition of the prototypical natural circulation BWR. In this section, noise analysis was performed for all the stable data to determine core-wide and regional stability features.

Figure 5.5 shows the effect of the void reactivity coefficient on the stability. All experimental conditions are identical as those for rated operating conditions except the void reactivity coefficient. The void reactivity coefficient was multiplied by $a_{C_{\alpha}}$, then used in the experiment for a sensitivity study. As shown in the figure, the decay ratio for rated operating conditions is 0.54, which means that the system is sufficiently stable. The system stabilizes as the absolute value of the void reactivity coefficient becomes smaller (smaller $a_{C_{\alpha}}$). This is because that the gain of the loop transfer function becomes smaller as the absolute value of the void reactivity coefficient diminishes.

When the void reactivity coefficient becomes zero, the power remains constant, even if the void fraction fluctuates. In that case, the decay ratio is referred to as ‘channel stability’. The channel decay ratio is determined to be 0.38 as shown in Figure 5.5.

Figure 5.6 shows the normalized cross correlation function of the inlet velocities of the two channels. The experimental data is obtained for the rated operating condition ($a_{C_{\alpha}} = 1$). The distinct peak of the cross correlation function with a negative value is found when $\tau = 0$ for all experimental parameters in this study, indicating an out-of-phase interaction modes between the two core halves. Therefore, the values of decay ratio and resonance frequency relate to the regional stability rather than the core-wide stability. The decay ratio of the core-wide stability is smaller than that of the regional stability (being 0.54).

Figure 5.7 shows the stability effect of the radial power profile and core size. Plotted λ -mode eigenvalue separation points with arrows indicate the power profiles as a result of three-dimensional steady-state reactor analysis as depicted in Figure 5.4. λ -mode eigenvalue separations of the other points are 0, 2, and 3 times as large as that for the base profile. As shown in Figure 5.7, the system destabilizes when the outer part of the power is relatively higher (smaller λ -mode eigenvalue separation). This is because the first azimuthal mode becomes dominant, since the out-of-phase thermal-hydraulic mode is more unstable than the in-phase mode at the rated operating condition.

Figure 5.8 shows the stability effect of the fuel rod time constant. The decay ratio reaches a

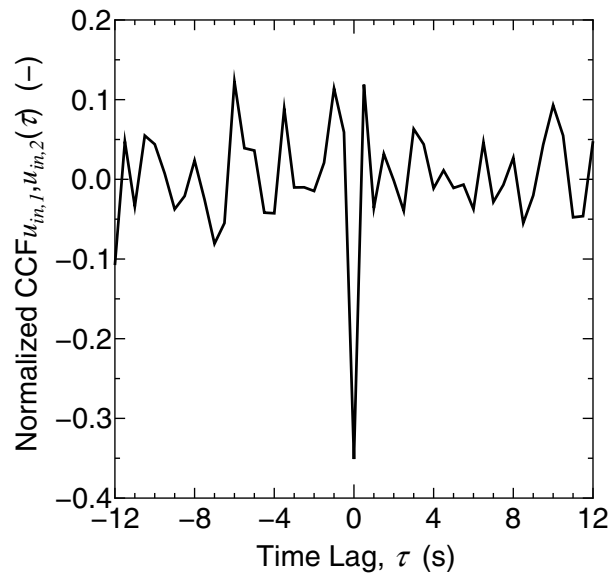


Figure 5.6: Interaction mode between half-cores. The distinct peak of the cross correlation function with a negative value is found at $\tau = 0$, indicating an out-of-phase interaction mode between the two core halves. Therefore, the values of decay ratio and resonance frequency relate to regional stability.

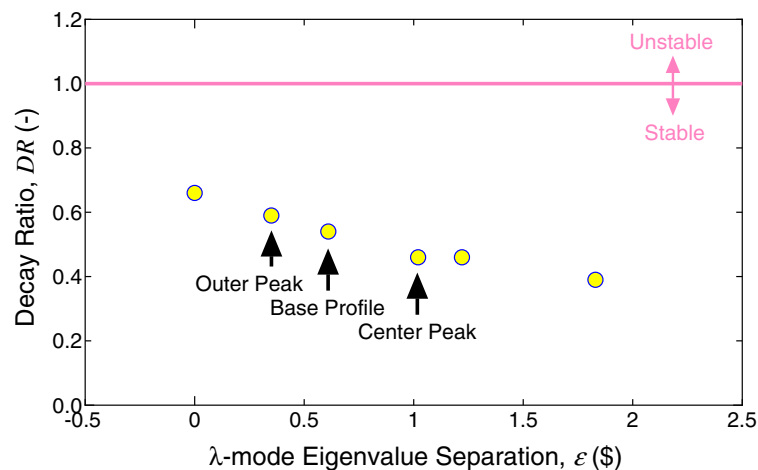


Figure 5.7: The system destabilizes when outer part of the power is relatively higher (smaller λ -mode eigenvalue separation).

local maximum when the fuel rod time constant is approximately 6.7 s. This time constant coincides with the time required for bubbles to travel through the chimney region as we discussed in Chapter 3 (Van Bragt and Van der Hagen, 1998b). Therefore, the system approaches the least stable condition when the oscillation period of thermal-hydraulic stability agrees with the phase lag of the void-reactivity feedback with a negative coefficient.

Figure 5.9 shows the stability effect of core inlet subcooling in terms of power profiles. As shown in the figure, the decay ratio becomes higher with increasing core inlet subcooling. This is mainly because the amplitude of the driving force of natural circulation in response to the flow rate becomes larger with increasing core inlet subcooling. For a fixed core inlet subcooling, the system seems to be more stable with larger λ -mode eigenvalue separation, though the difference is relatively small. The difference of decay ratio diminished with higher core inlet subcooling.

Finally, it can be concluded from the results above and the thermal-hydraulic stability investigations described in Chapters 2 and 3, that the prototypical natural-circulation BWR can

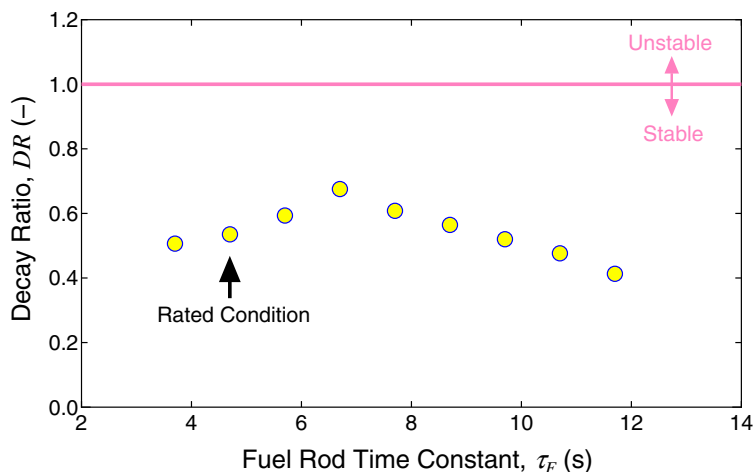


Figure 5.8: Stability effect of the fuel rod time constant. The decay ratio reaches a local maximum when the fuel rod time constant is approximately 6.7 s. Therefore, the system approaches the least stable condition when the oscillation period of thermal-hydraulic stability agrees with the phase lag of the void-reactivity feedback with a negative coefficient.

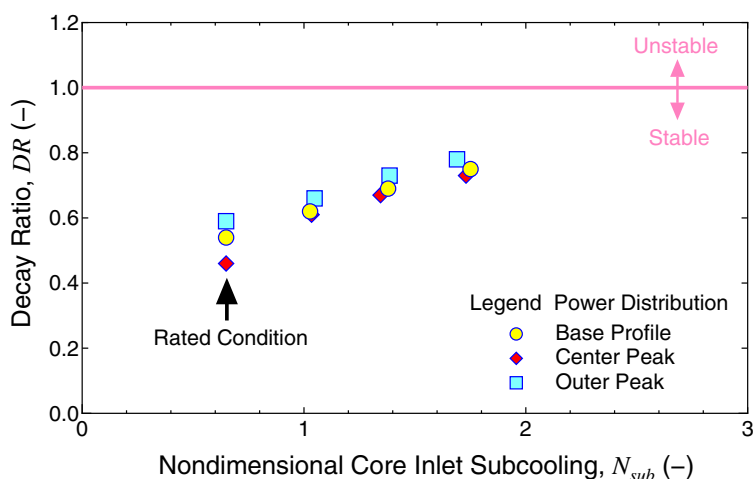


Figure 5.9: Stability effect of core inlet subcooling. The system becomes less stable with increasing core inlet subcooling.

be started up with a sufficient stability margin.

5.3.4 Stability Identification by Limit Cycle Oscillations

In order to identify the least stable mode (the core-wide or the regional mode) and the characteristics of limit cycle oscillations, experiments were conducted under hypothetical and least stable conditions. The two differences from the rated conditions are: (1) the void reactivity coefficient was set to be twice as large as that under rated operating conditions, (2) the core inlet subcooling is kept at the maximum value tabulated in Table 5.2, being $N_{sub} = 2.35$. Type-I density wave oscillations occur with the higher inlet subcooling as we discussed in Chapter 3 (also see Figure 3.3). The system pressure and the heat flux at criticality were the same as those under rated operating conditions.

Figure 5.10 shows the stability map for the λ -mode eigenvalue separation and the fuel rod time constant. The λ -mode eigenvalue separation is related to the power distribution illustrated in Figure 5.4. Regional instability was observed within a certain range of the fuel rod time constant. When the heat flux was kept constant, which means no void reactivity feedback, out-

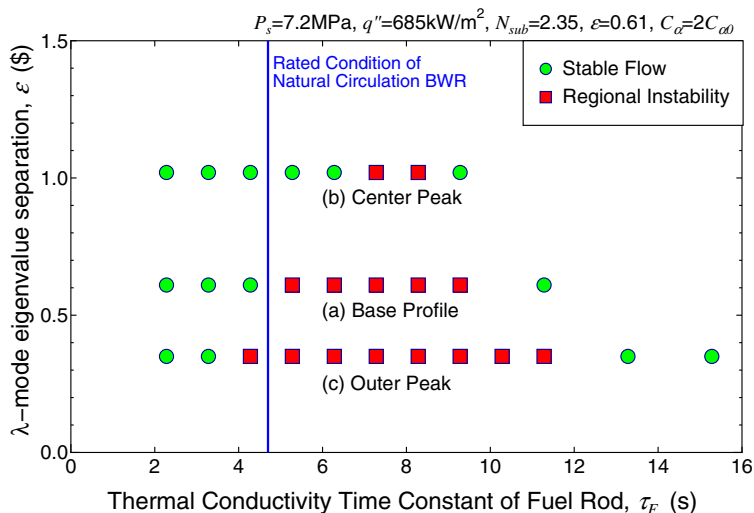


Figure 5.10: Effect of power distribution on stability. Regional instability was observed within a certain range of the fuel rod time constant. The unstable region enlarges with decreasing λ -mode eigenvalue separation, since the feedback gain of the first azimuthal mode becomes larger resulting in out-of-phase oscillations.

of-phase oscillations were observed when $N_{sub} > 4$. Regional oscillations seem to occur due to the least stable mode of thermal-hydraulics (Type-I density wave oscillations). As shown in Figure 5.10, the unstable region enlarges with decreasing λ -mode eigenvalue separation, since the feedback gain of the first azimuthal mode becomes larger resulting in out-of-phase oscillations.

In order to investigate the characteristics of the regional instability, we demonstrate limit cycle oscillations of the regional instability with the SIRIUS-N facility. Figure 5.11 shows waveforms under stable flow with a fuel time constant τ_f of 2.3 s and regional instability ($\tau_f = 8.3$ s). Each graph in this figure shows the channel inlet velocity, the thermal power of the channel, the void fraction at chimney exit and middle, and the core void fraction. Compared to stable flow, the amplitudes of the regional instability increased gradually with time after the artificial neutronic feedback was activated (at $t = 0$ s). After approximately 170 s, the oscillations attained stable limit cycles.

The phase of the void fraction in the core section shifted to that of the thermal power by 180 degrees, which clearly indicates the characteristics of regional instability. The void wave in the core section was transferred to the chimney exit. As we discussed in Sections 3.2.1 and 3.2.1 (see Figures 3.2 and 3.9), the void fraction in the chimney was synchronized with the channel inlet velocity, since vapor bubbles in the chimney drive the circulation flow in the natural circulation BWR.

As investigated for relatively high system pressures in Section 3.2.2 (see Figure 3.5), the oscillation period of Type-I density wave oscillations is one to two times the time required for vapor bubbles to travel through the chimney region. According to the waveforms in Figure 5.11, the oscillation period is approximately 7 s, which is 1.8 times the time required for vapor bubbles to travel through the chimney region. When the oscillation period of Type-I density wave oscillations coincides with the fuel rod time constant (being 7 s), the flow becomes least stable as shown in Figure 5.10.

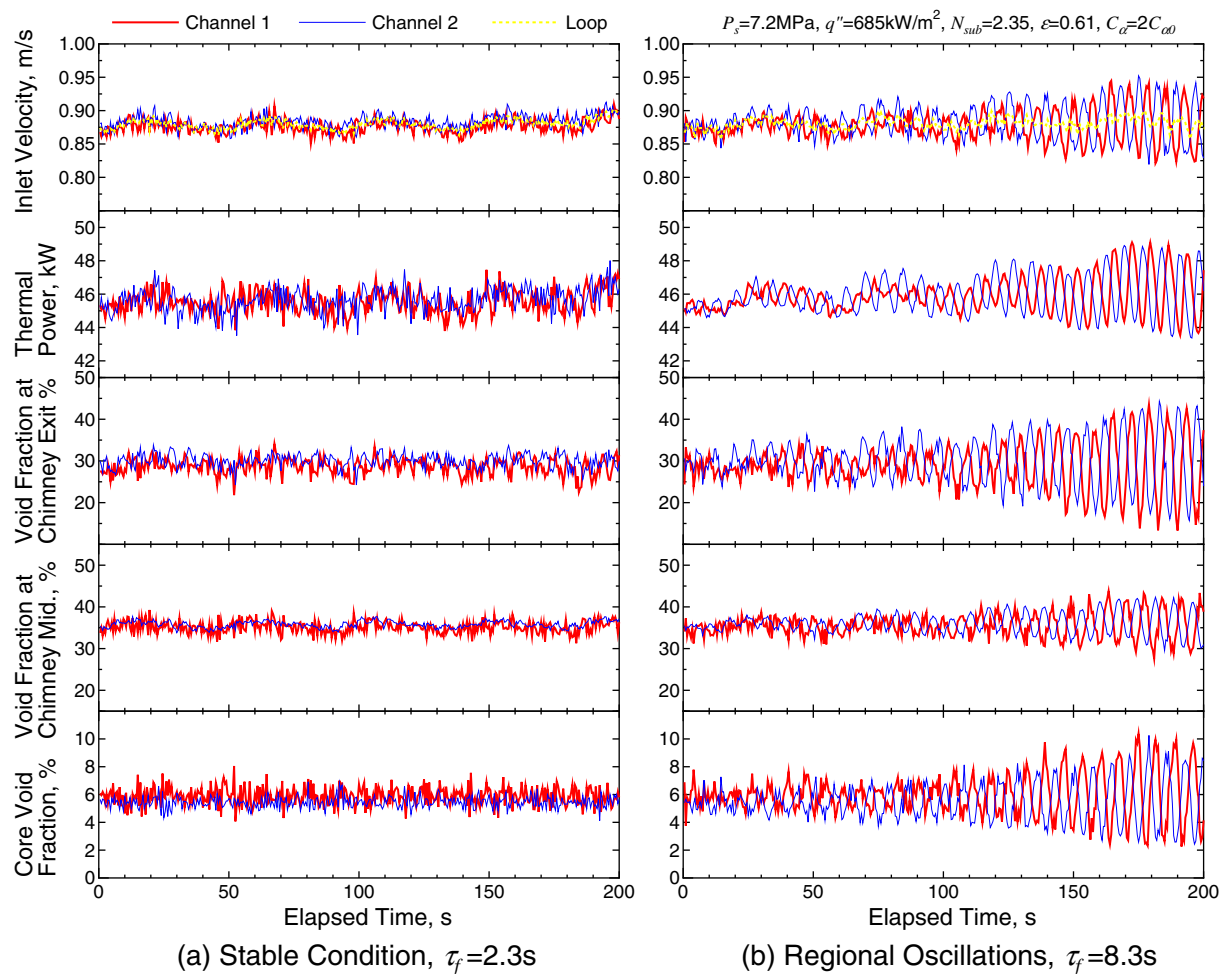


Figure 5.11: Time traces of signals under stable conditions ($\tau_f = 2.3$ s) and regional oscillations ($\tau_f = 8.3$ s). The regional oscillations are clearly demonstrated when the artificial neutronic feedback is activated (at $t = 0$ s), and the amplitudes increases gradually with time. After approximately 170 s, the oscillations attained stable limit cycles. The phase of the void fraction in the core section shifts to that of the thermal power by 180 degrees, which clearly indicates the characteristics of regional instability.

5.4 Conclusions

- In order to estimate decay ratios, an auto-regressive method has been applied for time series data of the core inlet flow rate. The reconstructed power spectral density of the inlet flow rate demonstrates the validity of the method.
- Experiments were conducted with the SIRIUS-N facility for the rated operating condition of a 3.13 GWt natural circulation BWR. Channel and regional stability decay ratios were determined to be 0.38 and 0.54, respectively, which indicates a sufficient margin to both instabilities at the rated condition.
- Experiments were extended to evaluate the stability sensitivity of the design parameters. The system stabilizes with decreasing λ -mode eigenvalue separation, inlet subcooling, and the void reactivity coefficients. It was found that the system approaches the least stable condition when the fuel rod time constant is approximately 6.7 s. This is because the oscillation period of thermal-hydraulic stability agrees with the phase lag of the void-reactivity feedback with a negative coefficient.

- The regional instability was clearly demonstrated with the SIRIUS-N facility for hypothetical conditions (double-void reactivity coefficient and inlet core subcooling increased by a factor of 3.6). When the artificial void-reactivity system is activated, the amplitude of oscillations becomes larger. After 170 s, the oscillations reaches to the limit cycle. The phase of the void fraction in the core section shifts to that of the thermal power by 180 degrees. The void fraction in the chimney is synchronized with the channel inlet velocity. These facts clearly indicate the characteristics of regional instability.

Chapter 6

Forced Circulation BWR Core-Wide and Regional Stabilities

Abstract

The method of implementing artificial void-reactivity feedback that is described in Chapter 4 is now used for studying core-wide and regional stability estimation. We used the SIRIUS-F facility for determination of the channel, core-wide, and regional stabilities of the ABWR, which is a forced circulation BWR.

The core-wide and the regional stability experiments were conducted at the maximum power points along the minimum pump speed line and the natural circulation line of the ABWR. The regional stability is clearly demonstrated, since the distinct peak of the cross-correlation function between the two core halves with a negative value was found at $\tau = 0$. The decay ratios and resonance frequencies from the SIRIUS-F facility are in good agreement with those from the design analysis code, ODYSY. The design analysis code, ODYSY is validated with the SIRIUS-F experimental data.

The experimental data from the SIRIUS-F facility suggests that the ABWR will not encounter instabilities even if the selected control rods run in malfunctioning after a pump trip event.

6.1 Introduction

In historical perspective, stability has been the main concern in the development stage of BWRs. The boiling two-phase flow in the core may become less stable because of the time lag between vapor generation and pressure loss perturbation (the void sweep phenomenon). Furthermore, void-reactivity feedback may make the system less stable. These two issues are of practical importance for designing and operating BWRs.

Three instability modes are related to forced circulation BWRs: (1) channel instability, (2) core-wide instability, and (3) regional instability. Channel stability is a thermal-hydraulic phenomenon, known as density-wave oscillations. In estimating the channel stability, the void-reactivity feedback is not taken into account. Core-wide and regional instabilities deal with thermal-hydraulics coupled with neutronics (void-reactivity feedback). In core-wide stability, neutron flux perturbations are in-phase at all the locations in the core. For instance, the core-wide oscillations were observed at the LaSalle 2 plant in the United States (NRC, 1988). The observed decay ratio was reported to be higher than that calculated by the design analysis.

In regional stability, the neutron flux on one side of the core fluctuates in the opposite phase

to that on the other side. Regional oscillations were, for instance, observed at the Caorso plant in Italy (Gialdi *et al.*, 1985). In all observed regional instabilities in BWRs, the oscillation mode was the first azimuthal mode (D'Auria *et al.*, 1997). It is well established that as the core size increases, the nuclear coupling between different parts of the core becomes weaker and the core becomes more susceptible to regional oscillations. Therefore, regional stability considerations can limit the maximum feasible core size and power ratings.

In estimating core-wide and regional stabilities, linear stability analysis is a useful tool and widely used for licensing analysis. Linear stability analysis can predict the decay ratio (or the damping coefficient) as a stability index. Most of the linear stability analysis codes were validated with plant operation data of BWRs. Although experimental investigations were conducted with BWR plants, scattered data from those instability events could never reveal the effects of design parameters systematically, such as core thermal power, flow rate, fuel type, void-reactivity feedback coefficient, and so on. No experimental facility is yet available to simulate regional stability. It is of scientific importance to understand physical phenomena. Furthermore, in order to increase in-depth knowledge of the stability of a BWR, it is of practical importance to validate design analyses with experimental data.

This chapter elaborates on the channel, core-wide, and regional stabilities of forced circulation BWRs. It describes the method developed to implement artificial void-reactivity feedback for forced circulation BWRs, which differs from that of natural circulation BWRs. The channel, core-wide, and regional stability experiments were conducted with the SIRIUS-F¹ facility, which simulates the behavior of the Advanced Boiling Water Reactor (ABWR). The results obtained were compared with the licensing analysis code, ODYSY, for validation.

6.2 SIRIUS-F Experimental Facility

The SIRIUS-F facility is a full-height facility for simulating core-wide and regional stabilities of the ABWR. In this section, features of the SIRIUS-F facility and the experimental procedure are described.

6.2.1 Design Concept

The SIRIUS-F facility is slightly different from the SIRIUS-N facility for simulating core-wide and regional stabilities of the ABWR. The design concept of the SIRIUS-F facility, as well as the difference between the SIRIUS-F and the SIRIUS-N facilities are briefly summarized in the following context.

Artificial void-reactivity feedback system Void-reactivity feedback is a crucial phenomenon in core-wide and regional instabilities. In order to simulate void-reactivity feedback, which does not exist in out-of-pile facilities, void fractions are measured by differential pressure measurement systems (DPMS) over the core sections. The measured void fractions are used as input for real-time simulations of void-reactivity feedback and modal point kinetics. The power supplies are controlled in accordance with the simulation output. For further description, see Section 4.2.

Feedback loop implementation and system integration As shown in Figure 4.3, the measurement and control systems of the SIRIUS-F facility are the same as those of the

¹SIRIUS-F is an abbreviation of *S*imulated *R*eactivity feedback *I*mplemented into thermal-hydraUlic *S*tability loop for *F*orced circulation BWR

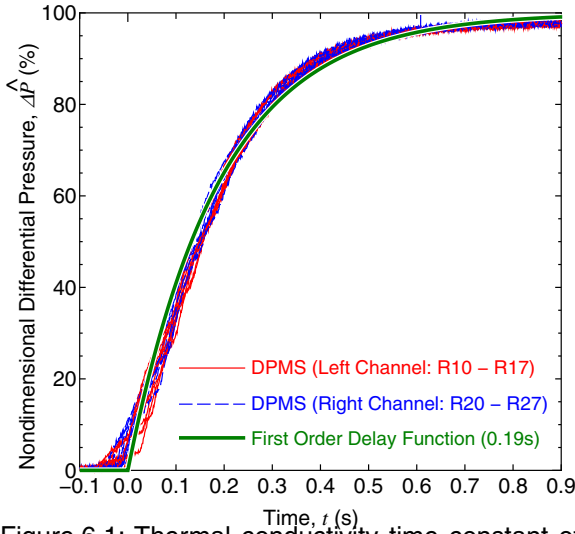


Figure 6.1: Thermal conductivity time constant of heater rod. The indicial response curve followed the first-order delay function of 1.1 s.

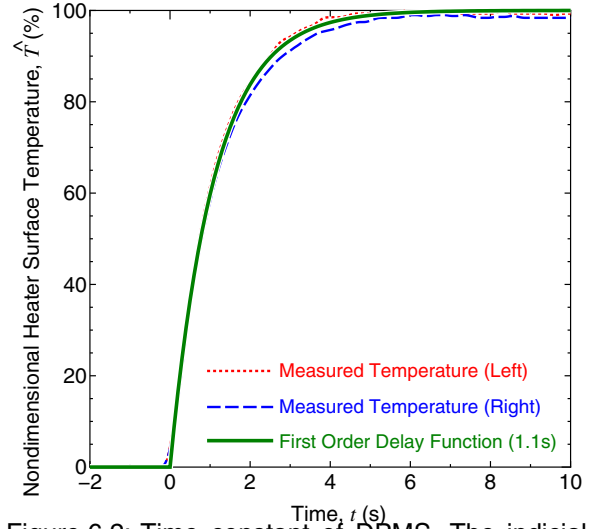


Figure 6.2: Time constant of DPMS. The indicial response curve followed the first-order delay function of 0.19 s.

SIRIUS-N facility, except the number of measurement points is nearly doubled. The computer cluster consists of five computers (SIRIUS-PC1 to -PC5). Each computer has a 100Base-TX NIC and is connected with other computers via a switching hub using TCP/IP protocol. The only difference is the sampling frequency of the SIRIUS-PC2 measurement system. SIRIUS-PC2 acquires whole-plant conditions at 10 Hz (*cf.* 2 Hz for the SIRIUS-N facility). This is because the resonance frequency of the ABWR (0.3 Hz - 0.5 Hz) is higher than that of the prototypical natural circulation BWR (0.004 Hz - 0.15 Hz). For a detailed description of the measurement and control system, refer to Section 4.3.

Formulation of real-time analysis In order to simulate void-reactivity feedback, real-time analysis is conducted for thermal-hydraulics, neutronics, and thermal conduction. The void fraction in the core section is calculated from the measured differential pressure over the corresponding simulated fuel channel section, together with mass flux and local temperatures as described in Section 2.2.3. In the SIRIUS-F facility, seven sets of the DPMS are arrayed in the axial direction for acquiring the void fraction profile transients. In the SIRIUS-N facility, only one set of the DPMS in each channel is used, since the phase lag of the void fraction is relatively small. The seven measured sets of void fractions are used for void-reactivity estimation as follows (*cf.* equations (4.5) and (4.6) for the SIRIUS-N facility):

$$\rho_{00}^F(t) = \rho_{11}^F(t) = \frac{\sum_{i=1}^7 [\phi_i^2 \{C_\alpha(\alpha_{ch1,i})\delta\alpha_{ch1,i} + C_\alpha(\alpha_{ch2,i})\delta\alpha_{ch2,i}\}]}{\sum_{i=1}^7 \phi_i^2}, \quad (6.1)$$

$$\rho_{01}^F(t) = \rho_{10}^F(t) = \frac{\sum_{i=1}^7 [\phi_i^2 \{C_\alpha(\alpha_{ch1,i})\delta\alpha_{ch1,i} - C_\alpha(\alpha_{ch2,i})\delta\alpha_{ch2,i}\}]}{\sum_{i=1}^7 \phi_i^2}, \quad (6.2)$$

where i stands for each DPMS measurement region. The void-reactivity feedback to volumetric heat generation is analyzed by reactor neutronics, including eigenvalue separation of the higher-harmonic neutronic mode. In this study, formulations derived by Hashimoto (1993) were applied as summarized in Section 4.4. The heat generated in the fuel was

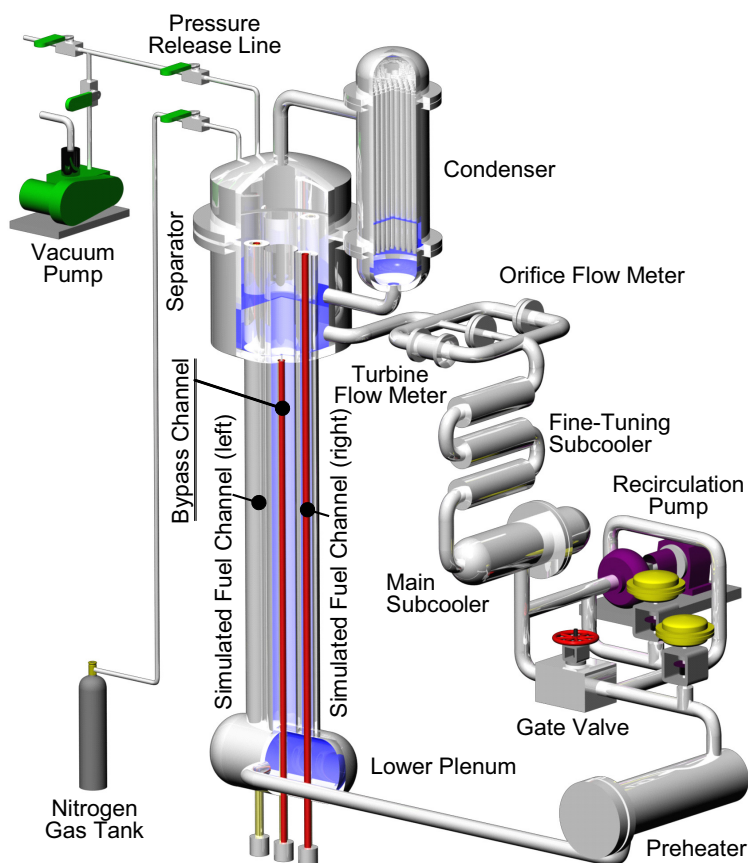


Figure 6.3: Schematic of thermal-hydraulic loop of SIRIUS-F facility. The SIRIUS-F is a full-height facility used to simulate the channel, core-wide, and regional stabilities of the ABWR.

transferred to the coolant with a certain delay time. This delay, caused by thermal conduction in the fuel rod, can be formulated as point kinetics. Detailed formulation is described in Section 4.4.3.

Fuel rod time constant A verification test was conducted to obtain the fuel rod time constant of the heater rods used in the SIRIUS-F facility. Temperature response was acquired from thermocouples embedded in the heater rod surface. Figure 6.1 shows a typical response of heater surface temperature to a stepwise increase in heater power. The temperature response curves closely agree with a first-order time delay function of 1.1 s, as shown in the figure. A time constant of 1.1 s was therefore assumed (*cf.* 0.9 s for the SIRIUS-N facility, the difference being caused by a different composition of the electrical insulation material in the heater rod).

Time constant of measurement system The DPMS has a certain delay in its response to differential pressure change. A higher-response DPMS was developed for the SIRIUS-F facility. Figure 6.2 shows the response of the DPMS to a stepwise increase in differential pressure. All sixteen curves follow a first-order delay function of 0.19 s (*cf.* 0.38 s for the SIRIUS-N facility), as the figure illustrates. Time delays of 0.19 s (DPMS) and 1.1 s (heater rod) were added to the fuel rod time constant in the real-time simulation. Therefore, the fuel rod time constant indicated as an experimental parameter, τ_f , includes these time delays.

Stability estimation method based on noise analysis The number of the time-series data (the velocity at the channel inlet) was determined to be 2048 (*cf.* 512 for the SIRIUS-N facil-

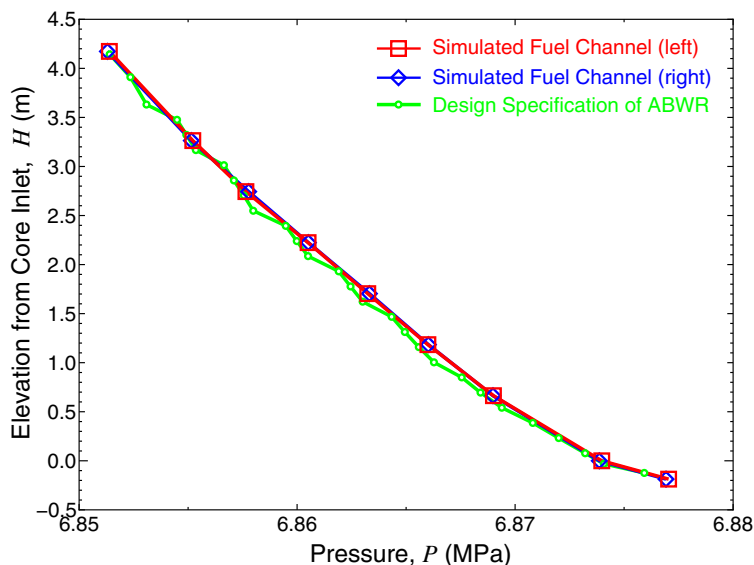


Figure 6.4: Axial pressure profile measured at SIRIUS-F facility and analyzed on the basis of the ABWR design analysis code. The measured pressure profiles agree well with those of the ABWR, as local pressure losses, such as tie-plates and orifices, are accurately simulated in the SIRIUS-F facility.

ity) on the basis of a parametric study. A detailed explanation is described in Section 5.2.

6.2.2 Boiling Two-Phase Flow Loop

Figure 6.3 is a schematic of the thermal-hydraulic loop of the SIRIUS-F facility. The thermal-hydraulic loop consists of a lower plenum, two simulated fuel channels, a bypass, separator (upper plenum), downcomer, subcooler, recirculation pump, and preheater. Unlike the SIRIUS-N facility, there is no chimney present in this loop. A heater pin is installed in each simulated fuel channel concentrically. The heated length, l_c , is 3708 mm, which is identical to the fuel height in the ABWR. The SIRIUS-F facility can be operated up to 9 MPa. The water working fluid is passed through an ion exchange resin.

Because of the importance of the dimensions and local pressure losses of orifices and tie plates in boiling two-phase flow phenomena, the seven orifices and two tie plates were inserted at the same elevation, having the same local pressure loss coefficients as commercial fuel, called STEP-III (9×9 fuel) Type-A. Local pressure loss coefficients of these orifices and tie plates were determined by performing a single-phase forced circulation experiment at various flow rates.

Figure 6.4 shows the axial pressure profile measured at the SIRIUS-F facility and analyzed on the basis of the design analysis code for the ABWR. Eight differential pressure measurement systems were installed in each simulated fuel channel. Each differential pressure measurement region includes one local pressure loss location (lower tie plate and seven spacers) in the middle. The connecting pipes of DPMS are attached at more than 260 mm away from the spacers not to acquire pressure perturbations. As shown in the figure, the axial pressure distribution of the boiling two-phase flow measured at the SIRIUS-F facility agrees well with that analyzed on the basis of the design analysis code for the ABWR.

Eight Type-K thermocouples (0.5-mm OD) were embedded in, and silver brazed to the surface of the sheath heater rod. The flow rate was measured by an orifice flowmeter attached to the downcomer. System pressure, P_s , refers to the pressure in the separator dome.

Decay ratios and resonances frequency were estimated with the use of noise analysis (see Section 5.2). Artificial void-reactivity feedback control was initiated after the thermal-hydraulic conditions (subcooling and flow rate at the channel inlet, system pressure, and channel heat flux) were steady at the specified values. These boundary conditions can be maintained at the specified value even when instabilities occur within a certain amplitude of the limit cycles, since vapor volume in the separator and volume of the preheater are sufficiently large.

6.2.3 Experimental Procedure

Experiments were conducted according to the following procedure:

1. De-aerate the thermal-hydraulic loop.
2. Heat the simulated fuel channels and bypass channel to induce a boiling natural circulation flow.
3. Start the recirculation pump when the system pressure is high enough to protect the pump from cavitation damage.
4. Pressurize the thermal-hydraulic loop at the specified system pressure by controlling heater outputs and condenser performance automatically.
5. Maintain the channel inlet temperatures, heat fluxes, and channel inlet flow rate at the specified value by changing performance of the subcoolers and the preheater.
6. After steady-state conditions are confirmed in boiling two-phase flow, initiate the artificial void-reactivity feedback system with the specified reactor physics constants and fuel rod time constants.
7. Acquire experimental data for four minutes for the noise analysis to determine the decay ratio and the resonance frequency.
8. Deactivate the void-reactivity feedback system. Wait until the heat flux reaches a constant value.
9. After steady-state conditions are confirmed in boiling two-phase flow, repeat the experiments using the next set of boundary conditions, following the same procedure (6).

6.3 Description of Design Analysis Code

In order to validate a design analysis code, the experimental results of channel, core-wide, and regional stabilities are compared with computational results. The ODYSY code is selected as the design analysis code, since the code is well-established and widely used for the licensing of forced circulation BWRs. The ODYSY code is a linear stability analysis code. It belongs to the Global Nuclear Fuel - Japan (GNF-J) Company.

ODYSY incorporates four models to describe BWR dynamics related to channel, core-wide, and regional stabilities. Figure 6.5 illustrates the scope of the models and the relations between the models. Brief explanations of these four models are described in the following. For more detailed explanations, refer to the reference (Shiralkar, 1997).

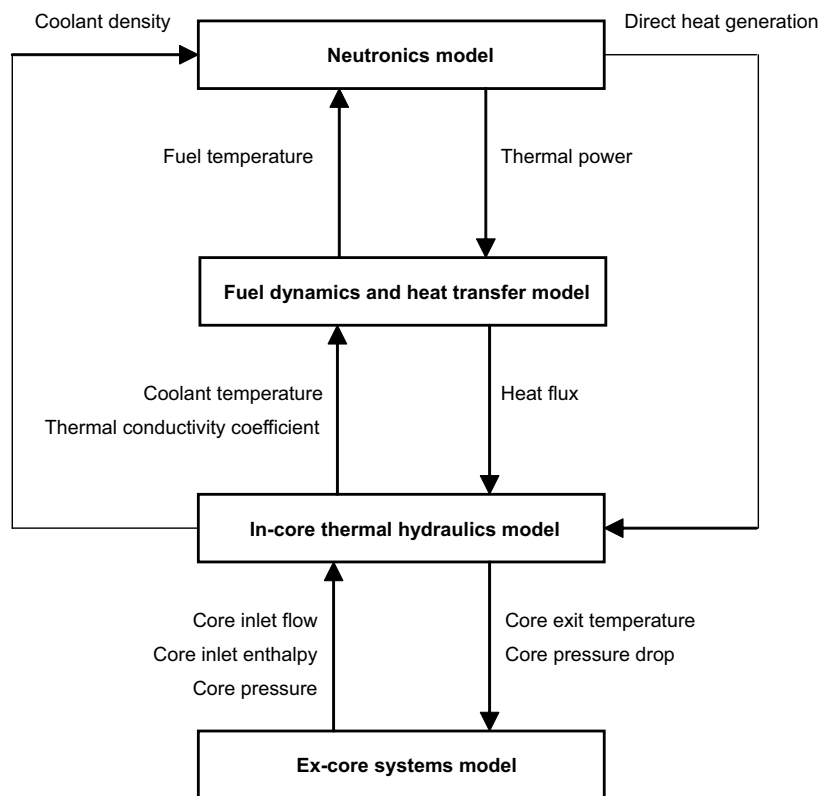


Figure 6.5: Relationships among Models in Analysis

In-core Thermal-hydraulics model The in-core thermal-hydraulics model describes parallel channels of one-dimensional, steam-water two-phase flow. The model consists of five constitutive equations: two mass, one momentum, and two energy equations. The phasic velocity is calculated on the basis of a drift flux model.

Fuel dynamics and heat transfer model The fuel dynamics and heat transfer model describes thermal conduction in the fuel pellet and fuel cladding, and the gap conductance between the fuel pellet and the fuel cladding. The constitutive equations are solved only in the radial direction because heat transfer rate in other directions is small. The material properties and gap conductance are given as functions of temperature.

Neutronics model The neutronics model describes the modal point neutron kinetics. The neutron flux modes considered are the fundamental and the first azimuthal modes. The formulations are almost the same as those implemented in the SIRIUS-F facility (see Section 4.4.2). The two major differences are: (1) this model is based on six delayed neutron groups, whereas the real-time simulation implemented in the SIRIUS-F facility is based on one delayed neutron group, and (2) the design analysis code ODYSY employs linearized equations, whereas nonlinear terms are solved in the real-time simulation implemented in the SIRIUS-F facility. Those differences may not affect the core-wide and regional stabilities within the present experimental parameter ranges (under such stable conditions).

Ex-core systems model The external core systems model describes the thermal-hydraulics in the specific components such as upper plenum, separator, reactor vessel, recirculation system, and lower plenum of BWRs. The mass, momentum, and energy balances are solved in the same manner as the in-core thermal-hydraulics model.

Table 6.1: Specifications of Design Analysis Code

Model	Descriptions
Neutronics	<ul style="list-style-type: none"> - Point neutron kinetics with six delayed neutron groups - Neutron flux transfer functions for fundamental and higher mode - Higher mode transfer function calculated from the higher mode subcriticality obtained by a 3D-core simulator code - Transfer functions of fundamental and higher mode corresponding to core-wide and regional stabilities respectively
Fuel dynamics	<ul style="list-style-type: none"> - 1-D radial thermal conduction - Radial variation of power generation in pellet - Axially varying power generation rate - Temperature dependent thermal properties for cladding and fuel - Gap conductance with axial and radial distributions
Thermal-hydraulics	<ul style="list-style-type: none"> - 1-D axial boiling two-phase flow - Five equation drift flux model (two mass, two energy, and single momentum equations) - In-channel and bypass flow paths - Heat transfer coefficients for single-phase liquid, subcooled boiling, boiling two-phase flows - Best estimate thermal-hydraulic correlations - Plant-specific models describing ex-core systems

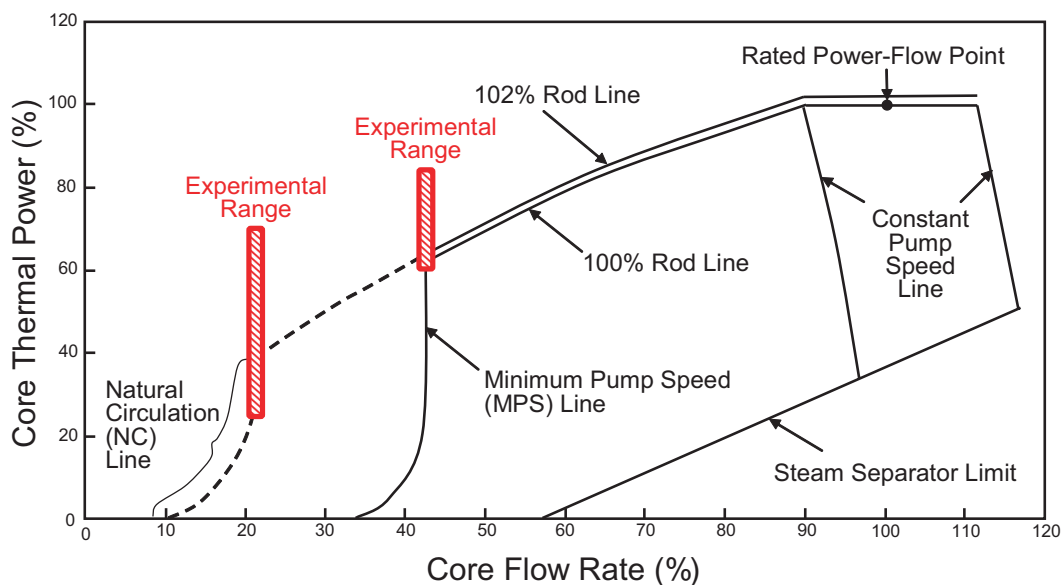


Figure 6.6: ABWR Power-Flow Operating Map and SIRIUS-F Experimental Range

A set of equations is perturbed around a given operating condition and linearized to obtain a set of Laplace transformed equations. Decay ratios and resonance frequencies are calculated by these Laplace transformed equations. The analytical models and code specifications are shown in Table 6.1. More detailed model descriptions, code specifications, and qualifications are described in references (Shiralkar, 1997; Hitachi, Ltd., 1998; Toshiba Co., 1998).

6.4 Experimental and Analytical Parameters

In general, a forced circulation BWR is in its least-stable condition when the power-to-flow ratio is high. The ABWR plant was selected as the target plant for stability investigation, because

Table 6.2: Input Parameters of Design Analysis Code and Experiments

Parameters	Value
Rated thermal Power	3926 MWt / 872 / 74 × 2
Rated core flow	145000 kg/s / 872 / 74 × 2
Fuel	
- Type	STEP-III (9×9 fuel) Type-A
- Active fuel length	3708 mm
Recirculation pump	
- Type	Internal pump
- Number	10
Orifice loss coefficient	40K FABLE
Spacer	Ferrule type
Void reactivity coefficient	0.059 \$ at 40 % void fraction
Total β	0.0053
Gap conductance	8520 W/m ² K
Radial power distribution	1.0
Axial power distribution	1.70N3
λ -mode eigenvalue separation	
- Forced circulation	0.00371
- Natural circulation	0.00318
Target operating conditions	Minimum pump speed line Natural circulation line
Code name	ODYSY05

its power-to-flow ratio is the highest among all commercial BWRs, when the plant is operated under natural circulation condition.

Figure 6.6 shows an ABWR power-flow operating map. Hereafter, the power and flow are expressed in %, being the ratio to the rated condition. The experimental ranges in this study are shown in the figure with two hatched rectangles: (1) the minimum pump speed (MPS) line including the maximum power point, and (2) the natural circulation (NC) line including the maximum power point. The term ‘minimum pump speed’ refers to the state in which all the internal pumps are operated at the lowest allowable pump speed. The term ‘natural circulation’ refers to the state in which all the internal pumps are out of operation (rotors are fixed).

When the operating condition falls in the high power/flow region after e.g. a pump trip event in the ABWR, a predetermined set of control rods is inserted into the core to suppress heat generation (SCRRI: Selected Control Rods Run-In). In the present study, core thermal power was assumed to remain the same because of a malfunctioning of the SCRRI for a conservative estimate of the stability.

Linear stability analysis with the ODYSY code is performed ² for the same conditions as the experimental ones. Table 6.2 shows analytical conditions in detail. The target fuel type and axial power profile are so-called STEP-III Type-A and bottom skewed profile (1.70N3), which are usually applied for a conservative evaluation in a licensing analysis. In the design of STEP-III Type-A fuel, some fuel rods are shorter than others, namely the part length rods (PLRs). The idea behind the PLRs is to enhance the thermal-hydraulic stability by decreasing the pressure drop in two-phase region. The PLRs are implemented in the SIRIUS-F facility and in the analysis by changing the flow area at the edge of the PLR.

A three-dimensional modified one-group neutron diffusion analysis was carried out to determine reactor physical parameters. The λ -mode eigenvalue separation was set at 0.00371 on

²The calculation has been performed by Global Nuclear Fuel - Japan (GNF-J)

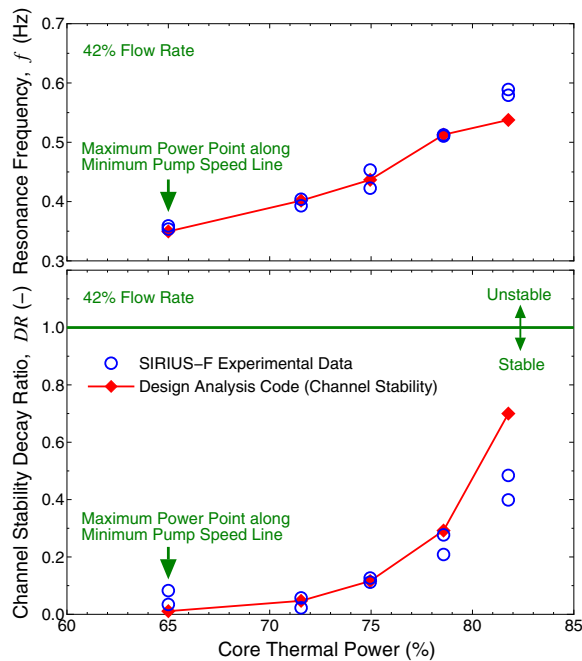


Figure 6.7: Channel stability on the minimum pump speed line. The resonance frequencies obtained in the linear stability analysis agree well with those obtained in the SIRIUS-F facility. Although the power increases further to 82 %, the channel decay ratio remains lower than 0.8.

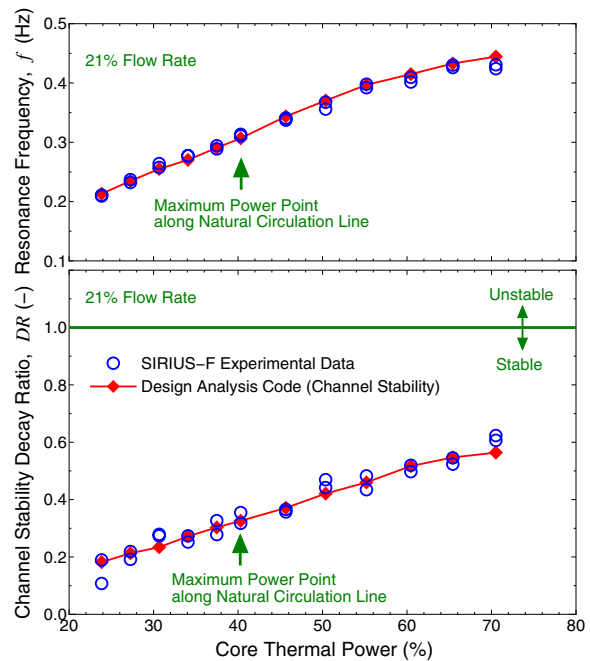


Figure 6.8: Channel stability on the natural circulation line. The experimental and analytical decay ratios are in close agreement. As the power increases from 24 % to 71 %, the decay ratio increases monotonically. Even at 71 % power, the decay ratio is lower than 0.7.

the minimum pump speed line and at 0.00318 on the natural circulation line, for a conservative estimate (the largest value under all conditions that meets the design criteria). The fuel time constant used was 3.5 s, which is the representative value for a licensing analysis.

6.5 Results on Channel Stability

At first, in order to investigate thermal-hydraulic characteristics, the channel stability experiment was conducted on the minimum pump speed and natural circulation lines without void-reactivity feedback. Consequently, the heat flux was constant with time. Experiments were repeated twice to test reproducibility.

6.5.1 Minimum Pump Speed Line

Figure 6.7 shows the experimental and analytical channel stability results on the minimum pump speed line. The upper figure shows the resonance frequency. Resonance frequencies obtained by linear stability analysis agree well with those obtained using the SIRIUS-F facility. The resonance frequency increases monotonically with increasing power, because the transit time of the channel becomes shorter with increasing power.

The lower figure shows the decay ratio as a function of core thermal power. It is found that the experimentally-obtained decay ratio matches the value obtained from the design analysis code for the power between 71 % - 79 %. The analytical and experimental decay ratios at

maximum power (65 % of the rated power) on the minimum pump speed line are lower than 0.1, indicating that channel stability is sufficiently high. The experimental decay ratio at the maximum power is higher than the analytical value. This is caused by the difficulty to estimate such a low decay ratio with noisy signals experimentally obtained by the applied AR method. At 82 % power, the experimental decay ratio is lower than the analytical value. At the same point, the experimental resonance frequency is higher by 0.05 Hz than the analytical value. Although the cause of the discrepancy is not clear, the convergency of the analysis could contribute to the discrepancy. As the power increases on the minimum pump speed line, both experimentally and numerically obtained decay ratios increases monotonically. Although the power increased further up to 82 %, the channel decay ratio is still lower than 0.8 (which is the design criterion in Japan).

6.5.2 Natural Circulation Line

Figure 6.8 shows the experimental and analytical channel stability results on the natural circulation line. Resonance frequencies obtained by linear stability analysis agrees well with those obtained using the SIRIUS-F facility. At the maximum power point (40 % of the rated power) on the natural circulation line, the channel stability decay ratio is approximately 0.3 in both analytical and experimental results. As the power increases from 24 % to 71 %, the decay ratio increases monotonically. Even at 71 % power, the decay ratio is lower than 0.7 (which is lower than the design criterion in Japan ($DR < 0.8$)).

These channel stability results suggest that the ABWR is thermal-hydraulically stable enough to meet the design criteria. In addition, the linear stability analysis was validated with the SIRIUS-F facility for the channel stability.

6.6 Results on Core-Wide and Regional Stability

The reactor cannot operate without void-reactivity feedback. Furthermore, the void-reactivity with a negative void reactivity coefficient magnifies the amplitude of the density wave oscillations in BWRs. Therefore, it is of practical importance to evaluate the core-wide and regional stability. The core-wide and regional stability experiments were conducted with the SIRIUS-F facility on the minimum pump speed and natural circulation lines with simulated void-reactivity feedback.

6.6.1 Minimum Pump Speed Line

Figure 6.9 shows the experimental and analytical stability results on the minimum pump speed line. One can estimate both the core-wide and regional stabilities by changing the boundary condition in the computer simulation. Both the core-wide and regional stability features obtained by the design analysis code are plotted in the figure. In the experiment with the SIRIUS-F facility, the least stable mode (corresponding to either the core-wide mode or the regional mode) is excited. Experiments were repeated twice and the results are plotted in the figure.

The upper figure shows the resonance frequency. The resonance frequencies obtained by the SIRIUS-F facility agree very well with the regional resonance frequencies obtained by linear stability analysis. The resonance frequency increases monotonically with increasing power, because the transit time of the channel becomes smaller with increasing power.

The regional stability decay ratios obtained by the linear stability analysis agree well with the experimental decay ratios. The analytical and experimental decay ratios at the maximum

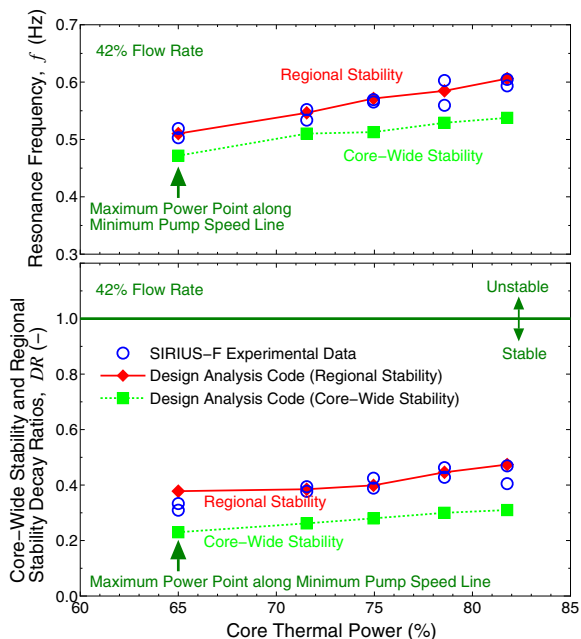


Figure 6.9: Core-wide and regional stability on the minimum pump speed line. The resonance frequencies and decay ratios obtained with the SIRIUS-F facility agreed with those for regional stability obtained by the linear stability analysis. Although the power increases up to 82%, the decay ratios are still lower than 0.8, which is the design criterion in Japan.

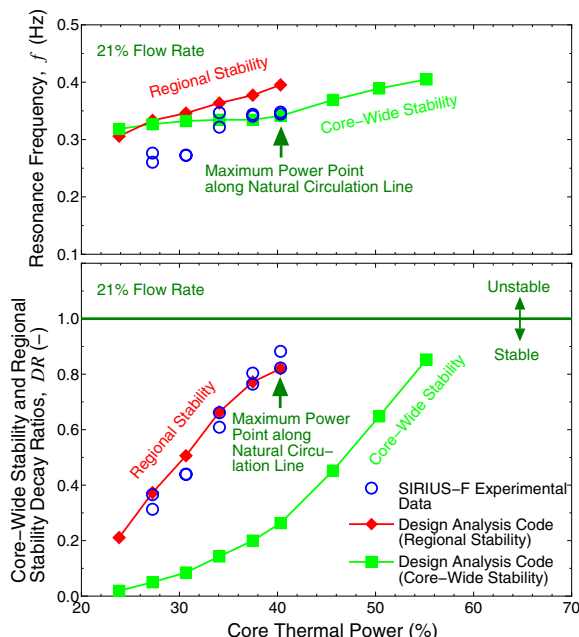


Figure 6.10: Core-wide and regional stability on the natural circulation line. The experimental and analytical regional stability decay ratios are in good agreement. Since $DR < 1.0$, the ABWR will not encounter core-wide or regional instabilities even in the event of malfunctioning of the selected control rods run.

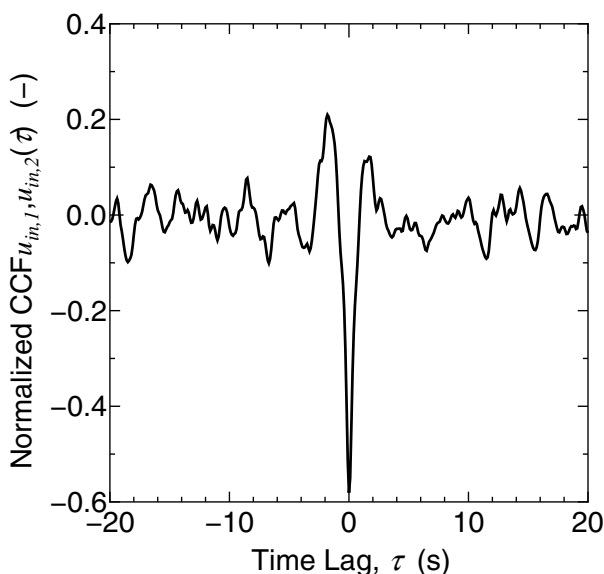


Figure 6.11: Interaction mode between half-cores. The distinct peak of the cross-correlation function of the fluctuations of the two inlet velocities with a negative value is found at $\tau = 0$, indicating an out-of-phase interaction mode between the two core halves (regional stability mode).

power (65 %) on the minimum pump speed line are lower than 0.4, indicating that core-wide and regional stability margins are sufficiently high. The power increases from 64 % to 82 %, and the decay ratio remains lower than 0.5. It can therefore be concluded that the core stability margin is sufficiently large. As the power increases on the minimum pump speed line, all decay ratios increase monotonically. Although the power increases further up to 82 %, the decay ratios are still lower than 0.8 (which is the design criterion in Japan).

6.6.2 Natural Circulation Line

Figure 6.10 shows the experimental and analytical stability results on the natural circulation line. The resonance frequency increases monotonically with increasing power. The resonance frequencies obtained with the SIRIUS-F are scattered among analytical core-wide and regional frequencies. These deviations are not found for the channel stability (see Figure 6.8). At low power, the analytical results show that the resonance frequencies of the core-wide mode are higher than those of the regional mode, which is physically incorrect. We think that the deviations between experimental and analytical resonance frequencies may be caused by the convergency of the linear stability analysis. The decay ratios obtained by the SIRIUS-F facility, however, agree well with the analytical regional stability decay ratios. The decay ratio increases with increasing power. At the maximum power point (40 %) on the natural circulation line, the stability decay ratio is approximately 0.8 in both analytical and experimental results. The power increases from 64 % to 82 %, and the decay ratio is lower than 0.5. It can be concluded that the core stability margin is sufficiently high.

From these findings, one can conclude that the ABWR will not encounter core-wide or regional instability at maximum power on the minimum pump speed and natural circulation lines even if SCRRI malfunctions.

As we discussed, the least stable mode (either the core-wide mode or the regional mode) appears in the experiment. In order to clarify the least stable mode, the cross correlation between fluctuations of the inlet velocities of the two channel is investigated. Figure 6.11 shows the normalized cross-correlation function of the inlet velocities of two channels. The experimental data were obtained at 27 % core thermal power along the natural circulation line (21 % flow). The distinct peak of the cross-correlation function with a negative value was found at $\tau = 0$ for all experimental parameters in this study, indicating an out-of-phase interaction modes between the two core halves (regional stability mode). The values of the decay ratio and the resonance frequency therefore relate to regional stability. The decay ratio in terms of the core-wide stability must be lower than that of the regional stability as demonstrated by the design analysis code.

6.7 Conclusions

- Channel, core-wide, and regional stability experiments were conducted for a wide range of operating conditions, including maximum power points on the minimum pump speed and natural circulation lines of the ABWR.
- The obtained decay ratio and resonance frequency relate to regional stability. This is because the distinct peak of the cross-correlation function with a negative value was found at $\tau = 0$ for all experimental parameters in this study, indicating an out-of-phase interaction mode between the two core halves (regional stability mode).

- The decay ratios and resonance frequencies from the SIRIUS-F facility are in good agreement with those from the design analysis code, ODYSY. The design analysis code, ODYSY is validated with the SIRIUS-F experimental data.
- The SIRIUS-F experimental results demonstrate a destabilizing effect of the increasing power, and show a sufficiently large stability margin even under hypothetical conditions of power enlargement.
- It can be concluded from these stability experiments that the ABWR will not encounter core-wide or regional instabilities even if the selected control rods run in (SCRRI) malfunctions after a pump trip event.

6.8 Recommendation

The experiments and analysis were conducted with two channels, which is the minimum number required to simulate the regional mode. In order to gain more confidence of the stability estimation, a multichannel effect should be studied. The effect can be investigated by an analysis.

Chapter 7

Conclusions

7.1 Concluding Remarks in the Thesis

In the early 1990s, it became very important to assess the feasibility of large-scale natural circulation BWRs. Special attention was paid to the flashing phenomenon. At that time, the mechanism of flashing-induced instability was not yet clear in natural circulation BWRs with a chimney. To cope with the lack of experiments and analytical models for natural circulation BWRs, the SIRIUS-N facility (being a version of the ESBWR) was built to study thermal-hydraulic stability. Subsequently, the facility was equipped with an artificial void-reactivity feedback system to simulate core-wide and regional stabilities. Finally, in order to study forced circulation BWRs, the facility was modified to have a circulation pump without chimneys (the SIRIUS-F facility).

In this thesis, several aspects of the dynamics and stability of natural circulation and forced circulation BWRs have been investigated using four tools: two experimental facilities, a noise analysis code for stability estimation, and a linear stability analysis code to model the two-phase flow stability.

Thermal-Hydraulic Stability of ESBWR The thermal-hydraulic stability of a prototype natural circulation BWR (ESBWR) has been investigated with the SIRIUS-N facility, which is based on the thermal-hydraulic similarity law of the ESBWR. Stability maps have been obtained from 0.1 to 7.2 MPa. It was found that the flow becomes stable below a certain heat flux regardless of the inlet subcooling of the core and the system pressure. Above that heat flux, an instability was observed within a certain range of the inlet subcooling. The unstable region reduces with increasing system pressure. Therefore, the stability can be enhanced in a cold startup process of a reactor by pressurizing the reactor sufficiently before withdrawing control rods (heating the reactor core). Stability maps obtained at all pressures demonstrate that the ESBWR has significant stability margin to the unstable region both at startup and the rated operating conditions.

Instability Mechanisms The driving mechanisms of the thermal-hydraulic instabilities have been studied with the SIRIUS-N facility. Two distinct branches were found in the relation of the oscillation period to the liquid passing time in the chimney, indicating that the driving mechanisms of the instabilities are different for low and high pressures. The transition region between high and low pressures lies between 0.5 MPa and 1.0 MPa.

At low pressures (0.1 - 0.5 MPa), the observed instability is shown to be caused by flashing induced density wave oscillations. Here, flashing suddenly occurs in the chimney section (on top of the core) which increases the natural circulation flow. In the mean

time, cold water fills in, since the residence time in the core becomes very short due to a high flow rate. After the cold water flushes out the bubbles generated by the flashing, the flow becomes stagnant. The residence time in the core, in turn, becomes longer, resulting in hot water rising in the chimney to make flashing happen again. In these processes, the stagnant flow process takes the longest time period. Therefore, it is found experimentally that the oscillation period correlates well with the passing time in the chimney for liquid single-phase flow in the chimney regardless of the heat flux, system pressure, and inlet subcooling. It is found that flashing induces density wave oscillations above approximately 1.1 % of the quality at the chimney exit only.

At high pressures (1.0 - 7.2 MPa), the observed instability is shown to be caused by Type-I density wave oscillations, since the void fractions in the chimney inlet and exit are out of phase, and the instability occurs at low quality. These facts clearly indicate the characteristics of density wave oscillations. In other words, the instability is caused by the time lag between the moment that steam is generated in the core and the moment that the steam flows into the chimney (where it induces natural circulation flow). Therefore, the oscillation period correlates well with the time required for the bubbles to pass through the chimney regardless of the heat flux, system pressure, and inlet subcooling.

Stability Enhancement Method A method to stabilize the thermal-hydraulic instability has been investigated experimentally and analytically. Inlet throttling is a well established method to stabilize the density wave oscillations for a forced circulation system. In a natural circulation system, however, increasing the inlet throttling reduces the natural circulation flow rate, resulting in a shift of the unstable region to higher inlet subcoolings. It was found that the void fraction in the chimney for operating conditions close to the stability boundary is approximately constant regardless of the inlet throttling. Using the homogeneous equilibrium mixture model, together with the void fraction at operating conditions close to the stability boundary, the stability map can therefore be predicted for a range of inlet restrictions.

Prediction of Stability Boundary A linear stability analysis code, based on the homogeneous equilibrium mixture model, was used to predict the stability boundaries for the lower subcooling for the natural circulation BWR. The analytical stability boundary agrees well with the experimentally-obtained stability boundary. Moreover, the linear stability analysis calculates the experimentally obtained oscillation period as a function of the bubble passing time in the chimney. We verified that the experimentally-observed instability at high pressure falls in the category of the Type-I density wave oscillations by comparing it with the linear stability analysis.

Effect of Single-Phase Natural Circulation The natural circulation flow is driven by both the single-phase natural circulation and the boiling two-phase flow in the core and chimney. The single-phase natural circulation is induced by the difference between the liquid density in the downcomer and the liquid density in the chimney (and the core), since the water in the downcomer is subcooled. In order to investigate the effect of liquid density differences on the thermal-hydraulic stability, the analysis code (based on the homogeneous equilibrium model) was modified to include the dependence of liquid density on temperature. Analytical results showed that neglecting temperature dependence of the density yields a conservative estimate of the Type-II instability. On the other hand, it gives a non-conservative estimate of Type-I instability, since operating conditions shift towards or even into the stable region. Therefore, it is highly recommended to include the

dependence of liquid density on the temperature in a stability analysis, if a boiling natural circulation loop with an adiabatic chimney encounters low flow quality conditions.

Method to Implement Artificial Void-Reactivity Feedback In order to simulate core-wide and regional modes, an artificial void-reactivity feedback system was implemented in the SIRIUS-N facility. Void fractions are calculated in each section using the measured differential pressure, inlet velocity, and inlet temperature. The analysis in estimating the void fraction is based on the drift flux model. Using the estimated void fractions in reactor core sections of the thermal-hydraulic loop, the real-time simulation calculates the void-reactivity feedback based on the modal point kinetics of reactor neutronics. Solid-state, series-regulated power supplies that act as simulation output, were designed to obtain fast response speed without loss of accuracy (time constant of 0.3 ms based on a step response test; accuracy of 99.9 % in power amplitude and less than one degree of phase lag based on a noise response test within a target frequency range of 0.3 to 0.5 Hz).

Noise Analysis for Stability Estimation In order to obtain the decay ratio, a noise analysis on the basis of an auto-regressive method has been applied to time series data of the core inlet flow rate. The validity of this method is clearly demonstrated by a reconstructed power spectral density of the inlet flow rate.

Core-Wide and Regional Stabilities of the ESBWR In order to estimate the regional stability of the ESBWR, experiments were conducted with the SIRIUS-N facility together with the developed artificial void-reactivity feedback. Channel and regional stability decay ratios at the rated operating condition were determined to be 0.38 and 0.54, indicating sufficient margin to instabilities.

The experiments were extended to evaluate the stability sensitivity of the design parameters such as the power profile, the void reactivity coefficients, core inlet subcooling, and thermal conductance of the fuel rod. The decay ratio reaches a local maximum when the fuel rod time constant is approximately 6.7 s. Therefore, the system approaches the least stable condition when the oscillation period of the thermal-hydraulic instability corresponding to the phase lag of the void-reactivity feedback system.

In order to identify instability phenomena, the experiments were further extended to include a hypothetical parameter range (double-void reactivity coefficient and inlet core subcooling increased by a factor of 3.6). The regional instability was clearly demonstrated with the SIRIUS-N facility, when the fuel rod time constant matches the oscillation period of the density wave oscillations.

Core-Wide and Regional Stabilities of the ABWR The method to implement artificial neutronic feedback has also been applied to the SIRIUS-F facility, which is the full-height test facility of the ABWR (which is a forced circulation BWRs). Channel and regional stability experiments were conducted for a wide range of operating conditions including the minimum pump speed and natural circulation lines of the ABWR. A distinct peak of the cross correlation function with a negative value is found at $\tau = 0$ for all experimental parameters in this study, indicating an out-of-phase interaction modes between the two core halves (regional stability mode). Therefore, the ABWR is more susceptible to the regional instability.

The decay ratios and the resonance frequencies obtained from the SIRIUS-F facility are in good agreement with those from the design analysis code, ODYSY, although some discrepancy are found only in the regional stability resonance frequency on the natural

circulation line. The code is validated with the SIRIUS-F facility. It can be concluded from the stability experiments that the ABWR will not encounter core-wide or regional instability at the maximum power on the minimum pump speed and natural circulation lines even at malfunctioning of the safety feature (SCRRI: the Selected Control Rods Run-In).

7.2 Future Work

Some future work related to the investigation of the stability of BWRs is discussed in the following.

Flashing-Induced Type-II Instability Flashing induced *Type-I instability* can clearly take place in a two-phase flow loop with a chimney, since the amplitude of the quality to void fraction transfer function is relatively large at low qualities. However, one should not think that flashing-induced instability occurs in Type-I instability regions only. Flashing may amplify (or practically induce) *Type-II instabilities*, when the amplitude of the quality to void fraction transfer function is relatively large at high quality. In order to make it happen, one should conduct experiments where the change in saturation enthalpy with pressure is large: e.g. a boiling loop with high exit friction operating at low pressure. The flashing induced Type-II instability may be practically important for two-phase systems operated in aerospace (at low pressure) and for rotating machines (subjected to the high centrifugal force).

Amplitude of Limit Cycles The stability boundary can be predicted with linear stability analysis. In practical situations, even when a linear stability analysis gives a decay ratio higher than unity to a certain degree, a flow excursion may not take place. Limit cycle oscillations could occur due to nonlinearity in a boiling two-phase flow, instead. According to present developments in the field of nonlinear time-domain analysis, it is still difficult to accurately predict the amplitude of such oscillations. Research should therefore be performed on a nonlinearity in the boiling two-phase flow. In order to validate nonlinear analyses, experiments must be conducted in a simple geometry at well-controlled experimental conditions and system parameters with high accuracy.

Transient Correlations Describing Two-Phase Flow Almost all correlations for two-phase flow are formulated on the basis of steady-state experiments. In order to analyze oscillatory and transient flows, experimental data must be obtained at transient conditions. In this thesis, we use the drift flux model to estimate the transient void fraction. Parameters used in the drift flux model (the drift velocity and distribution coefficient) could then be determined for more reliable estimation under transient two-phase flows. In the two fluid model, which is used in the transient analysis code, phasic correlations for a two fluid model (e.g. interfacial area concentration) could be obtained to improve the accuracy of the stability analysis.

Multidimensional Flow in The Chimney The flow in the chimney is assumed to be one dimensional. In reality, the diameter of a subchannel in the chimney section could be roughly 1 m in the ESBWR (total diameter of the chimney is 3 m to 7 m). The flow structure could be three dimensional, encountering internal circulation, drift flow, and sloshing oscillation resulting in a pressure drop in the chimney. Unfortunately, the multidimensional flow in a large diameter tube is not fully understood yet. It is of scientific

and practical significance to investigate the physics of such flow to gain confidence in estimating the stability features and the driving force of natural circulation for reliable cooling. Nonintrusive measurement devices must be developed to acquire distributions of void fraction and phasic velocity to describe drag and lift forces and conditions of the flow pattern transition.

Local Instability Local instability events have been observed in BWR plants. These events were caused by e.g. an obstacle blocking the flow (resulting in a reduction of flow rate) or a control rod withdrawal accident (which leads to a high power condition). The boiling two-phase flow dynamics in one channel does affect and is affected by that in the neighboring channels through both thermal-hydraulics *and* neutronic coupling. This interaction between channels must thoroughly be considered in estimating the local instability. Most of the current investigations on local instability focus on the thermal-hydraulics (i.e. channel instability) only. In order to study local instability with void-reactivity feedback, one should apply different thermal powers to both channels separately in the SIRIUS-F facility and solve void-reactivity feedback between the channels.

Appendix A

Reduced-order Model

The following equations constitute the reduced-order model of Van Bragt and Van der Hagen (1998c).

A.1 Neutron Kinetics

Using one effective delayed neutron group:

$$\frac{dn(t)}{dt} = \frac{\rho(t) - \beta}{\Lambda} n(t) + \lambda c(t), \quad (\text{A.1})$$

$$\frac{dc(t)}{dt} = \frac{\beta}{\Lambda} n(t) - \lambda c(t). \quad (\text{A.2})$$

A.2 Fuel Dynamics

$$\frac{d}{dt} \frac{q''(t)}{q''_o} = \frac{1}{\tau_f} \left[\frac{q'(t)}{q'_o} - \frac{q''(t)}{q''_o} \right], \quad (\text{A.3})$$

where $q''(t) = h_{overall}[T_f(t) - T_{sat}]$.

A.3 Boiling Boundary Dynamics

$$\frac{dz_{bb}(t)}{dt} = 2 \left[\frac{M_{C,i}(t)}{\rho_l} - \frac{q'(t)z_{bb}(t)}{\rho_l A_C (h_l - h_{C,i})} \right]. \quad (\text{A.4})$$

A.4 Core Void Dynamics

$$\frac{d \langle \alpha(t) \rangle_C}{dt} = \frac{M_{C,e}(t) - M_{C,i}(t)}{(\rho_l - \rho_g) L_C}, \quad (\text{A.5})$$

$$M_{C,i}(t) = M_{C,e}(t) \left[1 + \frac{\rho_l - \rho_g}{\rho_g} x_{C,e}(t) \right] - \frac{(\rho_l - \rho_g)}{\rho_g} \frac{[L_C - z_{bb}(t)] q'(t)}{A_C (h_g - h_l)}, \quad (\text{A.6})$$

$$\langle \alpha(t) \rangle_C = \frac{L_C - z_{bb}(t)}{L_C} \frac{\rho_l}{\rho_l - \rho_g} \left\{ 1 - \frac{\rho_g}{(\rho_l - \rho_g) x_{C,e}(t)} \ln \left[1 + \frac{\rho_l - \rho_g}{\rho_g} x_{C,e}(t) \right] \right\}. \quad (\text{A.7})$$

A.5 Chimney Void Dynamics

For the n^{th} chimney node

$$\frac{d \langle \alpha(t) \rangle_{r,n}}{dt} = \frac{M_{r,n}(t) - M_{r,n-1}(t) N_r}{\rho_l - \rho_g} \frac{N_r}{L_r}, \quad (\text{A.8})$$

$$M_{r,n-1}(t) \left[1 + \frac{\rho_l - \rho_g}{\rho_g} x_{r,n-1}(t) \right] = M_{r,n}(t) \left[1 + \frac{\rho_l - \rho_g}{\rho_g} x_{r,n}(t) \right], \quad (\text{A.9})$$

$$\langle \alpha(t) \rangle_{r,n} = \frac{\rho_l}{\rho_l - \rho_g} \left\{ 1 - \frac{\rho_g}{(\rho_l - \rho_g)(x_{r,n}(t) - x_{r,n-1}(t))} \ln \left[1 + \frac{\rho_l - \rho_g}{\rho_g} \frac{x_{r,n}(t) - x_{r,n-1}(t)}{1 + x_{r,n-1}(t) \frac{\rho_l - \rho_g}{\rho_g}} \right] \right\}, \quad (\text{A.10})$$

where N_r is the number of chimney nodes.

A.6 Mass-flux Density Dynamics

The mass-flux density equation is given implicitly by the integral momentum equation along the closed natural-circulation loop:

$$\Delta P_C(t) + \Delta P_r(t) + \Delta P_d(t) = 0, \quad (\text{A.11})$$

where the different types of pressure drops accounted for in the model are summarized in Table A.1:

Table A.1: Pressure Drops in Reduced-Order Model

Location	Description
1. Inertia	
Core	$z_{bb}(t) \frac{dM_{C,i}(t)}{dt} + [L_C - z_{bb}(t)] \frac{dM_{C,e}(t)}{dt} + [M_{C,i}(t) - M_{C,e}(t)] \frac{dz_{bb}(t)}{dt}$
Chimney	$\sum_{n=1}^{N_r} \frac{L_r}{N_r} \frac{d\langle M \rangle_{r,n}(t)}{dt}$
Downcomer	$\left(\frac{L}{A}\right) \frac{d\Phi(t)}{dt}$
2. Acceleration	
Core	$\frac{M_{C,e}^2(t)}{\rho_l} \phi^2[x_{C,e}(t)] - \frac{M_{C,i}^2(t)}{\rho_l}$
Chimney	$\frac{M_{r,e}^2(t)}{\rho_l} \phi^2[x_{r,e}(t)] - \frac{M_{r,i}^2(t)}{\rho_l} \phi^2[x_{r,i}(t)]$
Downcomer	$\frac{\Phi^2(t)}{2\rho_l} \left(\frac{1}{A_{d,e}^2} - \frac{1}{A_{d,i}^2}\right)$
3. Gravity	
Core	$L_C g [\rho_l (1 - \langle \alpha(t) \rangle_C) + \rho_g \langle \alpha(t) \rangle_C]$
Chimney	$\sum_{n=1}^{N_r} L_r g [\rho_l (1 - \langle \alpha(t) \rangle_{r,n}) + \rho_g \langle \alpha(t) \rangle_{r,n}]$
Downcomer	$-\rho_l g (L_C + L_r)$
4. Wall Friction	
Core	$z_{bb}(t) \frac{f_C}{2D_C} \frac{M_{C,i}^2(t)}{\rho_l} + [L_C - z_{bb}(t)] \frac{f_C}{2D_C} \frac{M_{C,e}^2(t)}{\rho_l} \phi^2\left[\frac{1}{2}x_{C,e}(t)\right]$
Chimney	$\sum_{n=1}^{N_r} \frac{L_r}{N_r} \frac{f_r}{2D_r} \frac{\langle M(t) \rangle_{r,n}^2}{\rho_l} \phi^2[\langle x(t) \rangle_{r,n}]$
5. Local Pressure Drop	
Inlet core	$K_{C,i} \frac{M_{C,i}^2(t)}{2\rho_l}$
Exit core	$K_{C,e} \frac{M_{C,e}^2(t)}{2\rho_l} \phi^2[x_{C,e}(t)]$
Chimney exit	$K_{r,e} \frac{M_{r,e}^2(t)}{2\rho_l} \phi^2[x_{r,e}(t)]$
Inlet downcomer	$K_{d,i} \frac{M_{d,i}^2(t)}{2\rho_l}$

Appendix B

Transfer Functions Used in the Frequency-Domain Analysis

The following transfer functions appearing in the block diagram of figure 3.12 can be derived from the above equations. The zero-power reactivity transfer function derived from the point-kinetic equations is given as follows:

$$G_R = \frac{\frac{\delta P}{P_o}}{\delta \rho} = \frac{s + \lambda}{\Lambda s^2 + (\lambda \Lambda + \beta)s}. \quad (\text{B.1})$$

The transfer function describing the heat transfer from fuel to coolant is

$$G_F = \frac{\frac{\delta q''}{q_o}}{\frac{\delta P}{P_o}} = \frac{1}{\tau_f} \frac{1}{s + \frac{1}{\tau_f}}; \quad (\text{B.2})$$

The transfer function from the heat flux and from the core-inlet mass flux to the boiling-boundary position are

$$G_{z_{bb}, q''} = \frac{\frac{\delta z_{bb}}{z_{bb,o}}}{\frac{\delta q''}{q_o}} = \frac{2}{\tau_{nb}} \frac{1}{s + \frac{1}{\tau_{nb}}}, \quad (\text{B.3})$$

where

$$\tau_{nb} = \frac{z_{bb,o} \rho_l}{M_{C,i}};$$

and

$$G_{z_{bb}, M_{C,i}} = -G_{z_{bb}, q''}; \quad (\text{B.4})$$

The transfer function from the heat flux and from the core-inlet mass flux to the core-averaged void fraction are

$$G_{\alpha, q''} = \frac{\frac{\delta \langle \alpha \rangle_C}{\langle \alpha \rangle_{C,o}}}{\frac{\delta q''}{q_o}} = \frac{q_o''}{A_C H \langle \alpha \rangle_o} \frac{1}{s + \frac{1}{\tau_{bb}}}, \quad (\text{B.5})$$

where

$$\tau_{bb} = \frac{-H(L - z_{bb,o})}{2M_{C,i}(h_l - h_g) \frac{\partial \langle \alpha \rangle}{\partial \langle \alpha \rangle}},$$

$$H = (\rho_g h_g - \rho_l h_l) + [(1 - 2 \langle x \rangle_o) h_l + 2 \langle x \rangle_o h_g](\rho_l - \rho_g);$$

and

$$G_{\alpha, M_{C,i}} = -G_{\alpha, q}''; \quad (\text{B.6})$$

The transfer function from the boiling-boundary position to the core-averaged void fraction is

$$G_{\alpha, z_{bb}} = \frac{\frac{\delta \langle \alpha \rangle_C}{\langle \alpha \rangle_{C,o}}}{\frac{\delta z_{bb}}{z_{bb,o}}} = \frac{z_{bb,o}}{LC - z_{bb,o}} \frac{-\mu - \frac{1}{\tau_{bb}}}{s + \frac{1}{\tau_{bb}}}, \quad (\text{B.7})$$

where

$$\mu = \frac{q_o'}{AC H \langle \alpha \rangle_o};$$

The transfer function from the core-averaged void fraction and from the boiling-boundary position to the core-inlet mass flux are

$$G_{M_{C,i}, \alpha} = \frac{\frac{\delta M_{C,i}}{M_{C,i,o}}}{\frac{\delta \langle \alpha \rangle_C}{\langle \alpha \rangle_{C,o}}} = \frac{[(LC - z_{bb,o} + L_r \frac{AC}{A_r})s + K1] \frac{\partial M_{C,e}}{\partial \langle \alpha \rangle_C} + Core + Chimney}{(z_{bb,o} + (L - z_{bb,o}) \frac{\partial M_{C,e}}{\partial M_{C,i}} + L_r \frac{AC}{A_r} + \frac{L}{A_d} AC)s + K1 \frac{\partial M_{C,e}}{\partial M_{C,i}} + K2} \quad (\text{B.8})$$

and

$$G_{M_{C,i}, z_{bb}} = \frac{\frac{\delta M_{C,i}}{M_{C,i,o}}}{\frac{\delta z_{bb}}{z_{bb,o}}} = \frac{[(LC - z_{bb,o} + L_r \frac{AC}{A_r})s + K1] \frac{\partial M_{C,e}}{\partial z_{bb}} + \frac{\partial \Delta P_{fr,C}}{\partial z_{bb}} + \frac{\partial \Delta P_{gr,C}}{\partial z_{bb}}}{(z_{bb,o} + (L - z_{bb,o}) \frac{\partial M_{C,e}}{\partial M_{C,i}} + L_r \frac{AC}{A_r} + \frac{L}{A_d} AC)s + K1 \frac{\partial M_{C,e}}{\partial M_{C,i}} + K2}, \quad (\text{B.9})$$

where

$$Core = \frac{\partial \Delta P_{acc,C}}{\partial \langle \alpha \rangle_C} + \frac{\partial \Delta P_{fr,C}}{\partial \langle \alpha \rangle_C} + \frac{\partial \Delta P_{gr,C}}{\partial \langle \alpha \rangle_C} + \frac{\partial \Delta P_{fr,C,e}}{\partial \langle \alpha \rangle_C},$$

$$Chimney = \left(\frac{\partial \Delta P_{fr,r,e}}{\partial \langle \alpha \rangle_r} + \frac{\partial \Delta P_{fr,r}}{\partial \langle \alpha \rangle_r} + \frac{\partial \Delta P_{acc,r}}{\partial \langle \alpha \rangle_r} + \frac{\partial \Delta P_{gr,r}}{\partial \langle \alpha \rangle_r} + \frac{\partial \Delta P_{in,r}}{\partial \langle \alpha \rangle_r} \right) \frac{\partial \langle \alpha \rangle_r}{\partial \langle \alpha \rangle_C},$$

$$K1 = \frac{\partial \Delta P_{acc,C}}{\partial M_{C,e}} + \frac{\partial \Delta P_{fr,C}}{\partial M_{C,e}} + \frac{\partial \Delta P_{fr,C,e}}{\partial M_{C,e}} + \left(\frac{\partial \Delta P_{fr,r}}{\partial M_{C,e}} + \frac{\partial \Delta P_{fr,r,e}}{\partial M_{C,e}} \right) \frac{AC}{A_r},$$

$$K2 = \frac{\partial \Delta P_{acc,C}}{\partial M_{C,i}} + \frac{\partial \Delta P_{fr,C}}{\partial M_{C,i}} + \frac{\partial \Delta P_{acc,d}}{\partial M_{C,i}} + \frac{\partial \Delta P_{fr,d,i}}{\partial M_{C,i}}.$$

The $\frac{\partial \Delta P}{\partial M}$, $\frac{\partial \Delta P}{\partial \langle \alpha \rangle}$, $\frac{\partial \Delta P}{\partial z_{bb}}$ dynamic pressure drop derivatives appearing in $G_{M_{C,i}, \alpha}$ and $G_{M_{C,i}, z_{bb}}$ can be derived from the dynamic pressure drop terms listed in the above table in a straightforward manner.

Nomenclature

Alphabets

A	cross-sectional flow area	m^2
c	delayed neutron precursor number density	m^{-3}
C_D	normalized Doppler reactivity coefficient	–
C_p	specific heat at constant pressure	$Jkg^{-1}K^{-1}$
C_α	void reactivity coefficients	–
D	hydraulic diameter	m
f	(resonance) frequency	s^{-1}
	friction coefficient	–
g	gravitational acceleration	ms^{-2}
G_1	auxiliary transfer function	–
G_A	normalized transfer function from heat flux to void fraction	–
G_F	normalized transfer function from power to heat flux	–
G_R	zero power reactivity transfer function	–
$G_{x,y}$	transfer function from y to x	–
h	specific enthalpy	Jkg^{-1}
h_{fg}	latent heat	Jkg^{-1}
$h_{overall}$	overall heat transfer coefficient	$Js^{-1}K^{-1}m^{-2}$
L	length	m
M	mass flux density	$kgm^{-2}s^{-1}$
M_{local}	local (concentrated) friction	$kgm^{-2}s^{-2}$
M_{wall}	wall friction	$kgm^{-2}s^{-2}$
n	neutron number density	m^{-3}
P	pressure	$kgm^{-1}s^{-2}$
	power	Js^{-1}
P_e	perimeter	m
P_s	system pressure	$kgm^{-1}s^{-2}$
q''	heat flux density from fuel to coolant	$Jm^{-2}s^{-1}$
q'''	volumetric power generation rate in the fuel	$Jm^{-3}s^{-1}$
s	Laplace variable	s^{-1}
t	time	s
T	temperature	K
u	velocity	ms^{-1}
u_{in}	velocity at channel inlet	ms^{-1}
v_{gj}	drift velocity	ms^{-1}
V	volume	m^3
x	flow quality, thermodynamic equilibrium quality	–
z	axial position	m

z-transform variable —

Greek symbols

α	void fraction	—
β	delayed neutron fraction	—
ΔP	differential pressure	$kgm^{-1}s^{-2}$
$\delta(x)$	Dirac's delta function	—
ε	λ -mode eigenvalue separations	—
$\kappa_{C,in}$	orifice coefficient at the channel inlet	—
$\kappa_{R,ex}$	orifice coefficient at the chimney exit	—
Λ	neutron generation time	s
λ	eigenvalue	—
	delayed neutron precursor decay constant	s^{-1}
ν	average number of neutrons released per fission	—
ω	the imaginary part of s	s^{-1}
ρ	density	kgm^{-3}
	reactivity	—
σ	the real part of s	s^{-1}
Σ_a	one-group absorption cross section	m^{-1}
Σ_f	one-group fission cross section	m^{-1}
τ	time constant	s
τ_f	fuel rod time constant	s
τ_{fo}	flow oscillation period	s
τ_{pr}	passing time in the chimney	s
ϕ	neutron flux	$m^{-2}s^{-1}$

Subscripts

1ϕ	one phase
2ϕ	two phase
C	core
c	critical (reactor) state
ch	channel
d	downcomer
eff	effective
ex	exit
f	fuel
g	saturated gas
in	inlet
l	property of the liquid phase
m	mode order
n	mode order
nb	non-boiling
r	chimney
sat	saturation
sub	subcooled

Superscripts

*	adjoint
$\hat{}$	dimensionless
F	excitation
S	subcriticality

Operators

Δ	difference
$\langle \rangle$	time average

Dimensionless numbers

\hat{A}_d	nondimensional downcomer cross sectional area	$\hat{A}_d = \frac{A_d}{A_c}$
\hat{A}_r	nondimensional chimney cross sectional Area	$\hat{A}_r = \frac{A_r}{A_c}$
\hat{L}_r	nondimensional chimney length	$\hat{L}_r = \frac{L_r}{L_c}$
N_f	flashing parameter	$N_f = \frac{h_{l, ch, in} - h_{l, r, ex}}{h_{fg}} \left(\frac{\rho_{l, r, ex}}{\rho_{g, r, ex}} - 1 \right)$
N_{Fr}	Froude number	$N_{Fr} = \frac{u_{in}^2}{gL_c}$
N_{sub}	subcooling number	$N_{sub} = \frac{C_{pl} \Delta T_{sub}}{h_{gl}} \left(\frac{\rho_{l, r, ex}}{\rho_{g, r, ex}} - 1 \right)$
N_{pch}	phase change (Zuber) number	$N_{pch} = \frac{P_e q'' L_c}{A_c \rho_{l, ch, in} h_{gl}} \left(\frac{\rho_{l, r, ex}}{\rho_{g, r, ex}} - 1 \right)$
R_{gl}	ratio of vapor to liquid densities	$R_{gl} = \frac{\rho_l}{\rho_g}$
\hat{v}_{gj}	nondimensional drift velocity	$\hat{v}_{gj} = \frac{v_{gj}}{u_{in}}$

Abbreviations

ABWR	Advanced Boiling Water Reactor
AI	Analog Input
AO	Analog Output
ANL	Argonne National Laboratory
APRM	Average Power Range Monitor
AR	autoregressive
BWR	Boiling Water Reactor
CCF	Cross-Correlation Function
CIRCUS	CIRCULATION during Startup
CRIEPI	Central Research Institute of Electric Power Industry
DESIRE	DELft SIMulated REactor
DPMS	Differential Pressure Measurement System
DR	Decay Ratio
ESBWR	European Simplified Boiling Water Reactor
GFR	Gas-Cooled Fast Reactor
GIF	Generation IV International Forum
GE	General Electric company
GPIB	General Purpose Interface Bus (IEEE-488)
HEM	Homogeneous Equilibrium Mixture (model)
HTR	High Temperature Reactor
IP	Internet Protocol
JPDR	Japan Power Demonstration Reactor

JSBWR	Japanese Simplified Boiling Water Reactor
LFR	Lead-cooled Fast Reactor
LPRM	Local Power Range Monitor
MPS	Minimum Pump Speed
MSR	Molten Salt Reactor
NACUSP	NAtural cirCulation and Stability Performance of BWRs
NC	Natural Circulation
NIC	Network Information Card
ODE	Ordinary Differential Equation
OECD	Organization for Economic Co-operation and Development
PID	Proportional Integral Derivative
R ³	department of Radiation, Radionuclides and Reactors
PLR	Part Length Rod
RMLWR	Reduced Moderation Light Water Reactor
r.m.s.	root mean square
PS	Power Supply
SBWR	Simplified Boiling Water Reactor
SCRRI	Selected Control Rod Run In
SCWR	SuperCritical-Water-cooled Reactor
SFR	Sodium-cooled Fast Reactor
SIRIUS	Simulated Reactivity feedback Implemented into thermal-hydraUlic Stability facility
SIRIUS-F	Simulated Reactivity feedback Implemented into thermal-hydraUlic Stability facility for Forced circulation BWRs
SIRIUS-N	Simulated Reactivity feedback Implemented into thermal-hydraUlic Stability facility for Natural circulation BWRs
TCP	Transmission Control Protocol
TRAC	Transient Reactor Analysis Code
USDOE	United States Department of Energy
USNRC	United States Nuclear Regulatory Commission
VHTR	Very-High-Temperature Reactor
ZOH	Zeroth Hold

List of publications

- M. Furuya, T. Fukahori, S. Mizokami, J. Yokoya, “Development of BWR Regional Stability Facility SIRIUS-F, which Simulates Thermalhydraulics-Neutronics Coupling,” *13th International Heat Transfer Conferences, (to be appeared)* Sydney, Australia, August 13-18, 2006.
- M. Furuya, T. Fukahori, S. Mizokami, “Development of BWR Regional Stability Experimental Facility SIRIUS-F, which Simulates Thermalhydraulics-Neutronics Coupling, and Stability Evaluation of ABWR,” *Nucl. Technol., (to be appeared)* 2006.
- M. Furuya, F. Inada, T. H. J. J. van der Hagen, “Regional Stability Estimation of Natural Circulation BWRs using SIRIUS-N Facility,” *J. Nucl. Sci. Technol.*, Vol.42, No.4, pp.341-350, 2005.
- M. Furuya, F. Inada, T. H. J. J. van der Hagen, “Development of SIRIUS-N facility with simulated void-reactivity feedback to investigate regional and core-wide stability of natural circulation BWRs,” *Nucl. Engng. Des.*, Vol. 235, No.15, pp.1635-1649, 2005.
- M. Furuya and F. Inada, “Development of BWR Regional Stability Experimental Facility SIRIUS-F, Which Simulates Thermalhydraulics-Neutronics Coupling in Reactor Core, And Stability Evaluation of ABWR,” *Proc. Eleventh International Meeting on Nuclear Reactor Thermal-Hydraulics (NURETH-11)*, (CD-ROM Publication), October 2-6, 2005, Avignon, France.
- M. Furuya, F. Inada, T. H. J. J. van der Hagen, “Characteristics of Type-I Density Wave Oscillations in a Natural Circulation BWR at Relatively High Pressure,” *J. Nucl. Sci. Technol.*, Vol.42, No.2, pp.191-200, 2004.
- M. Furuya, F. Inada, T. H. J. J. van der Hagen, “Flashing-Induced Density Wave Oscillations in a Natural Circulation BWR with a Chimney - Mechanism of Instability and Stability Map -,” *Nucl. Engng. Des.*, Vol.235, No.15, pp.1557-1569, 2004.
- M. Furuya and F. Inada, “BWR Regional Stability Estimation using SIRIUS Facility with Noise Analysis Technology,” *Proc. Tenth International Meeting on Nuclear Reactor Thermal-Hydraulics (NURETH-10)*, A503 (CD-ROM Publication), Seoul, Korea, October 5-9,2003.
- M. Furuya, F. Inada and A. Yasuo, “Development of the SIRIUS Facility that Simulates Dynamic Behaviors of a Boiling Water Reactor and Its Stability Estimation on the Basis of Noise Analysis,” *Proc. 9th Asian Congress of Fluid Dynamics (ACFM-9)*, 45, (CD-ROM Publication), May27-31, Isfahan, Iran, 2002.

- M. Furuya, Annalisa Manera, David D. B. van Bragt, Tim H. J. J. van der Hagen, Willy J. M. de Kruijf, “Effect of Liquid Density Differences on Boiling Two-Phase Flow Stability,” *J. Nucl. Sci. Technol.*, Vol.39, No.10, pp.1094-1098, 2002.
- M. Furuya, F. Inada and A. Yasuo, “Development of SIRIUS Facility that Simulates Void-Reactivity Feedback, and Regional and Core-Wide Stability Estimation of Natural Circulation BWR,” *Proc. 9th International Conference on Nuclear Engineering (ICONE-9)*, ICONE-9593, April 8-12, 2001, Nice, France.
- M. Furuya, D. D. B. van Bragt, T. H. J. J. van der Hagen and W. J. M. de Kruijf, “Effect of Liquid Density Difference on Two-Phase Flow Instability,” *Proc. 9th Int. Meeting on Nucl. Reactor Thermal-Hydraulics (NURETH-9)*, F-2 (CD-ROM Publication), San Francisco, USA, 1999.
- M. Furuya, F. Inada and A. Yasuo, “Inlet Throttling Effect on the Boiling Two-Phase Flow Stability in a Natural Circulation Loop with a Chimney,” *Proc. Single and Two-Phase Natural Circulation Conference, EURO THERM Seminar 63*, B6, Genoa, Italy, 1999.
- M. Furuya, F. Inada and A. Yasuo, “Two-Phase Flow Instability in a Boiling Natural Circulation Loop at Relatively High System Pressure,” *Proc. 8th Int. Meeting on Nucl. Reactor Thermal-Hydraulics (NURETH-8)*, Vol.3, pp.1778-1784, Kyoto, 1997.
- M. Furuya, F. Inada, A. Yasuo, “A Study on Thermal-hydraulic Instability of a Boiling Natural Circulation Loop with a Chimney (Part II. Experimental Approach to Clarify the Flow Instability in Detail),” *Heat Transfer Japanese Research*, Vol. 24, No.7, pp.577-588, 1995.
- M. Furuya, F. Inada and A. Yasuo, “Density Wave Oscillations of a Boiling Natural Circulation Loop Induced by Flashing”, *Proc. 7th Int. Meeting on Nucl. Reactor Thermal-Hydraulics (NURETH-7)*, NUREG/CP-0142, Vol.2, pp.923-932, New York, 1995.

Bibliography

- Akaike, H. (1974). "A New Look at the Statistical Model Identification". *IEEE Trans. Autom. Control*, AC-19:716–723.
- Aritomi, M., Chiang, J. H., *et al.* (1992). "Fundamental Studies on Safety-Related Thermo-Hydraulics of Natural Circulation Boiling Parallel Channel Flow Systems Under Start-up Conditions (Mechanism of Geysering in Parallel Channels)". *Accident Analysis, Nuclear Safety*, 33(2):170–182.
- Bouré, J. A., Bergles, J. E., and Tong, L. S. (1973). "Review of Two-Phase Flow Instability". *Nucl. Engng. Des.*, 25:165–192.
- Carmichael, L. A. and Niemi, R. O. (1978). "Transient and Stability at Peach Bottom atomic power station unit 2 at end of cycle 2". EPRI, NP-564.
- Challberg, R. C., Cheung, Y. K., Khorana, S. S., and Upton, H. A. (1998). "ESBWR Evolution of Passive Features". In *Proc. ICONE-6 (6th Int. Conf. Nucl. Engng.)*, San Diego, USA, pages (CD-ROM Publication). ASME.
- Chang, C. J. and Lahey, R. T. (1997). "Analysis of chaotic instabilities in boiling systems". *Nucl. Engng. Des.*, 167:307.
- Cheung, Y. K., Shiralkar, B. S., and Rao, A. S. (1998). "design evolution of natural circulation in ESBWR". In *Proc. ICONE-6 (6th Int. Conf. Nucl. Engng.)*, San Diego, USA, pages (CD-ROM Publication). ASME.
- Chiang, J. H., Aritomi, M., and Mori, M. (1993a). "Fundamental Study on Thermo-Hydraulics during Start-up in Natural Circulation Boiling Water Reactors, (II) Natural Circulation Oscillation Induced by Hydrostatic Head Fluctuation". *J. Nucl. Sci. Technol.*, 30(3):203–211.
- Chiang, J. H., Aritomi, M., and Mori, M. (1993b). "Fundamental Study on Thermo-Hydraulics during Start-up in Natural Circulation Boiling Water Reactors, (II) Natural Circulation Oscillation Induced by Hydrostatic Head Fluctuation". *J. Nucl. Sci. Technol.*, 30(3):203–211.
- Clausse, A. and Lahey, R. T. (1991). "The Analysis of Periodic and Strange Attractors During Density-Wave Oscillations in Boiling Flows". *Chaos, Solitons and Fractals*, 1:167.
- D'Auria, F., Ambrosini, W., Anegawa, T., Blomstrand, J., Betou, J. I. D., Langenbuch, S., Lefvert, T., and Valtonen, K. (1997). "State of the Art Report on Boiling Water Reactor Stability (SOAR on BWRs)". OECD/CSNI report, OECD/GD (97) 13.
- De Hoon, M. J. L., Van der Hagen, T. H. J. J., Schoonewelle, H., and Van Dam, H. (1996). "Why Yule-Walker Should Not Be Used for Autoregressive Modeling". *Ann. Nucl. Energy*, 23(15):1219–1228.

- DeShong, J. A. and Lipinski, W. C. (1958). "Analyses of Experimental Power-reactivity Feedback Transfer Functions for a Natural Circulation Boiling Water Reactor". Technical Report ANL-5850, Argonne National Laboratory.
- Fukuda, K. and Kobori, T. (1979). "Classification of Two-Phase Flow Instability by Density Wave Oscillation Model". *J. Nucl. Sci. Technol.*, 16(2):95–108.
- Furuya, M., Inada, F., and Van der Hagen, T. H. J. J. (2004). "Flashing-Induced Density Wave Oscillations in a Natural Circulation Loop with a Chimney - Mechanism of Instability and Stability Map -". *Nuclear Engineering Design*, 235(15):1557–1569.
- Furuya, M., Inada, F., and Yasuo, A. (1995). "Density Wave Oscillations of a Boiling Natural Circulation Loop Induced by Flashing". *Proc. 7th Int. Meeting on Nucl. Reactor Thermal-Hydraulics, NUREG/CP-0142*, 2:923–932.
- Garea, V. B., Chang, C. J., Bonetto, F. J., Drew, D. A., and Lahey, R. T. (1994). "The analysis of nonlinear instabilities in boiling systems". In *New Trends in Nuclear System Thermohydraulics, Pisa, Italy*.
- Gialdi, E., Grifoni, S., Parmeggiani, C., and Tricoli, C. (1984). "Core Stability in Operating BWR: Operational Experience". In *Specialists Meeting on Reactor Noise: SMORN IV*, volume Dijon, France, October 15-19.
- Gialdi, E., Grifoni, S., Parmeggiani, C., and Tricoli, C. (1985). "Core stability in operating BWR: operational experiences". In *Prog. Nucl. Energy*, volume 15, pages 447–459.
- Hashimoto, K. (1993). "Linear Modal Analysis of Out-of-Phase Instability in Boiling Water Reactor Cores". *Ann. Nucl. Energy*, 20(12):789–797.
- Hitachi, Ltd. (1998). "Stability Analysis Methodology of Boiling Water Nuclear Reactor". Hitachi HLR-013, 4th Ed.
- Iguchi, T., Ohmizu, S., *et al.* (2000). "Core Thermal-Hydraulic Transient Test for LWRs". *Ann. Mtg. Atomic Energy Society of Japan (in Japanese)*, E28:499.
- Iguchi, T., Shibamoto, Y., Asaka, H., and Nakamura, H. (2003). "Experimental Study on Thermal-Hydraulics and Neutronics Coupling Effect on Flow Instability in A Heated Channel with THYNC Facility". *Proc. Tenth International Meeting on Nuclear Reactor Thermal-Hydraulics*, pages (CD-ROM Publication).
- Inada, F., Furuya, M., *et al.* (1995). "Thermo-Hydraulic Instability of Natural Circulation BWRs at Low Pressure Start-up: Experimental Estimation of Instability Region with Test Facility Considering Scaling Law". *Proc. 3rd JSME/ASME Joint Int. Conf. Nucl. Engng.*, 1:173–178.
- Ishii, M. (1976). "Study of Flow Instabilities in Two-Phase Mixtures". Technical Report ANL76-23, ANL.
- Ishii, M. (1977). "One-Dimensional Drift-Flux Model and Constitutive Equations for Relative Motion Between Phases in Various Two-phase Flow Regimes". Technical report, ANL77-47.
- Ishii, M. and Zuber, N. (1970). "Thermally induced flow instabilities in two-phase mixtures". In *Proc. 4th International Heat Transfer Conference*, volume B5.11, Paris.

- Kakac, S. and Liu, H. T. (1991). "Two-phase flow dynamics instabilities in boiling systems". In *Multiphase Flow and Heat Transfer, Second International Symposium*, pages 403–444, Washington, DC. Hemisphere.
- Karve, A. A., Rizwan-uddin, and Dorning, J. J. (1997). "Stability analysis of BWR nuclear-coupled thermal-hydraulics using a simple model". *Nucl. Engng. Des.*, 177:155.
- Kok, H. and Van der Hagen, T. H. J. J. (1999a). "Design of a Simulated Void-Reactivity Feedback in a Boiling Water Reactor Loop". *Nuclear Technology*, 128(1):1–11.
- Kok, H. V. and Van der Hagen, T. H. J. J. (1999b). "Design of a Simulated Void-Reactivity Feedback in a Boiling Water Reactor Loop". *Nucl. Technol.*, 128:1–11.
- Kok, H. V. and Van der Hagen, T. H. J. J. (1999c). "Modeling the Statics of a Natural-Circulation Boiling Water Reactor Loop". *Nucl. Technol.*, 127:38–48.
- Lahey, R. T. and Moody, F. J. (1993). "*The thermal-hydraulics of a boiling water reactor*". American Nuclear Society.
- Lahey, R. T. and Yadigaroglu, G. (1982). "On the relationship between Ledinegg and density wave instability analysis". *Trans. Am. Nucl. Soc.*, 41:689.
- Larsen, N. H. (1978). "Core design and operation data for cycle 1 and 2 of Peach Bottom 2". EPRI, NP-563.
- Lee, S. Y. and Lee, D. W. (1991). "Linear analysis of flow instabilities in an open two-phase natural circulation loop". *Nucl. Engng. Des.*, 128:317.
- Lin, J. H. *et al.* (1993). "SBWR Core Thermal-Hydraulic Analysis During Start-up". *Proc. 2nd JSME/ASME Joint Int. Conf. Nucl. Engng.*, 1:281–285.
- Manera, A. (2003). "*Experimental and Analytical Investigations on Flashing-Induced Instabilities in Natural Circulation Two-Phase Systems*". PhD thesis, Delft University of Technology, Delft, The Netherlands.
- Manera, A. and Van der Hagen, T. H. J. J. (2003). "Stability of Natural-Circulation-Cooled Boiling Water Reactors During Startup: Experimental Results". *J. Nuclear Technology*, 143(1):77–88.
- March-Leuba, J. and Blakeman, E. D. (1991). "A Mechanism for Out-of Phase Power Instabilities in Boiling Water Reactors". *Nuclear Science and Engineering*, 107:173.
- March-Leuba, J., Cacuci, D. G., and Perez, R. B. (1986a). "Nonlinear Dynamics and Stability of Boiling Water Reactors: Part 1 - Qualitative Analysis". *Nucl. Sci. Engng.*, 93:111–123.
- March-Leuba, J., Cacuci, D. G., and Perez, R. B. (1986b). "Nonlinear Dynamics and Stability of Boiling Water Reactors: Part 2 - Quantitative Analysis". *Nucl. Sci. Engng.*, 93:124.
- Masuhara, Y. *et al.* (1993). "Research on Geysering Phenomena in the Natural Circulation BWR". *Proc. 2nd JSME/ASME Joint Int. Conf. Nucl. Engng.*, 1:135–141.
- Mathisen, R. P. (1967). "Out of Phase Instability in the Loop Skälvan". In *Symp. on Two-phase Dynamics*, pages 19–64, Eindhoven, EUR4288e.

- McCandless, R. J. and Redding, J. R. (1989). "Simplicity: the key to improved safety, performance and economics (SBWR reactor)". *Nucl. Engng. Int.*, 34:20–24.
- Miida, J. and Suda, N. (1963). "Derivation of transfer functions of natural circulation boiling water reactor". Technical Report JAERI-1044, JAERI.
- Mishima, K. and Ishii, M. (1984). "Flow Regime Transition Criteria for Upward Two-phase Flow in Vertical Tubes". *Int. J. Heat Mass Transfer*, 27(5):723–737.
- Muñoz-Cobo, J. L., Rosello, O., Miro, R., Escriva, A., Ginestar, D., and Verdu, G. (2000). "Coupling of density wave oscillations in parallel channels with high order modal kinetics: Application to BWR out of phase oscillations". *Annals Nucl. Energy*, 27(15):1345–1371.
- Murley, T. E. (1990). "Developments in nuclear safety". *Nucl. Safety*, 31:1–19.
- Nakanishi, S. (1979). "Recent Japanese research on two-phase flow instabilities". In *Proceedings of Japan-US Seminar on Two-phase Flow Dynamics*. Hemisphere Publishing Corporation.
- Nakanishi, S., Ishigai, S., Ozawa, M., Mizuta, Y., and Tarui, H. (1978). "Flow Instability in Boiling Channels; 2. Geysering". *Trans. JSME J. Heat Transfer (in Japanese)*, 44(388):4252–4262.
- Nayak, A., Vijayan, P. K., Saha, D., Venkat, R. V., and Aritomi, M. (1998). "Linear Analysis of Thermohydraulic Instabilities of the Advanced Heavy Water Reactor (AHWR)". *J. Nucl. Sci. Technol.*, 35:768–778.
- Nayak, A. K., Vijayan, P. K., Jain, V., Saha, D., and Sinha, R. K. (2003). "Study on the flow-pattern-transition instability in a natural circulation heavy water moderated boiling light water cooled reactor". *Nucl. Engng. Design*, 225(2-3):159–172.
- NRC, U. (1988). "Augmented Inspection Team (AIT) report". Report no. 50-373/88008, US NRC.
- Ott, K. O. and Neuhold, R. J. (1985). "*Nuclear Reactor Dynamics*". American Nuclear Society, La Grange Park, Illinois, USA.
- Ozawa, M. (1999). "Flow Instability Problems in Steam-Generating Tubes". In Ishigai, S., editor, *Steam Power Engineering - Thermal and Hydraulic Design Principles*, chapter 5, pages 323–385. Cambridge University Press.
- Pinheiro Rosa, M. and Podowski, M. Z. (1994). "Nonlinear effects in two-phase flow dynamics". *Nucl. Engng. Des.*, 146:277–288.
- Prasser, H. M., Böttger, A., and Zschau, J. (1998). "A new electrode-mesh tomograph for gas-liquid flows". *Flow Measurement and Instrumentation*, 9:111–129.
- Rao, Y. F., Fukuda, K., and Kaneshima, R. (1995). "Analytical study of coupled neutronic and thermodynamic instabilities in a boiling channel". *Nucl. Engng. Des.*, 154:133.
- Sandoz, S. A. and Chen, S. F. (1983). "Vermont Yankee stability tests during cycle 8". *ANS Trans.*, 45:754.

- Shiralkar, B. S. (1997). “*State of the Art Report on Boiling Water Reactor Stability (SOAR on BWRs)*”, OECD/CSNI report. Chapter 4: Modelling Features and Assessment. OECD/GD (97) 13.
- Tabata, H., Tominori, S., Cheung, Y. K., and Rao, A. S. (1997). “Optimization of Power Output for JSBWR”. *The 5th Int. Conf. on Nucl. Engng.(ICONE5)*, 2050:(CD-ROM Publication).
- Takigawa, Y., Takeuchi, Y., Tsunoyama, S., Ebata, S., Chan, K. C., and Tricoli, C. (1987). “Caorso limit cycle oscillation analysis with three-dimensional transient code TOSDYN-2”. *Nuclear Technology*, 79:210–227.
- Taylor, J. J. (1989). “Improved and safer nuclear power”. *Science*, 244:318–325.
- Thie, J. A. (1958). “Theoretical Reactor Statics and Kinetics of Boiling Reactors”. In *Proc. Geneva Conf.*, page 440, Geneva, Switzerland. Stanford University Press, CA.
- Toshiba Co. (1998). “stability analysis methodology of boiling water nuclear reactor”. Toshiba TLR-013, 4th Ed.
- Uehiro, K. ((In Japanese) 1997). “*A Fundamental Study on Coupled Thermal-Hydraulics - Neutronics Instability in Boiling Water Reactors*”. PhD thesis, Doctoral Dissertation, Sch. Engng. Kyushu Univ., Japan.
- USDOE Nuclear Energy Research Advisory Committee and the Generation IV International Forum (2002). “*A Technology Roadmap for Generation IV Nuclear Energy Systems*”. GIF-002-00.
- Van Bragt, D. and Van der Hagen, T. (1998a). “Stability of Natural Circulation Boiling Water Reactors: Part I Description Stability Model and Theoretical Analysis in Terms of Dimensionless Groups”. *Nucl. Technol.*, 121:40–51.
- Van Bragt, D. and Van der Hagen, T. (1998b). “Stability of Natural Circulation Boiling Water Reactors: Part II Parametric Study of Coupled Neutronic-Thermalhydraulic Stability”. *Nucl. Technol.*, 121:52–61.
- Van Bragt, D. D. B., Rizwan-uddin, and Van der Hagen, T. H. J. J. (1999). “Nonlinear analysis of a natural circulation boiling water reactor”. *Nucl. Sci. Engng.*, 131:23–44.
- Van Bragt, D. D. B. and Van der Hagen, T. H. J. J. (1998c). “Stability of Natural Circulation Boiling Water Reactors: Part I - Description Stability Model and Theoretical Analysis in Terms of Dimensionless Groups”. *Nucl. Technol.*, 121:40–51.
- Van Bragt, D. D. B. and Van der Hagen, T. H. J. J. (1998d). “Stability of Natural Circulation Boiling Water Reactors: Part I, Description Stability Model and Theoretical Analysis in Terms of Dimensionless Groups”. *Nucl. Technol.*, 121:40.
- Van der Hagen, T. H. J. J., Pázsit, I., Thomson, O., and Melkerson, B. (1994). “Methods for The Determination of The In-Phase and Out-Of-Phase Stability Characteristics of A Boiling Water Reactor”. *Nuclear Technology*, 107:193–214.
- Van der Hagen, T. H. J. J. and Stekelenburg, A. J. C. (1995). “The Low-power Low-pressure Flow Resonance in a Natural Circulation Cooled Boiling Water Reactor”. *Proc. 7th Int. Mtg. Nucl. Reactor Thermal-Hydraulics, NUREG/CP-0142*, 4:2785–2795.

- Van der Hagen, T. H. J. J., Stekelenburg, A. J. C., and Van Bragt, D. D. B. (2000). "Reactor Experiments on Type-I and Type-II BWR Stability". *Nucl. Engng. Design*, 200:177–185.
- Wang, F. S., Hu, L. W., and Pan, C. (1994). "Thermal and Stability Analysis of a Two-Phase Natural Circulation Loop". *Nucl. Sci. Engng.*, 117:33–46.
- Wissler, E., ISBIN, H. . S., and AMUDSON, N. R. (1956). "Oscillatory Behavior of A Two-Phase Natural-Circulation Loop". *AIChE Journal*, 2:157–162.
- Yadigaroglu, G. (1981a). "*Two-phase flow instabilities and propagation phenomena*", chapter 17, pages 353–403. Hemisphere Publishing Corporation.
- Yadigaroglu, G. (1981b). "Two-Phase Flow Instabilities and Propagation Phenomena". In *Thermohydraulics of Two-Phase Systems for Industrial Design and Nuclear Engineering*, chapter 17, pages 353–403. Hemisphere Pub. Corp.
- Yokobori, S. *et al.* (1992). "Two-Phase Flow Natural Circulation Characteristics Inside BWR Vessel". *Proc. 5th Int. Topic. Mtg. Reactor Thermal-Hydraulics*, page 21.
- Zboray, R. (2002). "*An Experimental and Modeling Study of Natural-Circulation Boiling Water Reactor Dynamics*". PhD thesis, Delft University of Technology, Delft, The Netherlands.

Summary

Currently, 434 nuclear power plants are in operation worldwide. 21 % of them are known as Boiling Water Reactors (BWRs). These BWRs have pumps that cool their reactor cores (the forced circulation BWRs). In the design of new BWRs, ways to cool the core by a natural circulation flow, without pumps, also called natural circulation BWRs, are being considered. In these new systems, a chimney is installed on top of the core to increase natural circulation flow. A possible disadvantage of natural circulation BWRs might be their susceptibility to instabilities, which could then lead to both flow and power oscillations. In the early 1990s, it became very important to assess the feasibility of large-scale natural circulation BWRs, and to guarantee stable behavior under all possible conditions. The stability features of both natural circulation and forced circulation BWRs have been investigated thoroughly, using dedicated experimental setups, analytical models and numerical codes, and will be discussed in this thesis. We distinguish between pure thermal-hydraulic stability – where the fission power is assumed to be constant – and coupled thermalhydraulic-neutronic stability – where the two-phase mixture in the core influences the fission chain reaction.

To counteract the lack of experimental investigations and analytical models with respect to the stability of the boiling two-phase flow (channel stability) in natural circulation BWRs, the SIRIUS-N facility, a version of the General Electric Company's ESBWR reactor, was built. In a BWR, the amount of vapor bubbles, the void, generated in the core affects the neutron generation rate, namely the void-reactivity feedback phenomenon. In general, the boiling two-phase flow becomes less stable with the void-reactivity feedback. The SIRIUS-N facility was equipped with an artificial void-reactivity feedback system to simulate the interference between thermal-hydraulics and neutronics. Furthermore, the void-reactivity feedback system could also be used for studying the stability of forced circulation BWRs such as the SIRIUS-F facility, a version of the ABWR. There are two oscillation modes in BWRs: (1) regional oscillations that are induced by out-of-phase oscillations in neutron flux; and (2) channel inlet flows between regions of the core that are symmetric around the diagonal of the core. In turn, core-wide oscillations are induced by in-phase oscillations among all the regions of the core.

Thermal-hydraulic stability of a natural circulation BWR

The thermal-hydraulic stability of a prototypical natural circulation BWR, as in the ESBWR, has been investigated with the SIRIUS-N facility, which behaves, due to proper scaling, similarly to the ESBWR in its thermal-hydraulics. Stability maps were obtained for the system pressures ranging from 0.1 to 7.2 MPa. It is found that the flow becomes stable below a certain heat flux regardless of the inlet subcooling of the core and the system pressure. Above that heat flux, instability was observed within a certain range of the inlet subcooling. It was also found that the unstable region shrinks in response to an increase in the system pressure. Therefore, stability can be enhanced in a cold startup process of a reactor by pressurizing the reactor sufficiently before withdrawing the control rods. This is an event equivalent to heating the reactor

core. The stability maps obtained at all system pressures demonstrate that the ESBWR has a significant stability margin.

Low pressure thermal-hydraulic stability

Two distinct responses are found in the relation of the oscillation period to the time that liquid passes in the chimney, indicating that the driving mechanisms of the instabilities are different for low and high pressures. The transition region lies between 0.5 MPa and 1.0 MPa. At low pressures (0.1 - 0.5 MPa), the observed instability was shown to be caused by flashing induced density wave oscillations. Here, flashing suddenly occurs in the chimney section, on top of the core, which then increases the natural circulation flow. At the same time, cold water flows into the chimney, since the residence time in the core is shorter due to a high flow rate. After the cold water flushes out the bubbles generated by the flashing, the flow then becomes stagnant. Consequently, the residence time in the core becomes longer, resulting in hot water rising in the chimney and causing the flashing to reoccur. In this cyclic process, the time period of the stagnant flow process was found to be the longest when compared against the other processes. Therefore, experiments have shown that the oscillation period correlates well with the passing time in the chimney for liquid single-phase flow in the chimney, regardless of the heat flux, system pressure, and inlet subcooling factors. It has also been found that flashing induces density wave oscillations above approximately 1.1 % of the quality at the chimney exit only.

High pressure thermal-hydraulic stability

At high pressures (1.0 - 7.2 MPa), the observed instability was shown to be caused by density waves known as Type-I oscillations, since the void fractions in the chimney inlet and exit are out of phase, and the instability occurs at low quality. These facts clearly indicate the characteristics of density wave oscillations. In other words, the instability is caused by the time lag between the moment that steam is generated in the core and the moment that the steam moves to the chimney section where it induces natural circulation flow. Therefore, the oscillation period correlates well with the time required for the bubbles to pass through the chimney, regardless of the heat flux, system pressure, and inlet subcooling factors.

Stability enhancement

A method to stabilize the thermal-hydraulic instability in a natural circulation BWR has been investigated both experimentally and analytically. Inlet throttling is a well established method for stabilizing the density wave oscillations in a forced circulation system. In a natural circulation system, however, increasing the inlet throttling reduces the natural circulation flow rate, shifting the unstable region to higher inlet subcoolings. The experimental results have shown that the void fraction in the chimney on the stability boundary remains approximately constant, regardless of the inlet throttling. Using the homogeneous equilibrium mixture model, together with the void fraction at the stability boundary, the stability map can therefore be predicted for a range of inlet restrictions.

Stability boundary prediction with linear stability analysis

A linear stability analysis code, based on the homogeneous equilibrium mixture model, was used to predict the stability boundaries for the lower subcooling of the natural circulation BWR. The analytical stability boundary correlates well with the experimentally-obtained stability boundary. Moreover, the linear stability analysis predicts the experimentally-obtained oscillation period as a function of the time that liquid passing in the chimney. By comparing it with linear stability analysis, we verified that the experimentally-observed instability at high pressure falls in the category of density wave oscillations known as Type-I.

Coupled thermalhydraulic - neutronic stability (natural circulation)

In order to simulate core-wide and regional modes, an artificial void-reactivity feedback system has been implemented in the SIRIUS-N facility. Void fractions were calculated in each section using the measured differential pressure, inlet velocity, and inlet temperature. The void fraction is estimated from the momentum balance, by assuming the drift flux model. By using the estimated void fractions in reactor core sections of the thermal-hydraulic loop, the void-reactivity feedback can be calculated real-time, based on the modal point kinetics of reactor neutronics. Solid-state, series-regulated power supplies that act as simulation outputs have been designed to obtain a fast response without any loss of accuracy (with a time constant of 0.3 ms based on a step response test; accuracy of 99.9 % in power amplitude and less than one degree of phase lag based on a noise response test within a target frequency range of 0.3 to 0.5 Hz). In order to obtain the decay ratio, noise analysis on the basis of an auto-regressive method has been applied to time series data for the core inlet flow rate.

The dominating instability mode turned out to be the regional mode. The decay ratio at rated operating conditions was found to be 0.54, indicating a sufficient margin to instability. These experiments were extended to evaluate the stability sensitivities of the design parameters, such as the power profile, void reactivity coefficients, core inlet subcooling, and thermal conductance of the fuel rod. The decay ratio reaches a local maximum when the fuel rod time constant is approximately 6.7 s. Therefore, the system approached its least stable condition when the oscillation period of the thermal-hydraulic instability correlated with the phase lag of the void-reactivity feedback system.

In order to identify instability phenomena, the experiments were further extended to include a hypothetical parameter range (using a double-void reactivity coefficient with inlet core subcooling increased by a factor of 3.6). The regional instability was clearly demonstrated by the SIRIUS-N facility, where the fuel rod time constant matched the oscillation period of the density wave oscillations.

Thermal-hydraulic and coupled thermalhydraulic-neutronic stability (forced circulation)

The method to implement artificial neutronic feedback has also been applied to the SIRIUS-F facility, the full-height test facility of the ABWR (itself a forced circulation BWR). Channel and regional stability experiments were conducted for a wide range of operating conditions, including the minimum pump speed and natural circulation lines of the ABWR. A distinct peak of the cross-correlation function with a negative value was found at $\tau = 0$ for all experimental parameters in this study, indicating an out-of-phase interaction mode between the two core halves (regional stability mode). Therefore, the ABWR is more susceptible to regional instability. The decay ratios and the resonance frequencies obtained from the SIRIUS-F facility are in solid agreement with those from the design analysis code, ODYSY, although some discrepancies were found in the regional stability resonance frequency on the natural circulation (reactor operating) line only. The code was validated with the SIRIUS-F facility. It can be concluded from these stability experiments that the ABWR will not encounter core-wide or regional instability at the maximum power on the minimum pump speed and natural circulation lines, even with any malfunctioning of the safety features i.e., SCRR: the Selected Control Rods Run In.

Influence of liquid density

The influence of liquid density on the stability of natural circulation flows was also investigated. A natural circulation flow is driven by density differences in both the single-phase region and the boiling two-phase region in the core and chimney. The single-phase natural circulation is induced by the difference between the liquid density in the downcomer and the liquid density in the chimney (and the core), since the water in the downcomer is subcooled. In order to in-

investigate the effect of liquid density differences on the thermal-hydraulic stability, the analysis code in use (based on the homogeneous equilibrium model) was modified to include the dependence of liquid density on temperature. Analytical results show that neglecting temperature dependence of the density yields a conservative estimate of the margin to instability at high operating power. In contrast, at low operating power results give a non-conservative estimate of the stability margin, since operating conditions shift toward or even enter into the stable region. Therefore, it is highly recommended that the dependence of liquid density on the temperature in a stability analysis, if a boiling natural circulation loop with an adiabatic chimney encounters low flow quality conditions, be included.

In conclusion, the dynamics and stability of the boiling two-phase flow have been investigated, both in the natural circulation flow with a chimney and in the forced circulation flow without a chimney. In addition to the thermal-hydraulic stability, coupled thermal-hydraulic-neutronic stability (both core-wide and regional stability) was studied experimentally and analytically for both natural circulation and forced circulation BWRs.

Samenvatting

Op dit moment zijn, wereldwijd, 434 kerncentrales operationeel. Van deze kernreactoren bestaat 21 % uit zogenaamde kokend water reactoren (KWR's). In deze KWR's wordt water, dat als koelmiddel van de reactorkern fungeert, door middel van pompen rondgepompt (dit wordt ook wel 'gedwongen stroming' in een KWR genoemd). Momenteel worden KWR's ontwikkeld waarin het water niet door pompen, maar door middel van natuurlijke circulatie rondstroomt. Om deze natuurlijke circulatie te bevorderen wordt bovenop de kern een schoorsteen (Eng: 'chimney') geïnstalleerd. Omdat de stroming in dit geval echter volledig bepaald wordt door de fysica van het systeem zelf, kan dit instabiel gedrag bevorderen. In het begin van de jaren negentig bleek het van belang om te onderzoeken of een dergelijk systeem op grote schaal haalbaar en veilig zou zijn. In dit proefschrift worden daarom de stabiliteit van zowel gedwongen stroming KWR's als die van natuurlijke circulatie KWR's onderzocht. Daarbij werd gebruik gemaakt van verschillende experimentele opstellingen, analytische modellen en numerieke codes. Tijdens dit onderzoek werd een duidelijk onderscheid gemaakt tussen thermo-hydraulische instabiliteit en gekoppelde thermo-hydraulische-neutronica stabiliteit. In het laatste geval wordt ook de interactie tussen de twee-fasenstroming in de kern en het transport van neutronen meegenomen.

Nogmaals samenvattend: In dit proefschrift zijn de dynamica en de stabiliteit van een kokend twee-fasen systeem onderzocht. Hierbij kan onderscheid gemaakt worden tussen een systeem met natuurlijke circulatie (hiervoor wordt een schoorsteen bovenop de kern geplaatst) en een systeem met geforceerde stroming (door middel van een pomp). Er is zowel gekeken naar de thermo-hydraulische stabiliteit als de globale/lokale stabiliteit ten aanzien van gekoppelde neutronica-thermo-hydraulica in de kern. Voor dit onderzoek zijn analytische modellen, numerieke methoden en experimentele opstellingen gebruikt. Omdat er relatief weinig experimentele data en analytische modellen beschikbaar zijn op het gebied van de stabiliteit van een kokend twee-fasensysteem (kanaalstabiliteit) in natuurlijke circulatie KWR's, werd de SIRIUS-N opstelling gebouwd (deze opstelling is een model voor de ESBWR van General Electric Company).

In een KWR is de productie van warmte door middel van kernsplijting afhankelijk van de hoeveelheid damp in de kern. Dit verschijnsel wordt 'void-reactivity feedback' genoemd. In het algemeen wordt een kokend twee-fasensysteem minder stabiel als er sprake is van void-reactivity feedback. De SIRIUS-N opstelling werd daarom voorzien van een regelsysteem dat de void-reactivity feedback in een natuurlijke circulatie KWR kan nabootsen. Daarnaast was het mogelijk om dit systeem te gebruiken in de SIRIUS-F opstelling, welke een KWR met geforceerde stroming moet nabootsen.

Er zijn twee oscillatie-modes in een KWR: regionale oscillaties die ontstaan door een wisselwerking tussen uit-fase oscillaties in de neutron-flux en lokale stromingsverschijnselen in de kern, en globale oscillaties die de gehele kern omvatten.

Thermo-hydraulische stabiliteit van een natuurlijk circulatie KWR

De thermo-hydraulische stabiliteit van een natuurlijke circulatie KWR (de ESBWR) is onderzocht met behulp van de SIRIUS-N opstelling. Deze opstelling gedraagt zich, door het toepassen van de juiste schaling, thermo-hydraulisch gezien hetzelfde als de ESBWR. Met deze opstelling werden stabiliteitsgrafieken gemeten, waarbij de systeemdruk werd gevarieerd tussen 0,1 tot 7,2 MPa. Uit deze metingen bleek dat de stroming stabiel is voor alle ingangstemperaturen en drukken als de warmteflux zich beneden een bepaalde waarde bevindt. Voor hogere waarden wordt instabiel gedrag gevonden voor een bepaald interval van ingangstemperaturen. Tevens werd gevonden dat de grootte van het instabiele gebied in de stabiliteitsgrafiek kleiner wordt naarmate de systeemdruk hoger wordt. We kunnen hieruit concluderen dat de stabiliteit tijdens het opstarten van de natuurlijke circulatie KWR verbeterd kan worden door het systeem eerst op een hogere systeemdruk te brengen, voordat de regelstaven worden opgetrokken (oftewel het opwekken van warmte in de kern). De stabiliteitsgrafieken die verkregen werden tijdens de experimenten laten zien dat de ESBWR een grote marge tot instabiliteit heeft.

Thermo-hydraulische stabiliteit bij lage druk

Als we kijken naar de relatie tussen de oscillatie-periode en de tijd die het water er over doet om door de schoorsteen te stromen, dan worden twee verschillende ‘takken’ in de grafiek gevonden. Deze takken geven aan dat het drijvende mechanisme dat instabiliteit kan veroorzaken verschillend is bij hoge en lage drukken. De transitiezone ligt tussen de 0,5 MPa en de 1,0 MPa. Bij lage drukken (0,1-0,5 MPa) wordt instabiel gedrag gevonden dat veroorzaakt wordt door flashing. Flashing is een zeer snel proces dat plaatsvindt in de schoorsteen en de natuurlijke circulatie bevordert. Op het moment dat flashing plaatsvindt stroomt relatief koud water de schoorsteen in doordat de verblijftijd van het water sterk afneemt door de toegenomen stroming. Nadat dit koude water de bellen, ontstaan door flashing, uit de schoorsteen heeft verdreven, staat de stroming hierdoor vrijwel volledig stil. Hierdoor wordt de verblijftijd van het water in de kern weer groter, wat resulteert in relatief heet water dat de schoorsteen binnenstroomt en flashing kan veroorzaken. Tijdens dit cyclische proces is de periode waarin de stroming stilstaat relatief lang ten opzichte van de periode die gevonden wordt voor andere soorten instabiliteiten. In de experimenten werd aangetoond dat de oscillatieperiode zeer sterk correleert met de tijd die water (vloeibaar) er over doet om door de schoorsteen te stromen, ongeacht de warmteflux, de druk en de ingangstemperatuur. Er werd ook gevonden dat flashing zogenaamde ‘density wave oscillations’ bij de uitgang van de schoorsteen veroorzaakt als de kwaliteit boven de 1.1 % ligt.

Hoge druk thermo-hydraulische stabiliteit

Bij hoge drukken (1,0 - 7,2 MPa) en een lage kwaliteit van de twee-fasenstroming kunnen zogenaamde Type-I instabiliteiten plaatsvinden, omdat de dampfractief fluctuaties bij de ingang en uitgang van de schoorsteen uit-fase zijn. Deze instabiliteit wordt veroorzaakt door het tijdsverschil tussen het moment dat stoom gegenereerd wordt in de kern en het moment dat de stoom zich in de schoorsteen bevindt (waarmee het natuurlijke circulatie veroorzaakt). De oscillatieperiode correleert daarom sterk met de tijd die bellen nodig hebben om te stromen door de schoorsteen, ongeacht de warmteflux, de druk en ingangstemperatuur.

Bevorderen van de stabiliteit

Door middel van experimenten en analytische modellen is een methode onderzocht om de thermo-hydraulische stabiliteit van een natuurlijke circulatie KWR te bevorderen. Voor geforceerde stroming KWR's kan de stabiliteit worden verbeterd door de inlaatfrictie te verhogen. Voor natuurlijke circulatie KWR's wordt door een verhoogde frictie de stroming verlaagd, waardoor het instabiele gebied in de stabiliteitsgrafiek verschuift naar lagere ingangstemperaturen (dus hogere subcooling-getallen). Er werd een vrijwel constante dampfractie in de schoorsteen op

de stabiliteitsgrens gevonden die onafhankelijk is van de ingangsfictie. We kunnen dus de stabiliteitsgrafiek voor een reeks van ingangsficties voorspellen door gebruik te maken van het 'Homogeneous Equilibrium Model' (HEM) en de dampfractie op de stabiliteitsgrens.

Voorspelling van de stabiliteitsgrens met behulp van lineaire stabiliteitsanalyse

De stabiliteitsgrens voor lage subcooling getallen in natuurlijke circulatie KWR's werd voorspeld door middel van een lineaire stabiliteitsanalyse code, welke gebaseerd is op HEM. De analytisch gevonden stabiliteitsgrenzen komen goed overeen met de experimenten. Bovendien kon de code de oscillatieperiode, als functie van de tijd die het water er over doet om door de schoorsteen te stromen, goed voorspellen. Door het vergelijken van de berekeningen en experimenten werd gevonden dat de instabiliteiten die gevonden worden bij hoge drukken van het Type-I zijn.

Gekoppelde thermohydraulische - neutronica stabiliteit (natuurlijke circulatie KWR's)

Om de globale en lokale modes te simuleren werd een void-reactivity systeem ontwikkeld en in de SIRIUS-N opstelling gebouwd. De dampfracties in elk deel van de kern werd gemeten aan de hand van het drukverschil over de kern, de stroming bij de ingang van de kern en de ingangstemperatuur. De dampfractie werd berekend door middel van de impulsbalans, waarbij het drift-flux model werd toegepast. Door het bepalen van de dampfracties in de kern kon zo de void-reactivity feedback worden toegepast, waarbij voor de neutronica in de reactor het puntkinetisch model werd gehanteerd. Hierbij werden voedingen met een zeer korte responstijd gebruikt (0,3 ms; nauwkeurigheid 99,9 % in de amplitude van het vermogen en minder dan één graad faseverschuiving, gebaseerd op een test waarbij een frequentiebereik tussen de 0,3 en 0,5 Hz werd toegepast). De decay-ratio (*DR*) werd bepaald door middel van het toepassen van een ruisanalyse methode (gebaseerd op een autoregressieve methode) op het tijdsignaal van de inlaatstroming.

De dominerende instabiliteit bleek de regionale mode te zijn. Een decay-ratio voor nominale condities van 0,54 werd gevonden, wat aangeeft dat er genoeg marge is tot instabiel gedrag. De experimenten werden uitgebreid om de gevoeligheid van de stabiliteit met betrekking tot het vermogensprofiel, de void-reactivity coëfficiënten, ingangstemperatuur en warmtegeleidingscoëfficiënt te bestuderen. De decay-ratio bereikt een lokaal maximum wanneer de tijdsconstante van de staven ongeveer 6,7 s bedraagt. Het systeem is dus het minst stabiel als de oscillatieperiode van de thermohydraulische instabiliteit overeenkomt met de faseverschuiving in het void-reactivity feedback systeem.

Om de instabiliteiten nog verder te kunnen onderzoeken zijn tijdens de experimenten extreme condities toegepast (een tweemaal zo hoge void-reactivity coëfficiënt en een 3,6 maal zo groot subcooling-getal). Er werd een regionale instabiliteit gevonden met behulp van de SIRIUS-N opstelling wanneer de tijdsconstante van de staven overeenkwam met de periode van de density wave oscillatie.

Thermohydraulische en gekoppelde thermohydraulische - neutronica stabiliteit (geforceerde stroming)

Het void-reactivity systeem werd ook in de SIRIUS-F opstelling toegepast. De stabiliteit (zowel globaal als regionaal) werd onderzocht voor uiteenlopende waarden van operationele parameters, zoals de minimum pompsnelheid en natuurlijke circulatielijnen van de ABWR. In de kruiscorrelatiefunctie van alle experimentele parameters werd een duidelijke piek gevonden bij $\tau = 0$, welke aangeeft dat de fysische grootheden in de twee helften van de kern uit-fase fluctueren (regionale instabiliteit). We kunnen daarom concluderen dat de ABWR gevoeliger is voor regionale instabiliteit. De decay-ratios en resonantiefrequenties komen goed overeen

met de waarden die gevonden werden met behulp van de ODYSY code. Daarbij moet worden opgemerkt dat er verschillen gevonden werden in de resonantiefrequentie van de regionale instabiliteit op de natuurlijke circulatielijn van de reactor in de vermogen-stroming grafiek. De code is gevalideerd met behulp van de SIRIUS-F opstelling. Uit de bevindingen kan geconcludeerd worden dat de ABWR geen globale en regionale instabiliteit vertoont bij maximaal vermogen op de minimum-pomp-snelheidslijn en natuurlijke circulatielijn, zelfs niet als één van de veiligheidsvoorzieningen (de SCRRI: Selected Control Rods Run In) het zou begeven.

Invloed van de dichtheid van het vloeibare water

De invloed van de dichtheid van het water op de stabiliteit in natuurlijke circulatie reactoren is ook onderzocht. Een stroming veroorzaakt door natuurlijke circulatie wordt zowel op aangedreven door dichtheidsverschillen in het één-fase deel van de stroming (het vloeibare water in de kern en de downcomer) als het kokende gedeelte in de kern. De invloed van het dichtheidsverschil in het één-fase deel van de stroming op de thermohydraulische stabiliteit werd bestudeerd met behulp van een code (gebaseerd op HEM). Deze code werd daarvoor aangepast zodat de dichtheid van het vloeibare water afhankelijk werd van de lokale temperatuur. De berekeningen tonen aan dat het verwaarlozen van de invloed van de temperatuur op de dichtheid een conservatieve schatting geeft op de marge tot instabiliteit voor hoge vermogens. Voor lage vermogens resulteert een dergelijke verwaarlozing in een niet-conservatieve schatting van de marge tot instabiliteit, doordat de operationele condities naar (of zelfs in) het stabiele gebied verschuiven. Het wordt daarom aangeraden om de invloed van de temperatuur op de dichtheid van water mee te nemen in de stabiliteitsanalyse, indien er sprake is van lage kwaliteiten in een natuurlijke circulatie loop.

Nogmaals samenvattend: In dit proefschrift zijn de dynamica en de stabiliteit van een kokend twee-fasen systeem onderzocht. Hierbij kan onderscheid gemaakt worden tussen een systeem met natuurlijke circulatie (hiervoor wordt een schoorsteen bovenop de kern geplaatst) en een systeem met geforceerde stroming (door middel van een pomp). Er is zowel gekeken naar de thermo-hydraulische stabiliteit als de globale/lokale stabiliteit ten aanzien van gekoppelde neutronica-thermo-hydraulica in de kern. Voor dit onderzoek zijn analytische modellen, numerieke methoden en experimentele opstellingen gebruikt.

内容梗概

世界では現在、434基の原子炉が稼働中である。そのうち21%は沸騰水型原子炉(BWR)である。稼働中のBWRは炉心を冷却するためにポンプを有している(強制循環BWR)。BWRの新たな設計として、ポンプが無く自然循環により炉心を冷却する方式が検討されている(自然循環BWR)。この自然循環BWRでは、自然循環力を増大させるために炉心上部に断熱円筒(チムニ)が設置されている。自然循環BWRは流量と出力が変動する不安定現象が生じやすいという課題を克服する必要がある。1990年代初頭、大型自然循環BWRの実現性を評価すること、および全ての運転状態が安定であることを確認することが重要となった。本論文では、忠実な実験設備と解析モデル、並びに数値解析を用いて、自然循環BWRおよび強制循環BWRの安定性を把握する。ここでは、純粋な熱水力安定性(核分裂反応量が一定の場合)と、核熱結合安定性(炉心内二相流が核分裂連鎖反応量を変化させる場合)を区別する。

自然循環BWRの沸騰二相流安定性(チャンネル安定性)を対象とした実験および解析モデルに基づく知見の欠如を克服するため、GE社のESBWR炉を模擬したSIRIUS-N設備を設計・建設した。BWRでは、炉心で発生する気泡量により中性子生成率が変化するボイド反応度フィードバック現象が存在する。一般的に、沸騰二相流にボイド反応度フィードバックが重畳することで安定度は低下する。SIRIUS-N設備は、ボイド反応度フィードバックを模擬する装置を導入し、熱水力と核反応との相互作用が模擬できる設備である。さらに、このボイド反応度フィードバック模擬装置は、強制循環BWRであるABWRを対象とするSIRIUS-F設備にも導入し、安定性を把握した。BWRでは領域不安定と炉心(一体型)不安定の二種類の不安定モードがある。領域不安定は炉心の対角線を境として、対称な二領域間でチャンネル入口流量や中性子束が逆位相で変動する現象である。一方、炉心不安定では、炉心のあらゆる場所で同じ位相で変動する現象である。

自然循環BWRの熱水力安定性

相似則に基づきESBWRと同じ熱水力挙動を示すSIRIUS-N設備を用いて、典型的な自然循環BWR(ESBWR)の熱水力安定性を解明した。系圧力0.1～7.2 MPaの範囲で安定性線図を得た。炉心入口サブクール度および系圧力によらず、熱流束がある値より小さい場合には流動は安定であることが判明した。熱流束がその値を超えると、入口サブクール度がある範囲で不安定現象が発生する。系圧力の増加に伴い、この不安定領域は減少する。よって、冷態起動過程では制御棒引抜(炉心加熱)前に炉心を十分加圧することで、安定度を増大させることができる。得られた安定線図から、全ての系圧力においてESBWRは十分な安定度を有していることが判明した。

低圧の熱水力安定性

振動周期とチムニ内液単相通過時間との関係線図において、高圧と低圧とで二つの明確な分岐が見られた。これは高圧と低圧では異なる不安定現象の駆動機構に支配されることを示唆している。二つの分岐の遷移は0.5 MPa～1.0 MPaである。低圧(0.1 - 0.5 MPa)で観測される不安定現象は、フラッシング誘起密度波振動である。ここで、フラッシングは炉心上部のチムニ内で急速に発生し、自然循環力を増大させる。同時に、流速が速く炉

心滞在時間が短いため、低温の水がチムニ内に流入する。低温の水がフラッシング気泡を押し流した後は、流れは淀む。その結果、炉心滞在時間が長くなり、高温の水がチムニ内に流入し、再びフラッシングが発生する。この一連の過程において、淀み流れ過程の時定数が他の過程と比較して最も長くなる。それ故、熱流束や系圧力、入口サブクール度によらず、振動周期は液单相流がチムニ内を通過する時間と良い相関があることが実験により示された。また、フラッシングが密度波振動を誘起するのは、チムニ出口クオリティが約 1.1 % を超える必要があることが判明した。

高圧の熱水力安定性

高圧 (1.0 - 7.2 MPa) では、ボイド率がチムニ入口とチムニ出口とで逆位相であり、低クオリティでのみ不安定現象が発生することから、観測された不安定現象は、いわゆる Type-I 密度波振動である。これらの試験結果は密度波振動の特長を明確に示している。換言すれば、不安定現象は炉心で発生した蒸気が、チムニに移動して自然循環駆動力となるまでの時間遅れに起因する。よって、熱流束や系圧力、入口サブクール度によらず、振動周期は気泡がチムニを通過する時間と良い相関があることが示された。

安定度の増大

自然循環 BWR の熱水力安定度を増大させる方法について実験および解析により検討した。入口を絞る手法は強制循環ループの密度波振動抑制策として確立した手法である。しかしながら自然循環ループでは、入口を絞ることにより自然循環流量が減少し、不安定領域を高サブクール度側に移行させる。実験の結果、安定境界上ではチムニ内のボイド率が入口絞りによらず一定であることが判明した。この安定境界上のボイド率を用いて、均質流モデルに基づき解析を行い、安定線図を入口絞りの関数として予測した。

線形安定性解析による安定境界の予測

均質流モデルに基づく線形安定性解析を行い、自然循環 BWR における低サブクール度側の安定境界を予測した。解析で得られた安定境界は実験と良く一致した。さらに、実験で得られた振動周期と液单相チムニ通過時間との関係を解析で予測することができた。これらの比較結果により、実験で観測された高圧の不安定現象は、いわゆる Type-I 密度波振動であることが検証された。

核熱結合安定性 (自然循環)

炉心一体型モードと領域モードを模擬するために、仮想的ボイド反応度フィードバック機構を SIRIUS-N 設備に導入した。各領域のボイド率の算定には、差圧、入口流量および温度の計測値を使用した。ボイド率はドリフトフラックスモデルに基づく運動方程式から計算した。熱水ループの炉心相当部ボイド率を用いて、高次モード固有値間隔を考慮した炉物理方程式に基づき、ボイド反応度フィードバックを実時間解析する。実時間解析の出力は電源である。設計した電源 (直列調整トランジスタ回路) は高速かつ高精度である。ステップ応答試験の結果は時定数 0.3 ms、ノイズ応答試験の結果は対象とする周波数帯域 (0.3 ~ 0.5 Hz) での出力振幅精度は 99.9 %、位相遅れは 1 度以下であった。減幅比を得るために、自己回帰 (AR) 法に基づくノイズ解析法を炉心入口流量の時系列データに適用した。

不安定現象の支配モードは領域モードであることが判明した。定格運転条件における減幅比は0.54であり、安定性上の余裕が十分であることを示している。更に試験を実施し、出力分布、ボイド反応度係数、炉心入口サブクール度、および燃料棒熱伝導時定数などの設計パラメータの安定性に対する感度を評価した。燃料棒時定数が6.7sになるときに、減幅比は極大になる。すなわち、熱流動不安定現象の周期がボイド反応度フィードバック系の位相遅れに等しくなるときに、系は最も安定度が低下する。不安定現象を同定するために、仮想的な条件(ボイド反応度係数を二倍および炉心入口サブクール度を3.6倍)に対して実験を行った。その結果、燃料棒時定数が密度波振動の振動周期に等しい場合に、SIRIUS-N設備で領域不安定現象が明確に再現された。

核熱結合安定性 (強制循環)

開発した核反応模擬手法を、SIRIUS-F 設備にも適用した。SIRIUS-F 設備は、強制循環 BWR である ABWR と同じ高さを有する設備である。チャンネル安定性および領域安定性試験を ABWR の最小ポンプ速度曲線および自然循環曲線を含む広い範囲で実施した。炉心入口流量の相互相関関数は $\tau = 0$ において、明瞭な負のピークを示した。これは、二つの半炉心で逆位相となる領域安定性モードに支配されていることを示している。よって ABWR では、領域安定性モードがより卓越する。SIRIUS-F 設備で得られた減幅比と共振周波数は解析コード ODYSY と良い一致を示している。但し、自然循環曲線上では、領域安定性の共振周波数が両者で多少の差異が見られた。安定性試験の結果より、ABWR は例えば選択制御棒挿入 (SCRRI) など安全系の機能喪失時においても、最低ポンプ速度曲線および自然循環曲線上では炉心不安定現象および領域不安定現象が発生することはないと結論できる。

液相密度の影響

液相密度が自然循環流の安定性に及ぼす影響について調べた。自然循環流は炉心とチムニ内の液单相領域と沸騰二相領域の密度差により駆動される。液单相の自然循環流は、ダウンカム内の過冷されている液相密度と炉心とチムニ内の液相密度の違いにより発生する。液相密度差が熱水力安定性に与える影響を調べるため、既存の均質流モデル解析コードを液相密度の温度依存性が考慮できるように修正した。解析により、液相密度の温度依存性を無視すると、出力が高い場合には安定裕度を保守側に評価することが判明した。一方、出力が低い場合には、運転条件が安定領域側もしくは安定領域内に移行するため、安定性余裕が非保守側に評価される。よって、断熱チムニを有する沸騰自然循環ループが低クオリティ状態で運転される場合には、安定性解析では液相密度の温度依存性を考慮することを強く推奨する。

総括すると、チムニを有する自然循環流およびチムニのない強制循環流について、沸騰二相流の動力学と安定性を明らかにした。自然循環 BWR と強制循環 BWR の双方を対象に、熱流動安定性のみならず、核熱結合安定性 (炉心安定性および領域安定性) を実験と解析により把握した。

Dankwoord (Acknowledgements)

It has been my privilege to complete this work under the guidance of my promoter prof.dr.ir. Tim H. J. J. van der Hagen. We first met at the NURETH-7 conference. It was also the first time for me to present my work at an international conference. Since he raised his hand after my presentation for asking me a question, we have had enthusiastic discussions and good humor ever since. I would like to express my gratitude to him. Thanks are extended to dr.ir. Martin Rohde for great refinements of my thesis. In addition, I learned from his excellent English writing skills.

I would like to express my sincere gratitude to Emeritus Prof. Akira Inoue and Prof. Masanori Aritomi of the Tokyo Institute of Technology, and to Prof. Kenji Fukuda of the Kyushu University for their continuous assistance and constructive discussions regarding this work. Most of the work has been conducted at the Central Research Institute of Electric Power Industry (CRIEPI), for more than ten years. I would like to thank Akira Yasuo and Fumio Inada of CRIEPI for giving me the opportunity to work in the research on BWR stability. Many thanks to Yoshiyuki Shiratori of Techno Service Co. and Jinya Amano of CERES, Inc. who helped me with the experiments. I am thankful to Moriyasu Tokiwai, Nobuyuki Tanaka and Eiko Hara of the Fresh Green Office members from CRIEPI for consulting and supporting customers, while I passed the hot and humid summer in Japan.

I wish to thank my room-mates at the Department of R³ in Delft, being Annalisa Manera, Christian P. Marcel, Arun K. Nayak, Róbert Zboray, and David D. B. van Bragt for their help and fruitful discussions. I owe gratitude to Ine Olsthoorn, Danny Lathouwers, August Winkelman, Willy de Kruijf and other staff members and colleagues from the Department of R³ for administrative matters. I enjoyed staying in Delft with Hirokazu Shibata, Carlos C. Ceballos and other friends. I had a good time with all of them in the Japanese and Spanish speaking societies through playing sports and having parties.

I would like to thank Takafumi Anegawa and Shinya Mizokami of TEPCO and Jun Yokoya of J-Power for providing the design parameters of the ABWR. I would like to thank Takanori Fukahori and Yoshiro Kudo of GNF-J for conducting the linear stability analysis with the ODYSY code. I am grateful for the many constructive suggestions on reactor physics modeling made by Yuichiro Kubo of NFI and on noise analysis made by Yutaka Takeuchi of Toshiba. I would like to thank Dr. Yee Kwong Cheung and Dr. H. T. Kim of General Electric Nuclear Energy for providing the design parameters of the natural circulation BWR.

Finally, thanks are extended to my family for supporting me along the whole way including my grandfather, who expected me to become a doctor.

Thanks to all of you, I look back to fourteen years of tough work, stimulating discussions, far journeys and all the rest.

Curriculum vitae

Masahiro FURUYA

Date of birth : 8th August 1968

Place of birth : Yamaguchi, Japan

1987-1991: B. Engineering at Kyushu University, majored in Applied Nuclear Engineering
Graduated March, 1991
Graduate subject: Three Dimensional Large Eddy Simulation for Turbulent
Natural Convection Flow

1991-1993: M. Science and Engineering at graduate school of Tokyo Institute of Technology,
majored in Nuclear Engineering
Graduated March, 1993
Graduate subject: Cooling Performance and Critical Heat Flux of High Heat
Flux Surface by A Two-Dimensional Impinging Liquid Jet

- Stay at Argonne National Laboratory, Illinois, USA (July - November, 1993)
Subject: Experiments Investigation and Analytical Modeling of Chemical
Ignition Type Vapor Explosion

1993-: Research Senior at Nuclear Technology Research Laboratory at Central
Research Institute of Electric Power Industry (CRIEPI), Tokyo, Japan

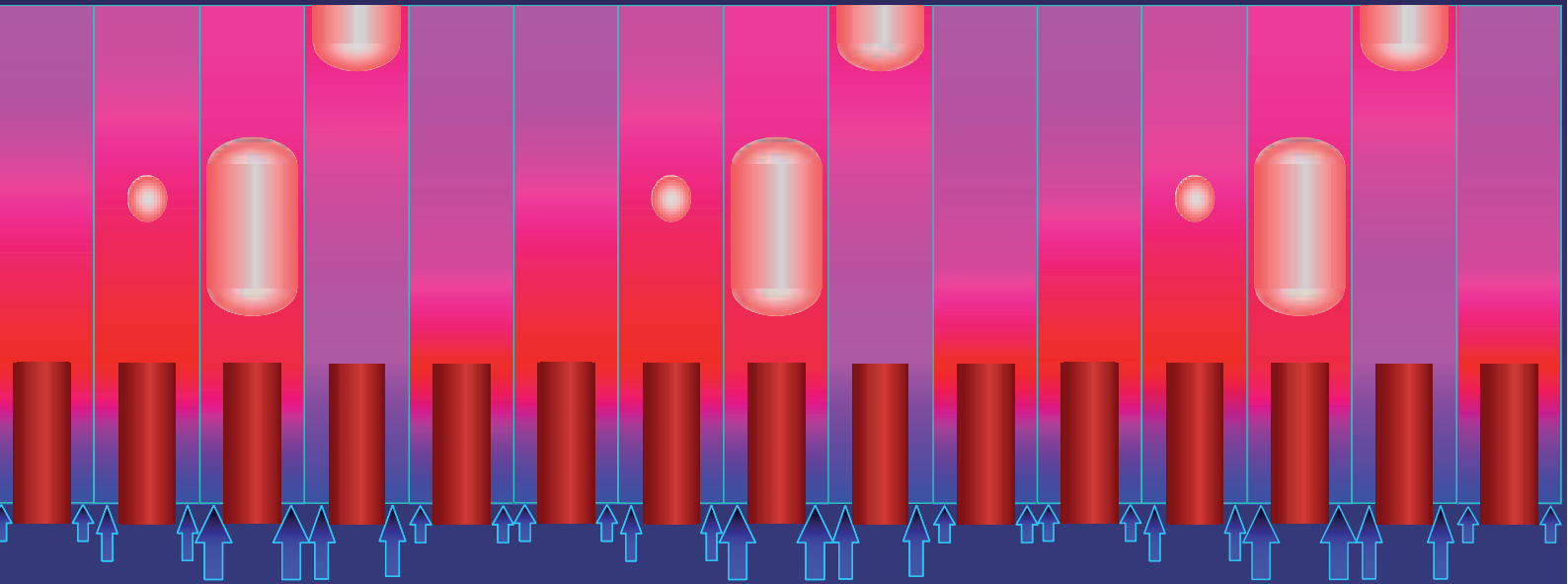
- Stay at Interfaculty Reactor Institute, Delft University of Technology, Delft,
the Netherlands (May - July, 1998, June - August, 2003 and June - August, 2004)
- Stay at the Department of Radiation, Radionuclides and Reactors (R³),
Faculty of Applied Sciences, Delft University of Technology, Delft,
the Netherlands (August 2005)
Subject: Experimental and Analytical Modeling of Natural Circulation BWRs

Publications

Journal Papers	41
Reports	59
Conference Papers	153
Patents	91

Awards

1. Technical Award, Japan Society for Multiphase Flow, "Wettability Improvement Technology on the Basis of Radiation Induced Surface Activation," July, 2004.
2. Nikkei BP Award, Nikkei Business Publication Co., "Amorphous Powder Production Utilizing Vapor Explosion Phenomena," April, 2004.
3. Best Presentation Paper, Japan Society of Mechanical Engineers, "Visualization of Liquid-Liquid Interface and Occurrence Condition of Vapor Explosions," September, 2003.
4. Original Paper Award, JSME, "Study of a Boiling Natural Circulation Loop with a Chimney - 4th Report: Analytical investigation of stability and thermal-hydraulic behavior in a chimney at high pressure," April, 2003.
5. Best Research Award, Atomic Energy Society of Japan, "Development of Core-Wide and Regional Stability Facility, SIRIUS, that Simulates Void-Reactivity Feedback, and Stability Estimation," March, 2003.
6. Best Presentation Paper, Japan Society of Mechanical Engineers, "Development of Rapid Cooling Process Utilizing Vapor Explosion and Application to Amorphization of Practical Materials," September, 2002.
7. Best Presentation Paper, Institute for Liquid Atomization and Spray Systems, "Development of Innovative Rapid Cooling and Liquid Atomization Process and Atomization of Highly Viscous Slug," December, 2001.
8. Best Technical Paper, American Society of Mechanical Engineers, "On Applicability of Direct Contact Heat Transfer Steam Generators for LMFBRs," May, 2000.
9. Best Research Award, Japan Society of Mechanical Engineers, "Mechanism of Triggering Process in Vapor Explosions," April, 2000.
10. MVP Award in Computer-Base Measurement Automation Symposium, National Instruments Co., "Development of Nuclear Reactor Simulator SIRIUS with Data Socket Technology," December 1999.
11. MVP Award in Virtual Instrumentation Symposium, National Instruments Co., "Investigation System of Vapor Explosion Mechanism with Virtual Instrumentation," December 1997.
12. TAKUMI Award, CRIEPI, "Development of Visualization System to Investigate Vapor Explosion Mechanism," September, 1997.
13. Best Research Award, CRIEPI, "Stability Evaluation of Next Generation Natural Circulation BWR during Startup Procedure," November, 1996.
14. Best Research Award, Heat Transfer Society of Japan, "Evaporation Characteristics and Thermal Interactions of A Water Droplet Impinging onto Molten Alloy Surface," May, 1996.




TU Delft

Delft University of Technology

ISBN 1-58603-605-X



9 781586 036058

ISBN 1-58603-605-X



Delft University Press is an imprint of IOS Press

IOS Press